

Reconfigurable DNA-nanochambers as dynamic compartmentalization systems

Inaugural-Dissertation

zur Erlangung des akademischen Grades eines
Doktors der Naturwissenschaften
– Dr. rer. nat. –

der Fakultät für Biologie
an der

Universität Duisburg-Essen

vorgelegt
von
Elisa-Charlott Schöneweiß (M. Sc.)

aus
Marl

Februar 2018

Die vorliegende Arbeit zugrundeliegenden Experimente wurden im Zeitraum von Oktober 2014 bis Oktober 2017 im Arbeitskreis von Dr. Barbara Saccà am Zentrum für medizinische Biotechnologie an der Universität Duisburg-Essen durchgeführt.

Tag der Disputation: 11.05.2018

1. Gutachter:	Prof. Dr. Markus Kaiser
2. Gutachter:	Prof. Dr. Elsa Sánchez-García
Vorsitzende des Prüfungsausschusses:	Prof. Dr. Michael Ehrmann

Dedicated to Mom and Dad

Table of contents

1	Introduction	1
1.1	Nanotechnology	1
1.2	DNA Nanotechnology	2
1.2.1	Design approaches	4
1.3	Functionalization/ Modification of DNA Nanostructures	9
1.3.1	Protein binding	10
1.3.2	Dynamic DNA nanotechnology	14
1.3.3	Role played by the surrounding environment	16
2	Objective of the thesis	18
3	Results and Discussion	19
3.1	Design of the programmable and modular DNA host	21
3.1.1	Topographical characterization using streptavidin as marker.....	21
3.1.2	AFM and gel electrophoresis analysis of the DNA origami constructs.....	23
3.2	The collective behavior of spring-like motifs tethered to DNA nanostructures	30
3.2.1	Design and FRET labeling of the device	30
3.2.2	Thermal stability of the devices	32
3.2.3	Considering the tethered hairpin motifs as elastic springs	42
3.2.3.1	Construct I – set of springs in parallel	42
3.2.3.2	Construct II & III – two sets of springs in parallel.....	44
3.2.4	Tethering effect according to a nearest-neighbor/WLC model	45
3.2.5	Tug-of-war between opposite forces	53
3.3	Development of a versatile DNA nanochamber for defined protein encapsulation.....	56
3.3.1	Successful G-quadruplex formation characterization for cargo loading.....	58
3.3.2	Thrombin stability	61

3.3.3	Binding affinity of a thrombin molecule embedded into DNA origami frame	61
3.3.4	Proteolytic activity of the caged thrombin protein within the DNA origami frame	69
4	Material and Methods.....	74
4.1	Material.....	74
4.2	Methods.....	74
4.2.1	Development of a versatile DNA nanochamber with modular and programmable size.....	74
4.2.1.1	Design of the DNA reconfigurable nanostructure	74
4.2.1.2	Scaffold m13mp18 preparation	81
4.2.1.3	Assembly of the DNA origami host.....	84
4.2.1.4	Purification of the assembled nanostructures	84
4.2.1.5	Determination of the concentration of the assembled DNA nanostructures using quantitative Real Time-Polymerase Chain Reaction (qRT-PCR).....	85
4.2.2	Protein processing.....	86
4.2.2.1	Expression and purification of the streptavidin protein.....	87
4.2.2.2	Characterization of correct G-quadruplex formation using fluorescence resonance energy transfer (FRET)	89
4.2.2.3	Protein labeling	90
4.2.2.4	Functionalization and loading of the DNA origami host with thrombin or other proteins	91
4.2.3	Enzyme studies.....	91
4.2.4	Characterization of the molecular forces applied by a collection of tethered hairpin motifs.....	94
4.2.4.1	Temperature-dependent FRET spectroscopy	94
4.2.4.2	Tug-of-war experiments	97
4.2.4.3	Temperature-dependent UV spectroscopy	98
4.2.5	Imaging analysis	98

4.2.5.1 Gel electrophoresis analysis	98
4.2.5.2 Atomic force microscopy (AFM) imaging and data analysis	100
4.2.6 Molecular dynamics simulations and atomistic models	100
4.2.7 Software	102
5 Conclusions and Outlook.....	104
6 Summary.....	105
7 Zusammenfassung.....	106
8 References.....	107
A List of Physical Parameter and Abbreviations	116
B List of Figures	121
C List of Tables	124
D List of Equations	126
E Supplementary Information	127
F Curriculum Vitae	158
G List of Authored and Coauthored Publications	159
H Declarations	160
I Acknowledgement	162

1 Introduction

1.1 Nanotechnology

The 21st century is a representative era for the enormous revolution of the nanotechnology research field, growing parallel to device miniaturization and the development of nanoscience. Beside advanced vaccines and medicines for striking diseases, innovative *in vivo* medical diagnostic instruments as well as progressive drug delivery systems were constructed, all relying on recently founded approaches discovered by this interdisciplinary field of science. However, beneficiary impact is not uniquely addressed to medical aspects. Nanotechnology has also positively influenced the construction of smart nanomaterials, cosmetics components and solar energy cells. Small particles (silicate, silver or zinc oxide) are incorporated into plastic packaging to block UV rays and provide anti-bacterial protection, while improving the strength and stability of plastic films and solar panels shape like multi-layer nanorod funnels in order to capture incident sunlight very efficiently. Another example of all-day-life nanomaterial is the Pilkington's self-cleaning glass. Here, a hydrophilic coating out of nanoparticles is used, responsible for breaking down organic dirt and supporting drying quickly without leaving any streaks. Nanomaterials have found application in advanced textile fabrication, resulting in hydro repellent clothing as well as in the military defense sector. Here, the nanostructural organization of the carbon coating material of military vessels results in invisibility to radar radiations by reducing the emission of reflected wavelengths. Altogether, these examples reveal that nanotechnology opens us the door to the tiny world, applicable in an enormous number of divergent fields.

The pioneer of this field was Richard Feynman, Nobel laureate in physics in 1965. On the 29th Dec. 1959 he gave a talk at the American Physical Society meeting, entitled: "There's Plenty of Room at the Bottom." That was the early beginning of the nanotechnology era. He envisaged to manipulate and control things on the nanometer scale and challenged the possibility of making big things small, i.e. writing the entire 24 volumes of the *Encyclopedia Britannica* on a head of a pin, by just reducing the size of all the writing by 25,000 times [1]. His talk encouraged a lot of scientists to overstep the minimal size of things and about 25 years later Tom Newman, a graduate student at Stanford University, succeed in writing a page of Charles Dicken's "A Tale of Two Cities" on the head of a pin with a beam of electrons at the required scale.

Today the task to generate nanosized objects can be summarized by two main approaches, *the top-down* and *the bottom-up approach*. Feynman proposed in his talk to

use light for the precise arrangement of molecules and/or single atoms on predefined surfaces, nowadays resulting in the application of the *top-down-approach*. This method covers, *inter alia*, techniques like photolithography, micropatterning techniques and inject-printing, all based on the same concept of packing a huge amount of information on a tiny small space [2-4]. Feynman's initial inspiration to his visionary ideas came from the observation of nature. In the cell, all information for the organization of a complex creature is stored in form of a long-chain DNA molecule in which approximately 50 atoms are used for one bit on information [1]. Nature therefore achieves control of matter distribution in space and time by complex molecular self-assembly processes, i.e. through a so-called *bottom-up approach*. In this way, all possible information is extracted from a single small nanoobject: i.e. cellular duplication, growth, movement and interaction are stored and coded in the nucleus of the cell in form of a densely packed DNA molecule. In this sense, DNA is itself a brilliant example of nanotechnology in nature, whose predictable self-assembling properties, discovered in 1953 by Watson and Crick, have later led – not surprisingly - to the idea to use DNA as a construction material [5;6].

1.2 DNA Nanotechnology

The fundamental work of Watson and Crick showed that the double stranded DNA molecule consists of the four bases adenosine (A), thymine (T), guanine (G) and cytosine (C), paired according to one simple “designer” rule (A with T and G with C). This specific and predictable self-assembly code thus opens the possibility to create complex nanoobjects like in a LEGO game. Beside the self-recognition properties, the overall advantages of using DNA as a building material for nanosized constructs are (i) its high physicochemical and high mechanical stability (persistence length (L_p) of dsDNA is ca. 50 nm) and (ii) its synthetic availability also in chemically modified forms (DNA, RNA, PNA & other analogues). This allows to construct DNA nanostructures in an efficient time frame at low costs with the opportunity to integrate selected groups at predefined positions for further addressability (figure 1-1).

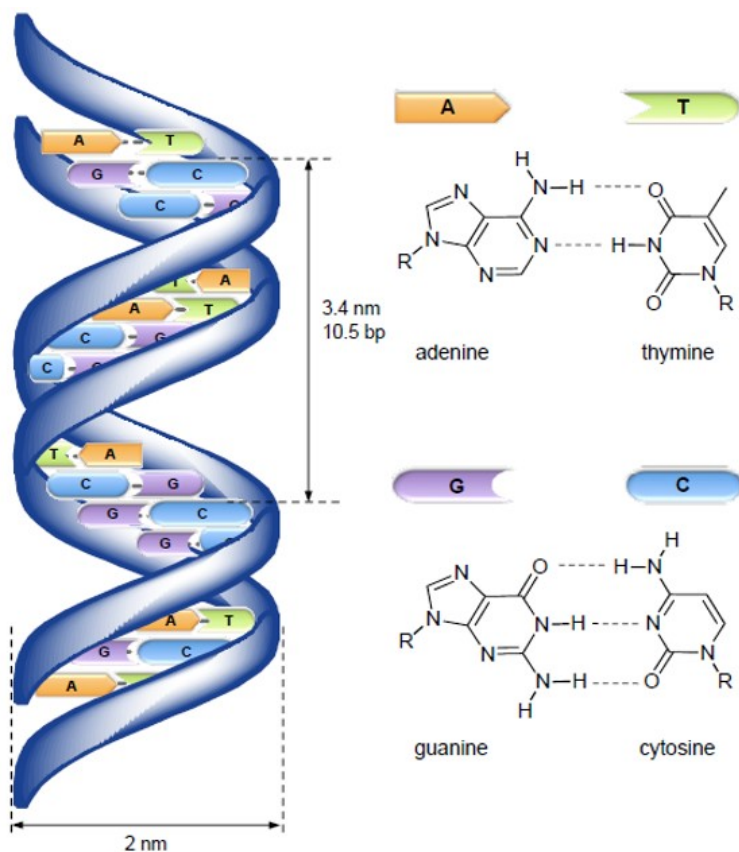


Figure 1-1: Schematic representation of the DNA double helix. The molecule is built up by four nucleobases which bind pairwise, defining complementary base-pairs, i.e. guanine (G) with cytosine (C) and thymine (T) with adenine (A). In its right-handed B form, which is the most common in nature, the helical structure is parted in a major (22 Å wide) and a minor groove (12 Å wide). The helix has a diameter of about 2 nm and each 10.5 bases the strands perform a complete turnaround the helical axis. The DNA molecule is an ideal candidate as a construction material, because (i) it is intrinsically a nanometer-sized object, (ii) it has a relatively

high physical and chemical stability, (iii) it can be nowadays easily purchased at low costs and (iv) conveniently modified with standard conjugation procedures. Images taken with kind permission from Saccà et al. [7].

Ned Seeman is mostly noted for being the founder of DNA nanotechnology. He came up with the idea in the early 80's, when he thought of using DNA for the construction and precise arrangement of nanosized objects [8]. He was inspired by a special woodcut (figure 1-2), realizing that a three-dimensional lattice could be constructed by the association of short DNA molecules linked one another into simple motifs, such as the Holliday junction motif. This idea resulted in the construction of the first artificially designed DNA tile. DNA tiles are multi-branched motifs formed by two or more intertwining DNA duplexes in (at least) one common branch point. The first immobile tile consisted of a 4-way junction formed by four defined 16 bases long single stranded DNA oligonucleotides, linked at one common point, the crossover, and arranged into four double stranded DNA segments of 8 bp each. Contrarily to its natural analog motif, the Holliday junction, found in genetic replication and recombination, the DNA tile designed by Seeman cannot undergo any topological isomerization. In this sense, the tile is immobile, that is, is designed to avoid its resolution into distinct double helical segments and therefore, lacks the capability to undergo branch migration at the crossover point.

Connecting the motif to itself along all possible directions should result in the formation of a lattice, which in principle can be used to orient target molecules in space for further crystallographic purposes. Although this concept may appear to be rather simple, the *de-novo* design of immobile DNA tiles is indeed the conclusion of several years of theoretical and experimental work, which eventually signed the beginning of the DNA nanotechnology field (figure 1-2).

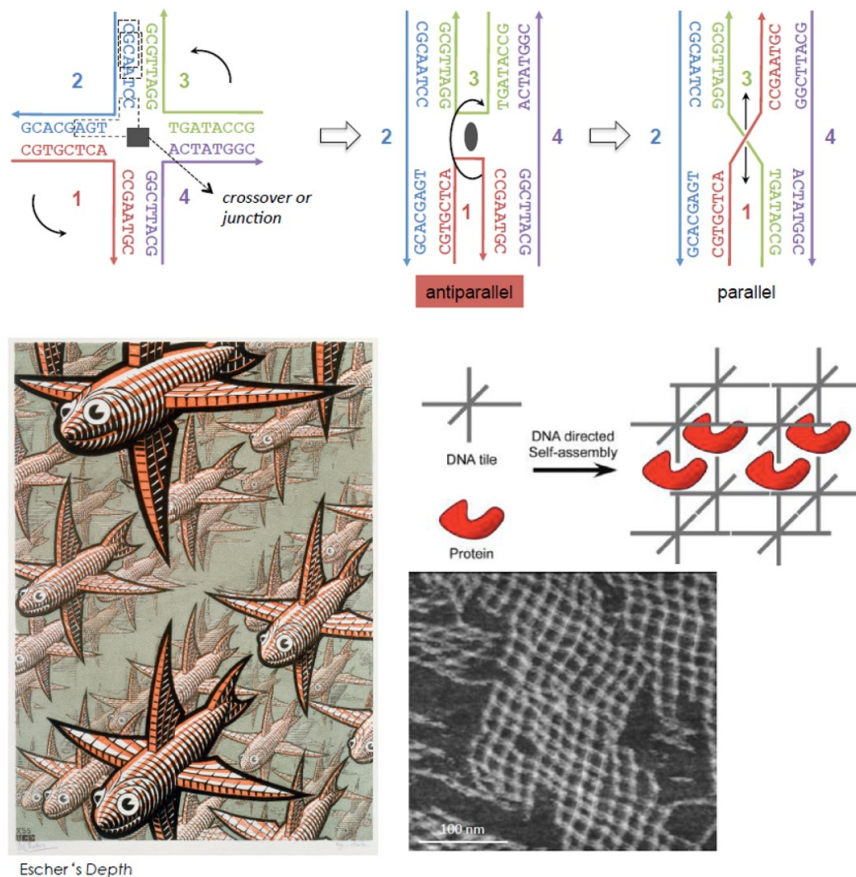


Figure 1-2: Pioneering work of Ned Seeman, representing the fundamental idea of the rapid growing DNA nanotechnology field. Images were modified from Seeman's initial work with kind permission [8].

1.2.1 Design approaches

Multi stranded approach

Seeman's 4-way junction in 1982 represents the first example of the so-called *multi-stranded approach*. This relies on the design of DNA sequences which self-assemble into branched motifs of predefined geometry [9] by means of a rather strict concept of sequence-symmetry minimization [10]. According to this principle, the sequences of the participating DNA strands are chosen to be maximally different from each other,

such that competing secondary structures can be almost excluded. Following this basic idea, multiple branched motifs were developed, featuring multiple crossovers, such as for example the so-called DX tiles [11]. These motifs can be classified into DAO or DAE tiles and are formed by two antiparallel helices whose two crossovers are spaced either by an odd ($2n+1$) or an even ($2n$) number of half helical turns ($n= 5$ bp), as schematically shown in figure 1-3. Joining four Holliday junctions one another at a common branched point led to more complex constructions as the 4x4 DNA motifs [12], consisting of nine distinct oligonucleotides intertwined into a 4-arms junction. This motif is able to form two dimensional arrays by means of sticky-ends cohesion between distinct tiles, i.e. short extended and mutually complementary single strand segments located at the 5' or 3' termini of the junction's arms. This characteristic is responsible for hybridization of the single building blocks triggering the crystallization process of the DNA network (figure 1-3).

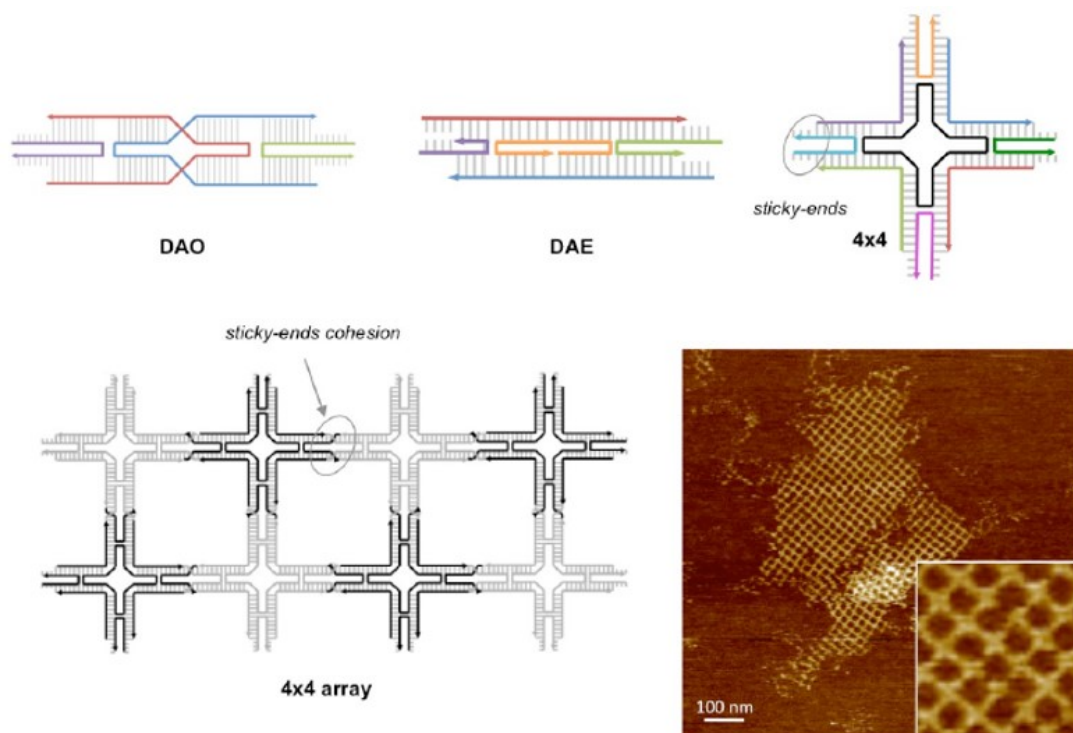


Figure 1-3: Multiple-branched antiparallel DNA motifs: the so-called DX tiles (subdivided in DAO and DAE tiles, in which the two crossovers within the tile are spaced, respectively, by an odd or an even number of half helical turns) and, the 4x4 motif. By extending the motifs's edges with sticky-ends, large lattices can be obtained, as for example 4x4 arrays. Images taken with kind permission from Saccà et al. and Yan et al. [7;12].

Important hereby is that the designed ends should ensure strong cohesion between the motifs, based on an increased CG content and/or length of the single stranded

segments and that the assembly temperature of the tile should be different from (and ideally higher than) the formation temperature of the array's formation. The connecting sticky-ends need to be three to five bases long to ensure sufficient specificity and stability of the formed double helical segments. However, particularly crucial is the overall control about the stoichiometry and purity of the constituent oligonucleotides. Unbalanced strands content and/or traces of truncated or deleted DNA sequences may increase assembly errors particularly for lengthy processes. Besides one work from the Liedl laboratory [13], the multi-stranded approach is up to now one of the most efficient ways for the construction of artificial DNA crystals [14]. After the seminal work of Ned Seeman, different laboratories worldwide were able to develop more sophisticated sequence symmetric and asymmetric 3-point, 4-point and 6-point stars, resulting in large arrays of different patterns [15-18].

Scaffolded DNA-origami approach

Almost ten years ago, Paul Rothemund came up with an innovative approach that revolutionized the way to construct DNA nanosized objects. He published the first scaffolded DNA-origami structure [19], thus signing the beginning of an extraordinary development in the field of structural DNA nanotechnology, which enormously facilitated accessibility to sophisticated nanosized objects, before only hardly imaginable [20;21]. The *scaffolded approach* is comparable to the Japanese art of paper folding, in that it uses a long circular single stranded DNA scaffold from the m13mp18 phage genome and folds it into a desired shape in combination with a few hundreds of short oligonucleotides. These are partly complementary to distinct locations of the scaffold strand and, through formation of Holliday junctions, bring discontinuous regions of the scaffold in close proximity, eventually resulting in the desired geometry of the object of interest (figure 1-4). Because of the circularity of the scaffold strand applied in most designs, it is important that the underlying folding pathway is circular as well, meaning that starting for example from the bottom of the structure, the scaffold will run back and forth along the first half of the shape till the top and then will run back down along the second half of the shape, thus returning to the initial position. The inverting points of the scaffold generate the so-called "seam" of the structure. In principle the DNA origami is a molecular platform of different crossover patterns, whose relative orientation defines the final geometry of the structure. For constructing a planar origami structure, the crossovers need to be placed at 180° one another, i.e. every 16 bp, in order to connect

neighboring helices along the same plane. Correct assembly of the structure is mainly attributed to the entropic advantage in using a single long scaffold strand for folding [22].

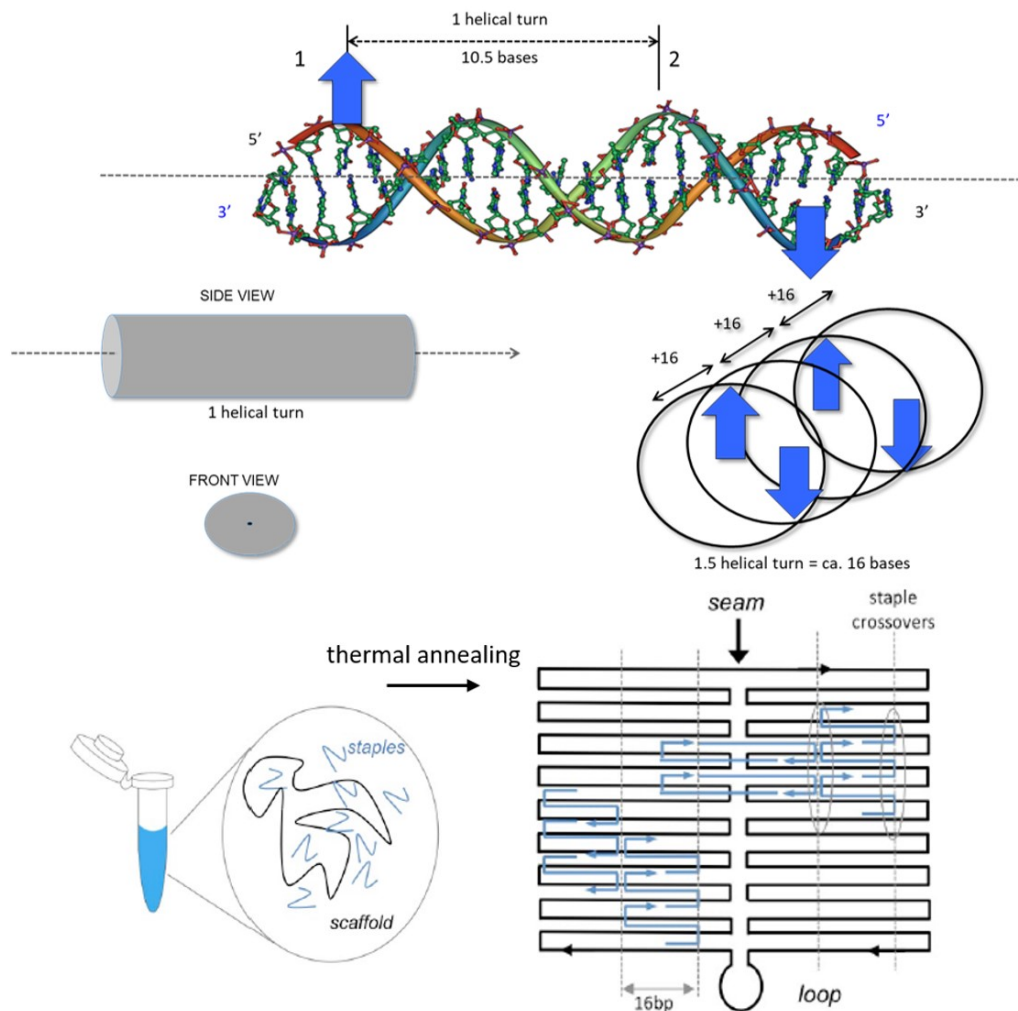


Figure 1-4: The scaffolded DNA origami approach. The predefined structure is folded during a thermal annealing step by mixing the long circular single stranded scaffold with the appropriated staples strands (blue). The staple strands connect distinct regions of the scaffold strand, bringing them in near proximity by forming Holliday junction motifs. A rule of thumb to reach a planar connection between two adjacent helices is to place the cross overs every $1 \frac{1}{2}$ helical turn (every 16 bp). By repeating this concept, one can build up a planar structure.

In comparison to the *multi-stranded approach* the designed staples of a DNA origami shape are chosen to hybridize to a common scaffold rather than with themselves, circumventing the need for precise control of their stoichiometric ratio, which is therefore no more the most crucial factor for successful realization of the structures. The initial correct arrangement of the scaffold favors the further binding of the remaining staples,

such that possibly existing wrong or truncated sequences are easily displaced by strand invasion and exchange mechanisms. Thus, experimental errors and time of synthesis are dramatically reduced.

In this way, Rothemund developed a method for the generation of complex nanoobjects of programmable dimension and molecular addressability, making the scaffolded DNA origami approach a very robust and powerful tool for construction of DNA-based architectures [23-25]. Based on the two approaches presented here, a lot of efforts have been devoted to the development of alternative design strategies [25-31], enlarging the spectrum of attainable structures and demonstrating the still bright future of DNA nanotechnology. Thanks to the constantly innovative software tools assisting the users in the engineering of DNA nanostructures, the time required for designing a single construct is drastically reduced and of course the probability of human errors in a completely manual process could be limited.

Alongside the rapid succeeding progress, based on modern design principles and user-friendly software tools, scientists were able to employ the huge amount of various DNA nanostructures to face struggling research challenges in numerous scientific fields, whereas only a few can be covered here. DNA nanotechnology offered the possibility to explore distinct protein patterning by employing DNA origami structures as addressable molecular pegboards [12]. These have been used to address signaling patterns for receptor mediated functioning [32], or to construct DNA encapsulation systems, as innovative drug delivery systems [33;34]. In a recently outstanding work presented by the Dietz group, the computer predesigned staple strands were replaced by distinct number of genetically engineered talin proteins to link different locations of the single stranded scaffold into a desired geometry. This showed that it is even possible to assemble a predefined nanostructure under physiological conditions *in vitro*, opening a prospective attempt to manipulate intracellular processes in user defined ways [35]. Moreover, the capability of precise local and temporal arrangement of molecules by means of this technology can help to elucidate the spatial orientation and number of molecules in a defined nanoenvironment by means of current single-molecule techniques [36;37]. In another work from Yin's laboratory, single building blocks made out of DNA were used to develop distinct DNA crystals of precise size, possibly serving as etching mask for fabricating diverse inorganic-materials-based devices [38]. In another work, Acuna *et al.* showed progress in constructing newly optoelectronic hybrid materials [39]. The validated high fidelity of this technology together with the development

of hierarchical self-assembly procedures enables to connect numerous DNA origami subunits by shape complementarity, base pairing interaction and blunt-end stacking, resulting in the construction of structures in the micrometer range and thus overcoming the large-scale limitation due to the scaffold size. This represents a striking step towards the development of macro materials with addressable features of nanometer size and a structural organization, comparable to their natural counterparts [40-42]. The enormous improvements of the field, the rapid advancement of technologies and design strategies enables nowadays to address the nanosized world with a high level of control.

However, for controlling the spatial arrangement of single molecules, static frameworks were mostly used. However, for constructing truly biomimetic nanocompartments, dynamical features are particularly crucial. Structural changes are constantly taking place within and between cellular compartments to allow the spatial rearrangement of internalized components, their mutual interaction, efficient transport and release to other cellular locations. Thus, accurately bio-inspired compartmentalization systems should provide not only a structurally confined space for isolation of a chemical event, but also be able to actuate dynamic operations in response to environmental changes. Therefore, DNA nanostructures need to be modified by integrated, triggerable, dynamical features to broaden the opportunity to develop DNA- nanomotors [43;44] and bioinformatic techniques for simulating complex natural systems [45]. All these applications share a common requirement, namely the proper functionalization of the origami platform in order to interact with the molecule or protein of interest to be elucidated [46]. The following chapter covers the chemical modification strategies that have been successfully applied to construct synthetic, truly bio-inspired compartmentalization systems made of DNA.

1.3 Functionalization/ Modification of DNA Nanostructures

Keeping in mind that reliable and realistic applications of DNA nanosystems are largely based on the successful and appropriate functionalization of the nanostructures, the use of the DNA molecule as a recognition motif is presented in this section and explained in detail by means of numerous examples. The possibility of functionalization can rely on the utilization of already characterized oligonucleotides, which serve as substrates for highly specific DNA-binding enzymes [47;48] or on the hybridization of specific DNA tagged molecules of interest to complementary protruding arms

extending from the origami platform at selected positions [33]. Additionally, DNA nanostructures may be designed to contain dynamical features, whose configurational state can be manipulated in a predictable manner [49].

1.3.1 Protein binding

Nature confines molecules within a defined time frame by means of so called compartmentalization systems, like mitochondria, organelles or the cell nucleus itself [50;51]. Thus, achieving control on matter distribution in space and time, the cell can stabilize reactive intermediates, perform translocation events, catalyze reactions and affect specific peptide conformations. In the effort to mimic such natural compartmentalization systems, an emerging approach uses the DNA molecule as the building block of self-assembled objects with molecular addressability and predictable shape [52], thus allowing to construct DNA origami compartments of variable size, mechanical rigidity and loading capability [49;53-56]. This, together with the development of sophisticated single-molecule technologies like atomic force microscopy (AFM), transmission electron microscopy (TEM) or total internal reflection fluorescence microscopy (TIRF), makes the DNA origami method a powerful tool for analysis of biochemical processes at the single-molecule level [57]. To address a molecule of interest specifically and efficiently, a selected DNA sequence within the nanostructure need to be modified into a defined recognition motif for sequence-specific binding of that molecule, which could be a protein or a small molecule ligand. Until now, a variety of strategies were employed to couple synthetic DNA oligonucleotides to a molecule of interest, e.g. a protein or a cargo, resulting in either covalent or non-covalent conjugation methods, described in the following sections.

Covalent protein coupling

The *covalent approach* is based on the modification of a predefined selected DNA strand with a chemical function, which is then covalently bound to the protein/molecule/particle of interest. This strand may be either an extended strand of the DNA nanostructure or a strand complementary to a protruding arm extending out of the origami surface. Thus, whereas in the former case the DNA-target conjugate will be directly bound to the nanostructure, in the latter the binding will be driven by DNA hybridization. Typically, thiol chemistry is used for the DNA-protein conjugation. The DNA strand is altered to feature a thiol group at the end of the strand, which can be

consequently coupled to genetically engineered cysteine residues of recombinant proteins, allowing to construct protein-DNA-conjugates of defined stoichiometry and regioselectivity [58]. Particularly important for this approach is the irreversible coupling of the disulfide bonds, based on the introduced cysteine residues. To bypass the cleavage of the bonds under reductive conditions a chemical crosslinker, bearing a maleimide functionality can be used. Sulfosuccinimidyl 4-(N-maleimidomethyl) cyclohexane-1-carboxylate (sulfoSMCC) is a typical example of heterobifunctional crosslinker used to link amino-reactive groups on the protein surface to thiol-modified oligonucleotides [59]. If cysteine residues are accessible on the protein surface, amino-modified oligonucleotides can be used instead [60]. Until now, the application of heterobifunctional crosslinkers is the most common approach used to link selected proteins on DNA scaffolds [33]. Despite its chemoselectivity, the presence of several lysine residues on most protein surfaces makes the method poorly regioselective. On the other hand, the lack of available single cysteine groups, accessible on the surface of the protein and not critical for its conformational stability, also severely limits the application of this method. Thus, alternative methods were developed to couple functional groups within the protein sequence in a chemo- and regio-selective manner. One of the most common strategies relies on the use of self-labeling proteins, such as “Snap-tag” and “HaloTag”. These specifically bind to a benzylguanine (BG) and chlorohexane (CH) ligands [61;62], allowing the site-selective coupling of DNA nanostructures to a protein of interest, previously fused to the corresponding protein tag [63;64]. Examples of the covalent approach are given in figure 1-5.

Unfortunately, all these methods share a number of drawbacks, namely extensive protein manipulation, as well as alteration of the protein surface and therefore of its natural properties, which may interfere with molecular recognitions events. Therefore, alternative methods were developed, inspired to natural recognition strategies and based on non-covalent coupling approaches, thus surpassing the limitations of current synthetic methods.

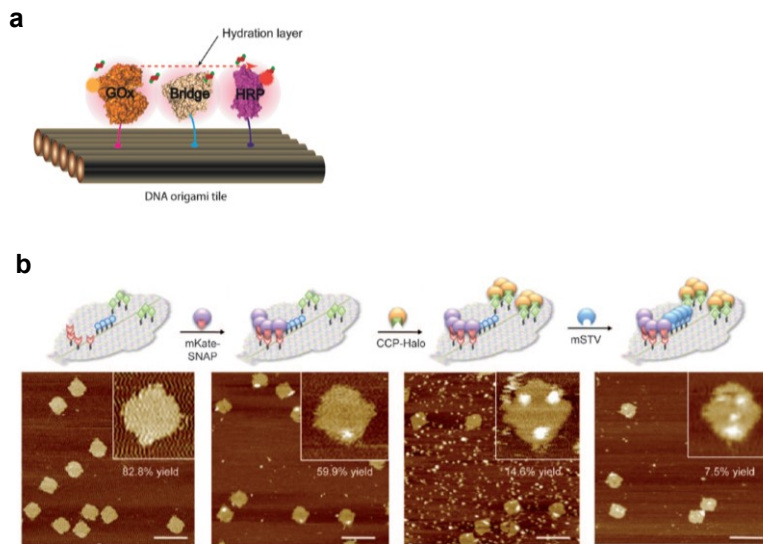


Figure 1-5: Examples for functionalization of distinct DNA nanostructures by means of covalent approaches. **(a)** Two-dimensional DNA origami platform modified with glucose oxidase- (GOx) and horse-radish peroxidase- (HRP) and a bridge protein- DNA conjugate. **(b)** Example of applying the covalent and non-covalent approach in parallel using the “Snap-tag” (covalent protein conjugate mKate-SNAP) and “HaloTag” technology (covalent protein conjugate CCP-Halo) and finally, the biotin–streptavidin (STV) interaction, which is the most widely used non-covalent functionalization of DNA nanostructure surfaces (scale bars in 100 nm). Images adapted with kind permission from [63;65].

Non-covalent protein binding

Nature uses various weak non-covalent interactions in a defined geometrical arrangement to confine specific substrates. For that reason, the *non-covalent* attachment approach, through DNA specific protein binding motifs [66;67], internalized ligands [68] or aptamers [69] has gained ever greater impact in this research field (figure 1-6). A lot of scientists focused their attention on the application of DNA aptamers for the evaluation of molecular recognition events and the development of biosensors. Rinker *et al.* for example internalized two DNA thrombin binding aptamers, TBA1 and TBA2 into a planar DNA origami platform, to induce their specific binding to two electropositive parts of the protein surface [70;71]. This enabled to control the optimal aptamer-to-aptamer distance for bivalent immobilization of the protein thrombin and analysis of this event at the single molecule level. This study revealed the capability of using designer DNA origami structures to construct complex and interactive biomolecular systems [69]. In other studies, DNA aptamers were integrated to perform dynamical re-configuration upon addition of an external trigger. At the initial state two parts of the construct were connected by an aptamer and its complementary strand. The addition

of a target specifically recognized by the aptamer sequence induces its binding to the target and therefore its dehybridization from the complementary strand, with consequent release of the connection between the two parts of the DNA construct. This mechanism was used in several studies to construct aptamer-encoded logic gates [49] or controlled release of molecules caged into a DNA nanostructure [72] or for the development of mechanochemical sensing systems [73]. Additionally, DNA origami could be implemented as platforms to immobilize DNA recognition motifs with the intend to analyze the binding and processing mechanism on the single molecule level by means of high-speed atomic force microscopy.

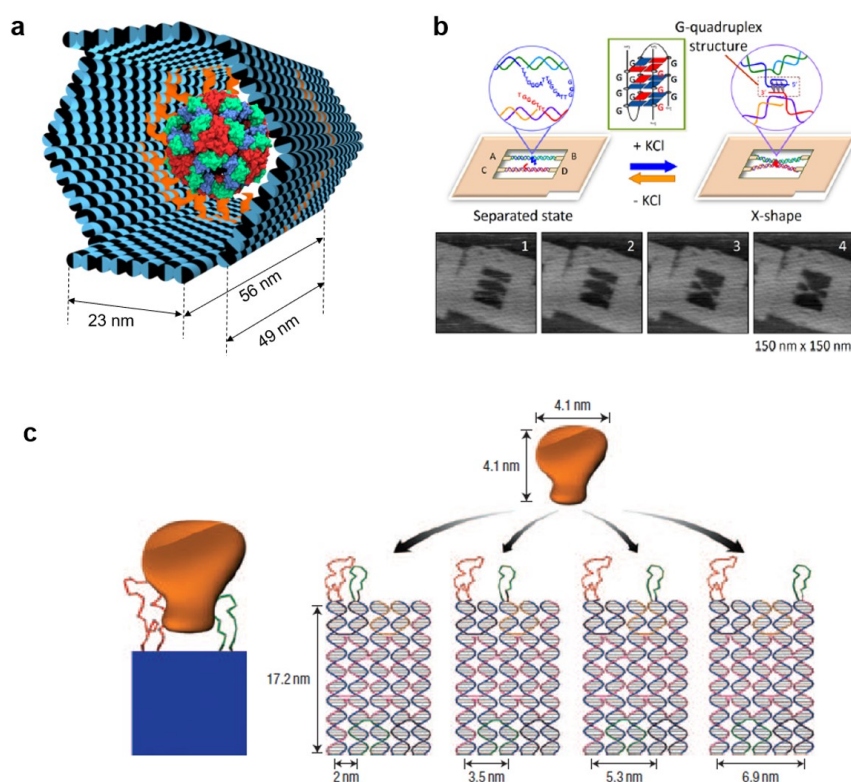


Figure 1-6: Examples for functionalization of distinct DNA nanostructures by means of the non-covalent approach. **(a)** Supramolecular ligands decorated on the inner surface of a DNA cage lead to successful encapsulation of the target protein. **(b)** Demonstration of correct G-quadruplex formation by means of DNA nanotechnology and multivalent protein binding on a two-dimensional DNA array **(c)**. Images adapted with kind permission from [68;69;74].

In this way, scientists could reveal the importance of DNA relaxation and bending in base-excision repair events [66] and evaluate the role of the topological state of the DNA substrates in recombination processes [47]. DNA nanoarchitectures have been also used for integration of specific DNA motifs, as molecular tags for transcription

factors [53] and site-specific DNA-binding protein adaptors [67;75]. Altogether, these data show that the attachment of target motifs to a DNA nanostructure in a non-covalent manner prevents the alteration of the natural properties of the selected target, giving the possibility to explore its characteristics in the native state.

1.3.2 Dynamic DNA nanotechnology

The previous sections clearly showed that the field of DNA nanotechnology offers the opportunity to build up biomimetic nanostructures with increasing complexity and spatial precision. However, several efforts have been done to develop reconfigurable systems, i.e. systems whose configuration can be manipulated in a predictable manner, exploiting for example the programmability of nucleic acid structures and in this way enabling to go one step further in the construction of truly-bioinspired compartmentalization systems [76]. Here again, the construction of molecular motors built completely out of DNA, has been pioneered by Ned Seeman's laboratory in 1999 [77]. He and his coworkers were able to construct a molecular machine built up by two simple double-crossover (DX) molecules connected by a double helical linker. The molecular motion of the device was induced by the addition of cobalt ions, triggering the transition from the B- to the Z-form of the DNA. This movement was monitored by fluorescence resonance energy transfer spectroscopy (FRET) and signed the beginning of dynamical DNA systems. Right after that, several researches followed this idea. For example Yurke *et al.* presented a reconfigurable DNA system, driven by the DNA molecule itself as a 'fuel' for the operational process [78]. The conversion between the different configurational states was driven by a mechanism called single-strand displacement, which is based on the strand invasion of a complementary strand, leading to the formation of a more stable duplex. A summary of this working principle is given in figure 1-7. This work founded the bases of the so-called dynamical DNA nanotechnology, applied in a lot of following research studies for the development of DNA-based nanomotors [41] and DNA circuits that simulate complex natural systems [43]. Applying this principle, it was possible to construct DNA nanostructures which undergo structural reconfiguration between different states, in a precisely controlled and directed fashion, opening the way to several exciting applications [78]. Few years after the study of Yurke *et al.* [77], DNA walkers have been developed, which walk directionally along a predefined DNA trajectory and whose steps are triggered by an external input [79-83], enabling also numerous states of configuration. However, a remarkable hindrance of

this strategy is the crowding effect due to the produced waste strands, which limits the functioning of the machine lowering the number of maximal possible cycles. Efforts to overcome this burden led to alternative techniques, where the output of the first state serves as input for the next state, allowing to construct more complex nanomachines, with higher cycling efficiency [78;79].

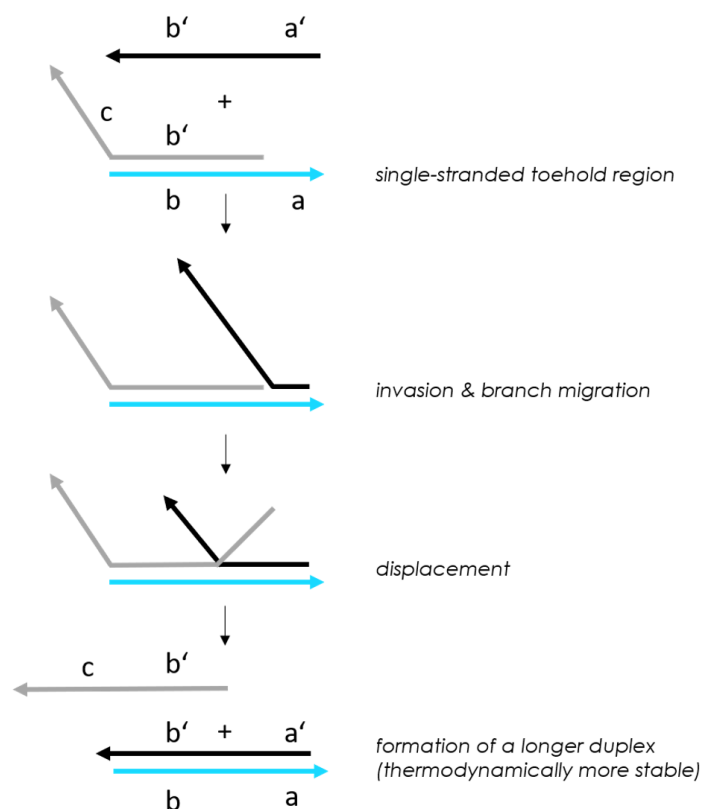


Figure 1-7: Toehold-mediated single strand displacement. *a* is complementary to *a'*, *b* is complementary to *b'*. The black strand binds to the single stranded toehold region on the turquoise strand (region *a*), and then in a branch migration process across region *b*, the grey strand is displaced and freed from the complex. Reactions like these are used to dynamically reconfigure or assemble nucleic acid nanostructures. In addition, the black and the turquoise strands can be used as signals in a molecular logic gate by fluorescence labeling techniques.

Based on these works, several progresses have been made in the field of dynamic DNA nanotechnology. One work, which deserved to be mentioned, is the study of Meng *et al.* [79]. They built a fully synthetic, autonomous chemical system, capable to synthesize programmable oligomers with defined sequences, thus mimicking the working mechanism of the ribosome and demonstrating the overall importance of kinetic control of chain-reactions using a simple DNA construct. In another work, Song *et al.* succeeded in tuning the energy landscape of a specific reaction in a predictable way. They achieved long-range-configurational changes by addressing local regions of connected units and triggering a domino-like effect from one unit to the adjacent ones [80]. This resulted in a controllable dynamic behavior of the whole DNA array, demonstrating that the future of DNA nanotechnology is without any doubt bright: integrating more complex structures with dynamic pathway circuits one can envision to engineer a

precise spatial and temporal organization of information propagation with a resolution of only few nanometers.

1.3.3 Role played by the surrounding environment

Distinct static and dynamic biomimetic nanostructures of various sizes and dimensions were developed, relying on the approaches presented above to specifically enable the loading of a selected cargo [53;72;81]. Dynamic 3-dimensional cage systems, additionally offered the possibility to undergo reconfiguration events upon external stimuli, serving as new transport systems for specific internalized cargos [33;82;83]. However, once the suitable system is developed the question which still remains is whether the DNA surrounding environment affects the stability and activity of the covalently or non-covalently internalized protein(s). Recently, there have been a lot of studies dealing with this question, and all of them consistently show that efficient binding of specific enzymes/proteins to DNA scaffold alters the enzymatic activity of the single DNA-enzyme conjugate or of the enzymatic cascade. Until now there are two main hypotheses for the explanation of this effect. From the one side, the origami platforms support correct spatial orientation of the conjugated enzymes and therefore bring the proteins in close proximity, thus facilitating substrate channeling. For example, Zhao *et al.* developed a three-dimensional DNA box system to successfully orientate glucose oxidase (GOX) and horseradish peroxidase (HRP) within the cage, driving efficient substrate channeling between them, which resulted in an enhanced substrate turnover number [33]. Just recently, the group of Andersen, constructed a protein-DNA-encapsulation system to control the enzymatic activity of the enclosed enzyme through regulation of substrate flux to the protein. For this purpose, they developed a method to open and close the cage system upon an external trigger [83]. Contrarily to this “orientational” hypothesis, Hess and coworkers postulated that the lower local pH, rather than the DNA scaffolding effect, is affecting the intrinsic activity of the DNA-enzyme conjugates by creating an optimal environment for catalytic performance of the enzyme [84]. This is in full agreement with what Goldstein *et al.* observed by evaluating the enzymatic behavior of a trypsin derivative embedded within a polyelectrolyte carrier [85]. In another hypothesis, the electrostatic potential near the DNA surface is believed to generate an ordered layer of water molecules that stabilize the caged protein. Alternatively, H-bond interactions between the DNA, the protein and the corresponding substrate may support the substrate binding as a consequence of favorable

conformational orientations. Finally, the surrounding DNA cage may act as a protective envelope, defending the protein against external influences and thus enhancing its catalytic activity [86-89]. Overall this shows that, until now, the influence of DNA caging on proteins is not fully understood and issues regarding this basic question still need to be solved and clarified.

2 Objective of the thesis

Compartmentalization is a key feature of living systems, which enables to control cell metabolism through the physical separation of reactions and chemical species into specialized vessels. An intriguing challenge of synthetic biologists is the realization of artificial compartments which mimic the structure and function of their natural counterparts but may display additional customized properties. One approach to achieve this goal relies on DNA nanotechnology. This method exploits the simple Watson-Crick code to construct nanosized objects made entirely of DNA. In the past few years, many brilliant examples of DNA-based nanocages have been realized for the spatial confinement of proteins or nanoparticles. However, many of those cargo-loaded DNA nanostructures are static, that is, they basically serve as structural frameworks for the precise positioning of molecules. In this sense, they lack an essential property of natural compartmentalization archetypes, i.e. the capability to undergo dynamic transformations in response to external events. Indeed, structural changes are constantly taking place within and between cellular compartments to allow for the spatial rearrangement of internalized components, their mutual interaction, efficient transport and release to other cellular locations. Thus, truly bio-inspired compartmentalization systems should provide not only a structurally confined space for isolation of a chemical event, but also be able to actuate dynamic operations in response to environmental changes. In other words, they should be reconfigurable. DNA nanotechnology offers also this possibility. Nevertheless, application of reconfigurable DNA nanostructures to address biological questions is only at its beginning and their use as biomimetic compartmentalization systems still remains largely unexplored. The purpose of this project is to address this challenge. In particular, the questions tackled here are (i) the mechanism of reconfiguration, which should be efficient, fast and possibly reversible; (ii) the loading mechanism towards a desired protein target, which should be “tailored” in the sense that one specific DNA chamber is designed to host a single kind of guest and finally, (iii) the effect of the surrounding DNA “environment” on the stability and activity of the internalized protein. The final goal is to develop a tool for selective encapsulation and manipulation of desired molecular cargos. In this way, artificial nanovessels can be created for the storage and delivery of materials at precise cellular locations and nanofactories can be engineered to perform simple chemical reactions in their inner cavity, thus emulating some of the fundamental properties of natural compartmentalization systems.

3 Results and Discussion

Since Richard Feynman's initial talk in 1959 several visions became reality [1], showing that the rapid growing field of nanotechnology is a powerful tool for the analysis of biochemical/biophysical processes (section 1.3). The enormous progress in this research area nowadays allows to achieve high control of chemical processes at the single molecule level with the advantage of temporally manipulating matter with a spatial resolution of few nanometers. This enabled to gain more insight into the basic mechanism of natural self-assembled systems and man-made constructions, paving the way to various applications, previously only hardly imaginable [57]. One of the most brilliant examples of nanotechnology in nature is probably the DNA molecule itself, whose simple structure and four-letter code is responsible for storing and transmitting the information necessary for life. DNA nanotechnology, pioneered by Ned Seeman in the early 80's [8], uses this fundamental property of DNA to build materials. In particular, one research area uses DNA nanotechnology to mimic the self-compartmentalization strategy adapted from nature with the aim to construct synthetic, supramolecular hosts to stabilize reactive intermediates [90] and catalyze reactions [91]. Using this approach, self-assembled constructs with molecular addressability and predefined shape have been developed [52], allowing to build nano-compartments of flexible size, mechanical properties and loading capability for specific targets of interests [33;49;53-55]. This, in combination with fluorescence-based methods offers new analyzing perspectives as it is a non-invasive methodology and the fluorescence signal can be used as an *in-situ* reporter with superior time resolution [92-94].

Despite the rapid development of that research field and the realization of DNA cages [68], and transport systems [72] inspired by their natural counterparts, i.e. lipid vesicles [95], viral capsids [96] or bacterial microcompartments [97], only a few studies, until now, focused on the biophysical characterization of dynamic compartmentalization systems capable of reversible structural reconfiguration.

We here describe a reconfigurable DNA origami device with modular and programmable size, i.e. a system with dynamic operational characteristics that can be actuated in a trigger dependent fashion. At this purpose, a quasi-planar 2D-origami structure was designed, which assembles during a defined temperature gradient into a rectangular shape. The structure consists of two halves linked by an unpaired scaffold segment at the top and bottom extremity. Due to the circular folding pathway, the two halves are joined by 18 small hairpin loops tethered and aligned along the seam of the structure.

These motifs can be manipulated in a trigger dependent fashion by means of a mechanism called strand displacement, lending to the whole structure its dynamical, mostly reversible properties [93;98-100]. The collective movement of all motor units led to a global transition of the structure resulting in defined states (named here as open (O), closed (C) and reclosed (RC)), which were characterized by means of atomic force microscopy (AFM) and gel electrophoresis (section 3.1). However, down to the present day, the employed forces of those kind of molecular motors were investigated only for ensembles of freely diffusing motifs [101-103] or for individuals hairpins using single molecule analysis [93;94;104-112]. In this study, instead, the purpose is to analyze the mechanical properties of a precise *ensemble of organized motors* through their tethering to a DNA origami architecture. The coordinated action of such motors was investigated by thermal-dependent FRET spectroscopy (3.2). The idea is to understand how mechanical properties in general can be gathered and manipulated on the nanometer scale, leading to fundamental information for the realization of more sophisticated nanomotors and for the comprehension of complex natural systems. Consequently, after characterization of the forces applied by the collection of hairpins, the operational mode of the device was used to mechanically unfold a defined molecular architecture placed in its inner cavity (section 3.2.5).

Beside this, the reconfigurable device has been upgraded to allow the programmable formation of more than two states. By the strategic positioning of different kinds of triggerable hairpin loops in series, it was possible to generate a four-state device (section 3.1.2). Thus, the inner space of the nanocompartment could be actively controlled in order to affect the intermolecular distance between cargo-specific, internalized ligands, eventually allowing to load distinct molecules with variable shapes and dimensions. Bock and coworkers [71] described two G-quadruplex DNA aptamers, which specifically bind to the serine protease thrombin. The choice here of this ligand-protein system relies on the fact that (i) the 3D structure of the complex is well known, (ii) the binding affinity of the two aptamers to the target protein are also well described in the literature, (iii) the proteolytic activity of the protein towards known substrates is also well characterized and, most importantly, (iv) encapsulation of the thrombin/TBAs complex within the DNA origami frame would allow to investigate the effect of different geometric parameters on the binding affinity and proteolytic activity of the protein. The protein indeed displays two binding electropositive exosites at opposite sides of its outer surface. These were targeted by the two G-quadruplexes placed at different

intermolecular distances and with distinct degrees of rotational freedom at the opposite edges of the inner cavity of the DNA origami frame and pointing towards the center of the structure. The dimensions of the protein thrombin together with the relatively high stability of the ligand-protein interaction enabled monitoring the binding event by standard gel electrophoresis and single-molecule AFM imaging. In addition, enzymatic assays enabled to evaluate the influence of the DNA cage and ligand design on the proteolytic activity of the enzyme, revealing still undisclosed properties of such host-guest complexes, which are of great interest for the scientific community, both for improvement of basic understanding and for potential biotechnological applications (section 3.3).

3.1 Design of the programmable and modular DNA host

The idea of this study was to engineer a DNA compartmentalization host, capable to perform specialized functions and to specifically confine distinct nanoarchitectures within its cavity. At this purpose, a DNA origami construct of rectangular shape containing an adaptable inner cavity was designed (see section 4.2.1, figure 4-1). Different numbers and types of small, switchable hairpin features were integrated into the seam of the rectangular shape, enabling to program the size of the inner cavity and resulting in four different constructs (0 = no hairpins, I = one set of hairpins, II = two identical sets of hairpins and III = two different sets of hairpins). The serine protease thrombin was then encapsulated inside the inner cavity of the structure by means of one or both TBAs anchored to the edges of the cavity in different spatial configurations (named here as D0, D1, D2, D3S and D3L). For detailed description of the different systems and designs and the mechanism responsible for the reversible reconfiguration process, please see section 4.2.1.1, figure 4-1 and figure 4-7. In the following chapters (section 3.1.2 and 3.3.3) all systems were characterized by AFM imaging (4.2.5.2) and gel electrophoresis (4.2.5.1) [44;113].

3.1.1 Topographical characterization using streptavidin as marker

The entire characterization of the reconfiguration process as well as the analysis of the thrombin loaded DNA origami constructs could be efficiently evaluated by using the interaction of biotin/streptavidin as a topographical marker and analyzing the sample at the single molecule level, using AFM [57;63]. The molecule biotin binds with a highly specific affinity to the protein streptavidin. DNA origami constructs, specifically quasi-

planar structures, can be modified with biotinylated oligonucleotides, oriented orthogonally to the origami plane. The interaction of streptavidin with the biotin molecule can then be used for topographical mapping of the origami surface, permitting to differentiate between the left and the right side of the device by AFM imaging. This tool was used in design D0 to distinguish which aptamer is binding to thrombin (TBA1 on the left side or TBA2 on the right side; figure 4-7).

In addition, the dynamic characteristics of the devices were also analyzed. Different amounts of small switchable hairpin loops were tethered into the seam of the structure. These dynamical features can be addressed with complementary “fuel” strands (orange). The hybridization of the fuel oligonucleotide to the hairpin motif of the compact closed device leads to a transition along the helical axis and to formation of a more stable double helical domain (open state), resulting in an increased size of the inner cavity (for more details see section 4.2.1.1). The fuel oligonucleotides can be as well modified with a biotin molecule at the 5'-terminus, enabling the visualization of the opening process upon streptavidin addition (visible as a change in the height profile of the structure during AFM imaging). Furthermore, the dynamic operational mode can be evaluated as a change in the electrophoretic mobility during gel electrophoresis. A schematically illustration of the described analyzing tool is given in figure 4-8.

Unfortunately, commercially available streptavidin shows high aggregation rates, making it often unsuitable as topographical marker. A method for the production of a modified streptavidin protein (including only the amino acids sequence 16-133) was therefore established, which circumvents this drawback and allows the use of the protein as a topographical marker during AFM imaging (for more details see section 4.2.2.1).

Figure 3-1 **(a)** shows a Western blot analysis of equal concentrated streptavidin samples taken at different timepoints after IPTG induction during an expression analysis experiment. The continuous rise of the band intensity is typical of protein expression initiation. Commercially available streptavidin served as control (CTR). The difference in electrophoretic mobility was a hallmark for the reduced amino acid sequence of the streptavidin variant compared to the control protein. The data showed successful expression of streptavidin and provided incentives for further development of a refolding and purification protocol of the truncated streptavidin protein.

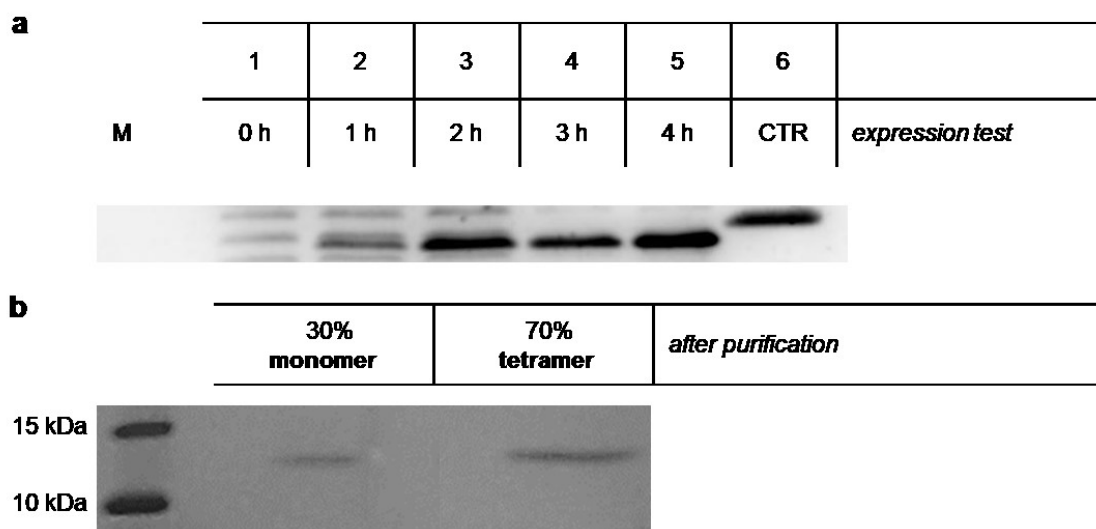


Figure 3-1: Characterization of the modified streptavidin protein (see section 4.2.2.1) by Western blot analysis (chapter 4.2.5.1). **(a)** Equally concentrated samples obtained at different timepoints were examined to evaluate the correct initiation of protein expression. The commercially available streptavidin served as a reference control (CTR). **(b)** Identification of the purified truncated streptavidin protein after correct refolding and precipitation at 30% and 70% $(\text{NH}_4)_2\text{SO}_4$ saturation. Running parameters: 120 V for 1 h at RT with 15% resolving and 5% stacking gel in 1x SDS running buffer. Lane M contains a low-range protein marker (1.7 to 40 kDa).

Therefore, the inclusion bodies (IB's) were isolated, denatured and the protein was refolded. Western blot analysis showed that the protein was successfully isolated by precipitation in $(\text{NH}_4)_2\text{SO}_4$ 30% (monomeric streptavidin) and 70% (tetramer) (figure 3-1, **(b)**) and satisfactorily purified after the refolding process. The applicability of this protein batch for topographical purposes is given in E Supplementary Information, figure e-1.

3.1.2 AFM and gel electrophoresis analysis of the DNA origami constructs

Particularly crucial for further investigation studies as well as applications of the presented DNA origami constructs, is the correct assembly of the devices as well as the precise functioning of the proposed reconfiguration process. In this section, all constructs (0, I, II and III) with respect to their operational characteristics upon fuel and antifuel addition were evaluated by means of AFM analysis (4.2.5.2) and gel electrophoresis (4.2.5.1) (mechanism and design are described in detail in the materials and methods section 4.2.1.1).

AFM imaging was chosen to characterize all modular origami constructs (0, I, II and III), due to its high spatial resolution capabilities. In figure 3-2 representative AFM

images of construct 0 and construct I, in either configurational state is presented. Remarkable here was the visualization of the unpaired scaffold segments at the top and the bottom extremity of the structure, which were designed to lend the structure a higher degree of flexibility and to allow the two parts of the device to move apart during the mechanical operation driven by the DNA-induced conformational transition (marked by the white arrows in figure 3-2). By close inspection of the images, it was possible to distinguish the seam of construct 0 (upper row, closed), which appeared to be more compact than the seam region of construct I. This is likely due to incorporation of the small molecular motors at the central seam connecting the two halves of the structure (lower row, closed).

Hybridization of the fuel strand to the closed tethered hairpins of construct I triggers the translational movement along the helical axes forming more stable double helical domains (open state of the device), as clearly visible during AFM analysis (lower row, middle, open).

Further visualization of the opening mechanism was achieved by the application of 5'-biotinylated modified fuel strands. Hybridization of these fuels to the closed tethered hairpin motifs, followed by addition of the truncated streptavidin protein (see section 3.1.1) led to the appearance of bright spots under AFM imaging, which indicates a change in the height profile of the structure (AFM image lower row, open + strep). High-resolution images of construct I additionally confirmed a distinct discrimination between the closed and the open form (upper row, zoom in on the right side).

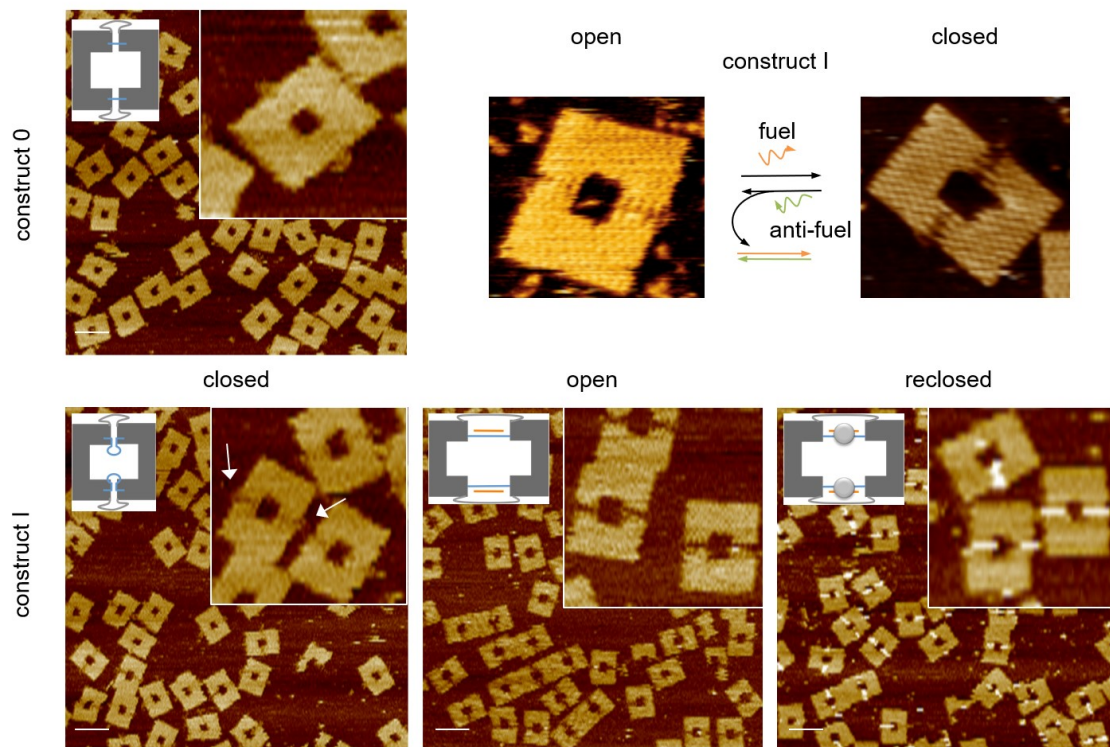


Figure 3-2: AFM characterization of construct 0 (closed, upper row) and I (lower row and zoom in upper row open/closed). The designed unpaired scaffold segment at the top and the bottom extremity is clearly visible, marked by the white arrows. The difference between the more compact seam of construct 0 (no integrated hairpins) and the more extended seam of construct I (one set of integrated hairpin loops) is evident, particularly at high resolution. Fuel addition to the close state of construct I (lower row, closed) triggers the translational movement along the helical axes, ending up with the formation of double helical domains (lower row, open), based on hybridization of the fuel strand to the complementary single-stranded hairpin loop. The opening process can be further visualized by using 5'-biotinylated fuel strands followed by direct addition of streptavidin, resulting in brighter spots along the seam, above and below the central cavity of the structure. This further proves correct hybridization of the fuel strands to the small switchable motifs integrated into the DNA origami seam (lower row, open + strep). For clarity, a schematic presentation of each samples is presented as small inset in all images. The streptavidin proteins are presented as a single grey circle. Analysis was performed in TEMg 1x buffer. Scale bars are 100 nm.

The correct functioning of these two constructs was additionally proven by gel electrophoresis (see figure 3-3, lane 1-6). Construct 0 was designed to feature no switchable motifs, analyzed in lane 1-3. The device was treated with biotinylated fuel strands followed by direct streptavidin addition. As expected, there is no apparent gel shift in lane 2 compared to lane 1 and 3. Identical treatment of construct I led instead to a significant change in the electrophoretic mobility of the sample, observable in lane 5 when compared to lane 4. This indicates correct hybridization of the biotinylated fuel strands to the integrated hairpin loops and further binding of the protein to the double helical

domains. To demonstrate the reversibility of the process (lane 6), the switch back to the initial closed state of construct I was achieved by adding antifuel strands fully complementary to the hybridized fuel strands, equipped with a short toehold. The electrophoretic mobility of the reclosed sample (lane 6) is similar to that of the closed state (lane 4), thus demonstrating the full reversibility of the reconfiguration process. This open-closed-reclosed cycle can be theoretically repeated several times, but the accumulation of waste strands (fuel/antifuel duplex) will “poison” the system, unless structures are immobilized on a solid surface and washing steps are integrated in between each cycle. Finally, matching with the theoretical estimation, an increase size of the inner cavity (figure 3-2) was visible.

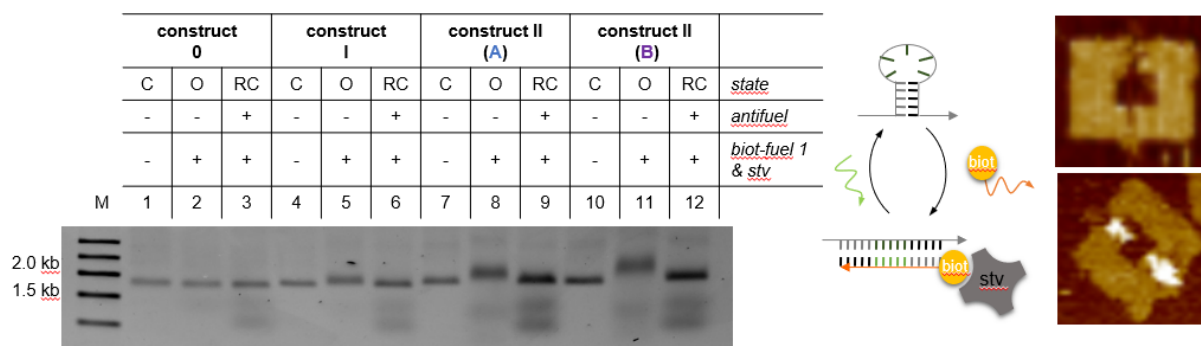


Figure 3-3: Visualization of the correct functioning of constructs type 0 (bearing no hairpin loops), I (bearing one set of hairpin loops) and II (bearing two identical sets of parallel hairpin motifs). All three constructs were analyzed in their initial closed state (C), in the open state (O) and in the reclosed state (RC). The band shift in band 5, 8 and 11 indicates the correct formation of the double helical domain upon fuel hybridization and binding of streptavidin to the biotinylated fuels. In contrast, construct 0 gave no electrophoretic mobility shift (lane 2). Adding fully complementary antifuel strands to the toehold appended fuel strands triggers the reconfiguration of the device to the initial closed state, as demonstrated in lanes 6, 9 and 12 (RC), characterized by an electrophoretic mobility similar to that of the corresponding closed samples (C) in lanes 4, 7 and 10. For clarification, an AFM image demonstrates the correct functioning of construct II (right). The difference between the two constructs II is the base sequence of the integrated inner segment A and B (design described in 4.2.1.1). Gel running parameters: 0.75% agarose, 2.5 h, 80 V by 4°C in TBEMg 1x. Lane M contain a 1 kb DNA ladder.

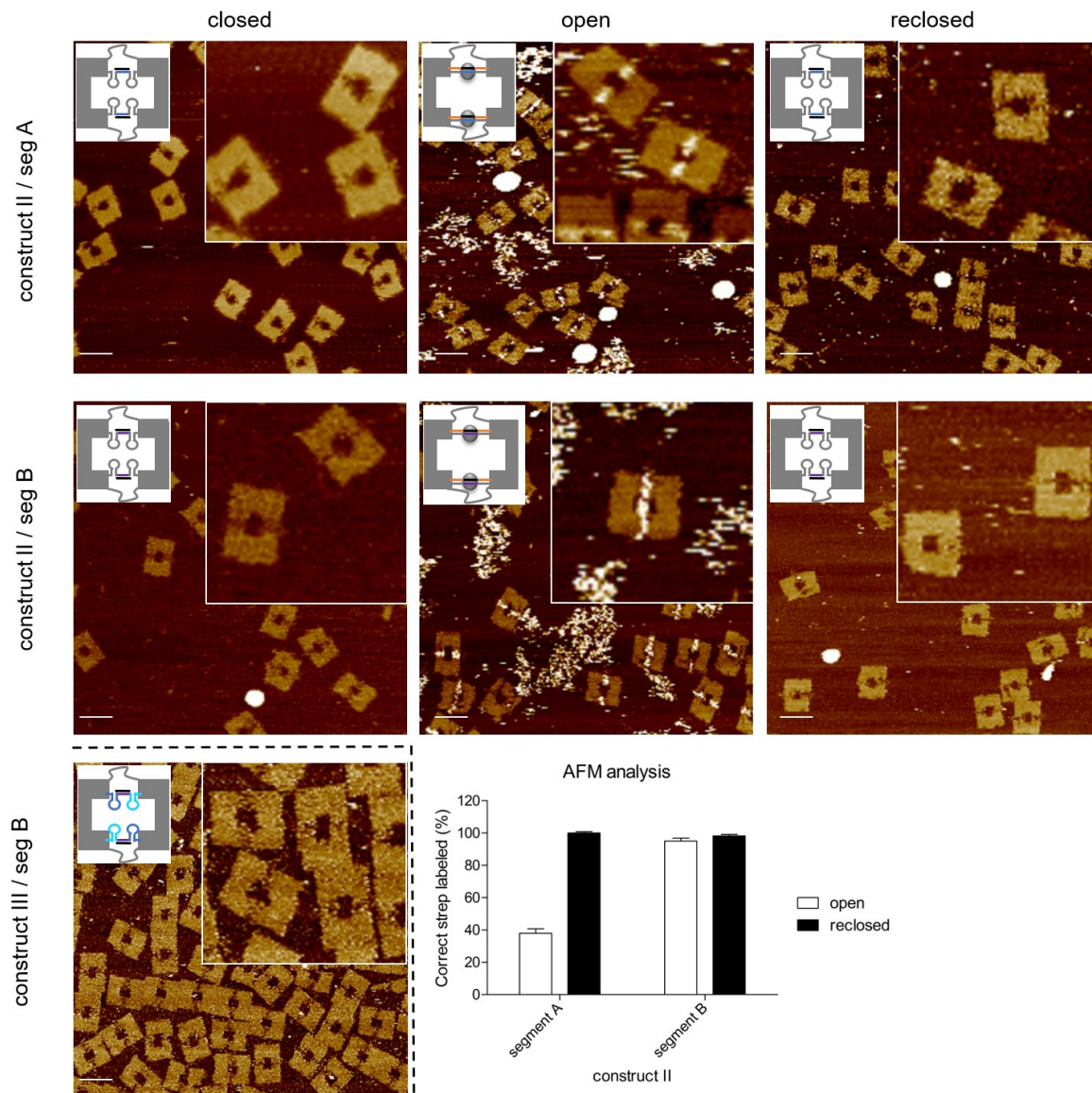


Figure 3-4: AFM characterization of construct II (upper and middle row) in the closed, open and reclosed state and construct III (lower row) in the closed state. These constructs contain two sets of hairpin loops in the central seam, separated by a short double helical region, of a sequence *A* (upper row, construct II / *seg A*) or *B* (middle row, construct II / *seg B*). The opening process is visualized by addition of toehold appended fuel strands containing a biotin at the 5'-terminus, followed by the addition of streptavidin and resulting in the appearance of the bright spots in the central seam (middle panels). Switching back to the initial closed state is achieved by the addition of fully complementary antifuel strands, which remove the protein-bound fuels from the seam (right panel). AFM analysis (mean value + SEM) revealed a higher opening yield for the structures containing the inner segment *B* (bar diagram, bottom row), which was therefore implemented in construct III (lower row, construct III / *seg B*). For clarity, a schematic presentation of each sample is presented as small inset in all images. The streptavidin proteins are presented as a single grey circle. Analysis was performed in TEMg 1x buffer. Scale bars are 100 nm.

Adding a second set of loops in series to the first one presented by construct I leads to an increased size of the inner cavity, enabling to place larger or multiple cargos within the structure. These constructs (II & III) were analyzed by gel electrophoresis (figure 3-3 for construct II and figure 3-5 for construct III) and AFM analysis (figure 3-4), and differed in the sequence of the integrated loops in series. Construct II contained two identical sets of hairpin loops, which could be simultaneously addressed by the same toehold appended fuel strands used in construct I to trigger the translational opening of the structure. This has been visualized by AFM (figure 3-4, upper and middle row) and gel electrophoresis (figure 3-3, lane 7-12), by adding streptavidin to the biotin-modified devices. As expected, the protein binds along the central seam sequences, visible as bright spots during AFM analysis (figure 3-4, middle panel, open) and resulting in a lower electrophoretic mobility of the samples (figure 3-3, lane 8 & 11 compared to 7 & 10). Disappearance of the protein due to addition of fully complementary antifuel strands demonstrates the correct reformation of the closed state of the device. This is evidenced by the disappearance of the streptavidin spots at AFM analysis (figure 3-4, right panel, reclosed) and the shifting back to the initial electrophoretic mobility of the closed samples (figure 3-3, lane 9 & 12 compared to 7 & 10). For stable connection of the two sets of loops in series, two different segments with its complement were used (seg A and seg B). AFM analysis of these two variants revealed a higher opening yield for construct II with the inserted seg B ($95\% \pm 1.9$) compared to seg A ($37.9\% \pm 2.9$). Interestingly, no significant difference during the reclosing events was observed (seg A: $100\% \pm 0.2$; seg B $98.3\% \pm 0.9$). Therefore, segment B was chosen to connect the two different sets of loops in construct III. This latter was also characterized by AFM imaging and gel electrophoresis (lower row, left, figure 3-4 and figure 3-5).

Construct III is a four-state device, each loop set can be addressed individually, leading to 2×2 states, specifically, fully closed (CC), partially open (OC and CO, depending on which of the two loops will be opened) and fully opened (OO), as schematically presented in figure 3-5 (a). This leads to a fully programmable device with various sizes of the inner cavity, which can be used to place different molecules, selectively and independently on distinct reconfigurations of the device. The correct assembly of this construct was proven by AFM imaging (lower row, left, figure 3-4) and the functioning of the device was proven by gel electrophoresis (figure 3-5). For this purpose, the hairpin motifs (named as 2 and 3) were addressed by the corresponding fuel strands,

previously labeled at their 5'-end with a FAM or a TAMRA molecule, respectively. Opening of hairpin 2 with fuel 2 was demonstrated by a FAM fluorescence signal (green, FAM-gel, lane 2 and 4), while opening of hairpin 3 with fuel 3 gave only a TAMRA fluorescence signal (red, TAMRA-gel, lane 3 and 4). Opening of both hairpin loops led to an overlay of both fluorescence signals (yellow, merge-gel, lane 4). The efficient reconfiguration of the device was demonstrated by the disappearance of all signals and the change in electrophoretic mobility (cfr, lanes 5, 6 and 7 respectively to lanes 1, 2, 3 and 4, in **(b)** of figure 3-5).

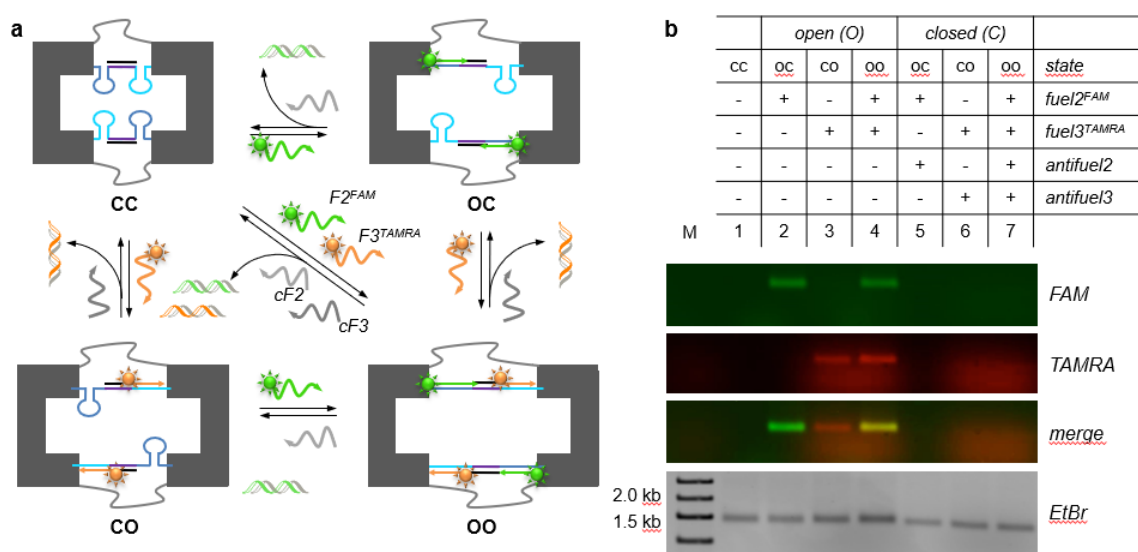


Figure 3-5: Demonstration of the reversible functioning of the four-state DNA origami device (construct III) bearing a second set of loops in series. **(a)** Each loop set can be addressed individually, leading to 2x2 states, specifically, fully closes (CC), partially open (OC and CO, depending on which of the two loops will be opened) and fully opened (OO). **(b)** The hairpin motifs (named as 2 and 3) were addressed by the corresponding fuel strands, previously labeled at their 5'-end with a FAM or a TAMRA molecule, respectively. Opening of hairpin 2 with fuel 2 was demonstrated by a FAM fluorescence signal (green, FAM-gel, lane 2 and 4) and while opening of hairpin 3 with fuel 3 gave only a TAMRA fluorescence signal (red, TAMRA-gel, lane 3 and 4). Opening of both hairpin loops led to an overlay of both fluorescence signals (yellow, merge-gel, lane 4). Gel running parameters: 0.75% agarose, 2.5 h, 80 V by 4°C in TBEMg 1x. Lane M contain a 1 kb DNA ladder and gel was stained with ethidium bromide (EtBr).

In summary it could be demonstrated that all designed structures could be assembled in high yields into their predicted geometrically and reconfigurable characteristics. In the following section, the mechanical properties and forces of the ensemble of the tethered hairpin loops were investigated with the intend to specifically use the generated forces to unfold a defined nanoarchitecture placed inside the inner cavity of the device (see section 3.2).

3.2 The collective behavior of spring-like motifs tethered to DNA nanostructures

Single stranded DNA hairpins can be assumed to be small switchable molecular motor units, with the capability to perform specialized dynamical functions upon an external trigger (demonstrated in section 3.1.2). Recent studies mostly investigated the dynamic characteristics of these switchable motifs when immobilized on solid surfaces or when freely diffusing in solution. In this work, a systematic analysis was performed to evaluate the performance of an ensemble of hairpin motifs tethered to a defined nanoarchitecture. At this purpose, temperature-dependent FRET spectroscopy was used (for more details see supplementary information and section 4.2.4.1).

3.2.1 Design and FRET labeling of the device

One of the fundamental questions of this thesis was: *“Is the tethering of small switchable hairpin motifs to a rigid origami frame affecting the performance of the individual motifs and can this be quantified?”* To address this question, the described systems (3.1.2 and 4.2.1.1) were used to evaluate the thermal stability of single hairpin motifs, tethered to different regions of an origami structure and surrounded by a distinct number of identical or different motifs, both in the closed and open state. Figure 3-6 (a) gives an overview of the various samples and constructs analyzed by means of temperature-dependent FRET spectroscopy. Two FRET reporters (FAM and TAMRA) were placed in near proximity at the 5'- and 3'- end of the embedded hairpin motifs and the global efficiency of energy transfer was monitored during the cooling and melting process, in both the single stranded (closed) state and more stable duplex (open) state. Important is, that the labeling strategy used allows to uniquely associate the change in FRET efficiency to correct integration/formation of the single stranded hairpin or duplex strand into the origami frame. As the hairpin themselves are not labeled, their formation in solution is not affecting the observed fluorescence signal. In total, four classes of constructs were analyzed, differing in the number/type of embedded hairpin motifs inside the origami frame (figure 3-6 (c)). Construct 0 is not reconfigurable, bearing no loops within the central seam of the device. It is therefore static. Construct I contains one set of identical hairpin motifs aligned along the seam of the device and results in a dynamic behavior similar to construct II and III. These two constructs contain two sets of hairpin motifs one next to each other (i.e. in series) and aligned along the seam sequence. Whereas construct II contains two identical sets of motifs, construct III is

characterized by two different sets of hairpin loops. Both sets are connected by a short stabilizing segment (see section 3.1.2 and 4.2.1.1). For all devices specific FRET samples were prepared (figure 3-6, **(b)**). Correct formation and functioning of the designed systems were proven by gel electrophoresis (see E Supplementary Information, figure e-2). All samples analyzed were indicated by two numbers: the first one describing the type of construct (from 0 to III) and the second indicating the position of the FRET labels along the seam, from the top to the bottom (1 to 18, bold, dashed lines figure 3-6). In a control sample, the FRET reporters were embedded in the middle of the origami structure on the left side (ctr, figure 3-6), i.e. far from the dynamical seam region of the device. In addition, the effect of the structural environment on the thermal stability of the loops was investigated by varying the positions of the FRET reporters as well as omitting selected hairpins of the analyzed set, indicated by an apex (dashed lines, figure 3-6). For clarity, sample I/15^{12,13}, represents construct I with one set of hairpin loops, whose FRET reporters were placed at position 15 of the seam and lacking the loops at position 12 and 13. This strategy will give information about the variation in the thermal stability of the single hairpin motifs in dependence of their spatial arrangement and surroundings.

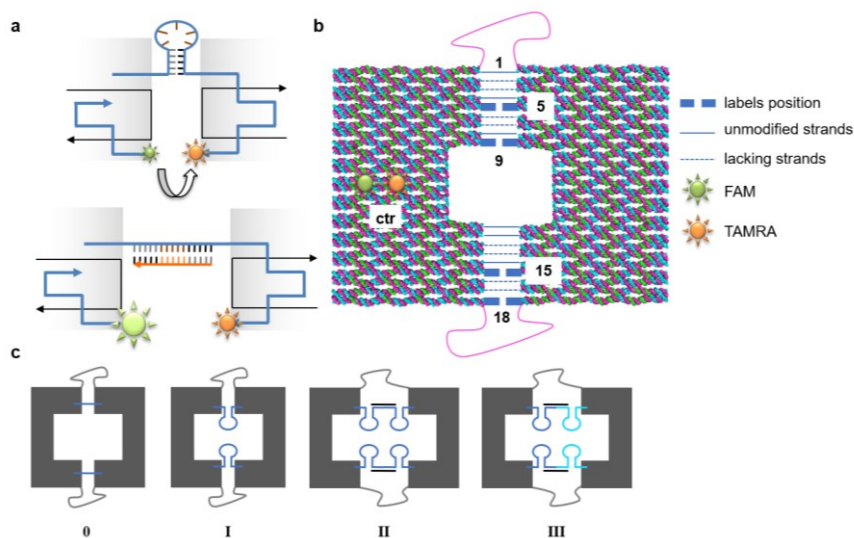


Figure 3-6: (a) Schematic illustration of the prepared FRET-thermal analysis constructs. In summary four classes of constructs were analyzed, containing different amounts and types of hairpin motifs tethered to the central seam of the device: construct 0 contains no hairpins, construct I bears one set of parallel hairpins, construct II and construct III feature, respectively, two identical and two distinct sets of parallel hairpins (c). To understand the effect of the structural environment on the thermal stability as well as the consequence to the mechanical properties of the motor units, the positioning as well as the number of total embedded hairpin loops and their geometric arrangement was varied (b).

3.2.2 Thermal stability of the devices

The cooling/melting curves for the systems described in 3.2.1 and obtained by temperature-dependent FRET spectroscopy were analyzed by van't Hoff analysis only when superimposable and of sigmoidal shape, because only when these two conditions are met, the process may be considered reversible and cooperative. The enthalpy and entropy change as well as the free energy change at 25°C was calculated for all suitable curves (calculation described in section 4.2.4.1).

The following figures (figure 3-7 to figure 3-9) display the FRET thermal curves obtained in this thesis. In particular, figure 3-7 summarizes the data for construct 0, the static construct, which is not reconfigurable. No remarkable change between the ctr samples could be observed, by comparing 0/ctr **(a)**, 0/ctr^{2,3,6,7} **(d)** and 0/ctr^{12,13,16,17} **(e)**. However, the FRET thermal profiles were extremely different when fluorophores were placed either at position 5, in the upper region of the structure, or 15, in the lower region of the device, (0/5 **(b)**: $\Delta G=50.9$ kcal/mol and $T_m=58^\circ\text{C}$; 0/15 **(c)**: $\Delta G=21.5$ kcal/mol and $T_m=53^\circ\text{C}$). This might be dependent on the tethering of the labels within different regions of the DNA nanostructure. This goes along with the results Wei *et. al* observed during their studies [114]. Their work revealed anisotropic thermal behaviour of origami structures, probably as a consequence of different “sequence environments” in the vicinity of the labels or local structural defects. Therefore, we assume that the difference in thermal stability observed for the 0/5 and 0/15 samples is based on the different sequence-dependent environments nearby the fluorophore labels.

This phenomena was not only observed for samples 0/5 and 0/15. The same tendency could be detected in construct I containing one set of hairpin loops aligned along the reconfigurable seam (figure 3-8 **(b)** I/5: $\Delta G=19.5$ kcal/mol and $T_m=52^\circ\text{C}$; **(c)** I/15 $\Delta G=16.6$ kcal/mol and $T_m=49^\circ\text{C}$). Comparing the thermal profiles of the two samples suggests that the labeled hairpin in device I/5 senses a higher degree of cooperativity than in I/15. Conceivably, this result may be associated to a more rigid and compact microenvironment in the upper area of the nanostructure, at least in the direct proximity of the labels.

In perfect agreement to that, the same behaviour was proven within sample I/9 **(d)** and I/18 **(e)**. These samples were designed to feature a limited anchoring surface compared to the other samples of construct I, enabling to evaluate the influence of a more flexible surrounding microenvironment. The labeling positions were placed on

the outer edge of the reconfigurable region of the device and therefore the reporters were fixed to a less extent to the nanostructure.

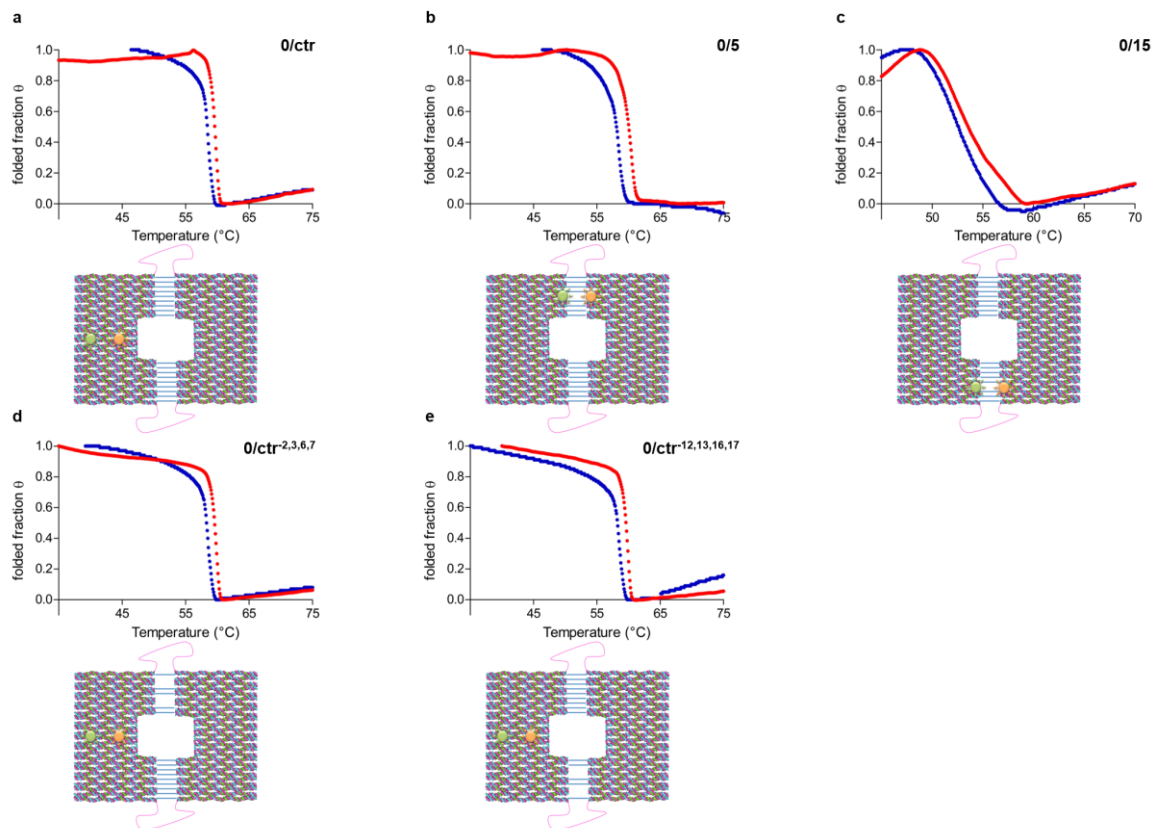


Figure 3-7: Construct type 0 is the most rigid structure analyzed during this study, containing no flexible hairpin motifs integrated along the seam sequence. The two FRET fluorophores reporters in this device were linked to the middle of the origami structure on the left side of the nanostructure (0/ctr) or along the seam, at position 5 (0/5) or 15 (0/15). Further control devices omitted seam staples at positions 2 to 7 (0/ctr²⁻⁷) or 12-17 (0/ctr¹²⁻¹⁷). The normalized FRET efficiency curves for the melting (red) and cooling (blue) process are reported.

This gave an hysteresis curve in case of sample I/9 and a monotonic transition for sample I/18, making these samples inappropriate for the evaluation by van't Hoff analysis.

In general, these data indicate that a sufficiently rigid anchoring surface and a stable structural microenvironment are necessary to allow an ideally reversible and cooperative thermal process. In support to this hypothesis, the control samples, bearing the FRET labels incorporated within the left half of the structure, display the highest values of free energy change (0/ctr: $\Delta G=82.2$ kcal/mol and $T_m=58^\circ\text{C}$ > 1/ctr: $\Delta G=71.4$ kcal/mol and $T_m=58^\circ\text{C}$).

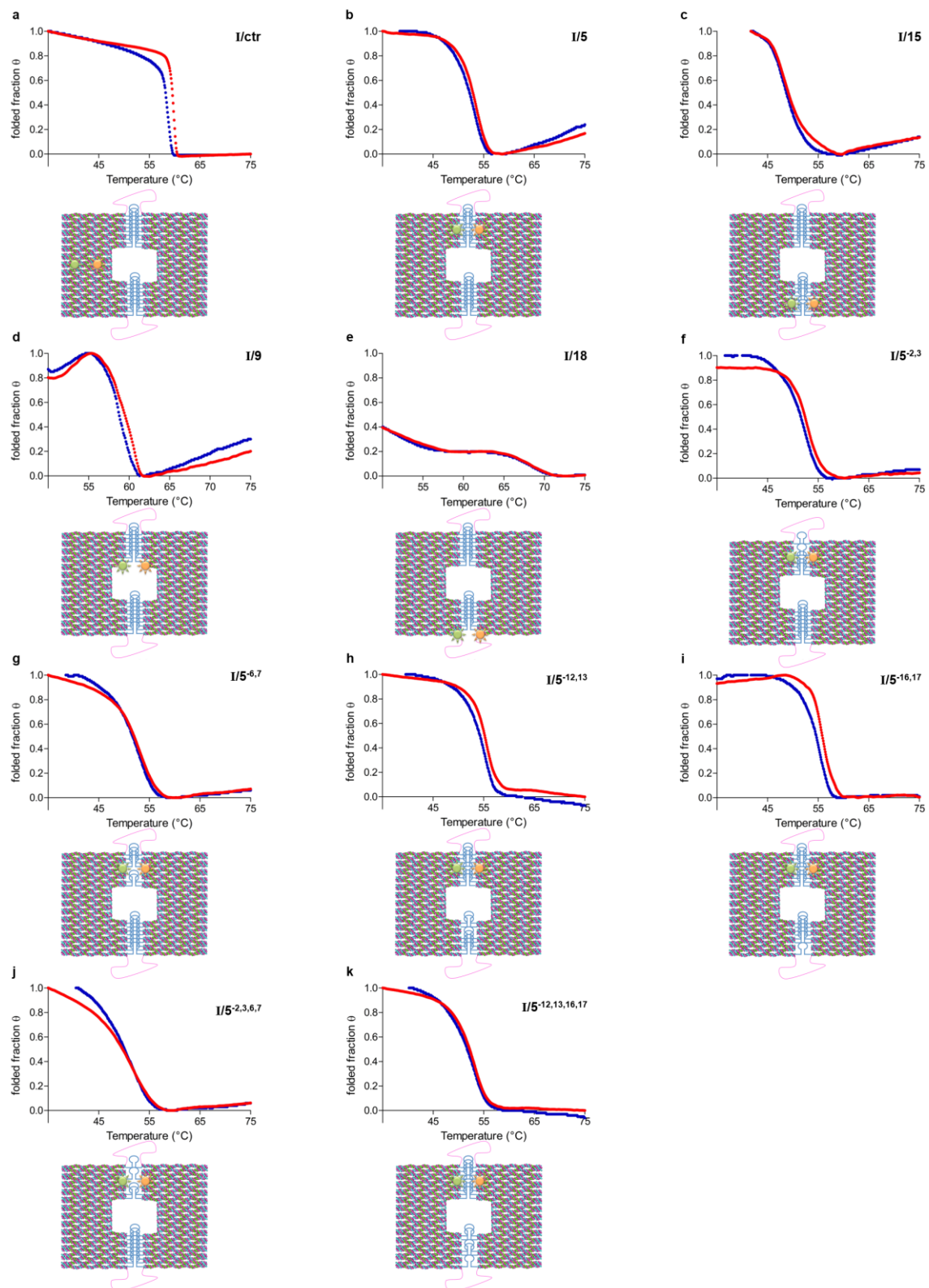


Figure 3-8: Curves obtained by temperature-dependent FRET spectroscopy for construct I, featuring one set of hairpin loops. The control sample contained the FRET reporters (indicated by the green and red star) on the left half of the structure, away from the reconfigurable region (a). In (b) and (c) the fluorophores were placed either at position 5 or 15 along the dynamical region. The apex represents the loops lacking during the analysis. I/5 was analyzed omitting two nearby strands above (f) or below (g) the reporters, or located on the opposite side of the structure (h, i), as well as four strands enclosed (j)

or distant from (**k**) the analyzed region. Construct I/9 (**d**) and I/18 (**e**) were not suitable for application of the van't Hoff analysis as they demonstrate either thermal hysteresis (**d**) or monotonic transition (**e**). Here, the reporters were positioned respectively on the inner and outer edges of the structures. The normalized FRET efficiency curves for the melting (red) and cooling (blue) process are reported.

Furthermore, integrating a second set of hairpin motifs adjacent to the first one, either identical (construct II (**a**)) or different to it (construct III (**b**)) decreases the thermal stability of the structures compared to construct 0 and I (schematic representation in figure 3-9), whereas the values of ΔG for those two systems were almost the same (7.8 kcal/mol \approx 9.7 kcal/mol). This may indicate an enhanced flexibility of the system most probably at the level of the inter hairpin connection.

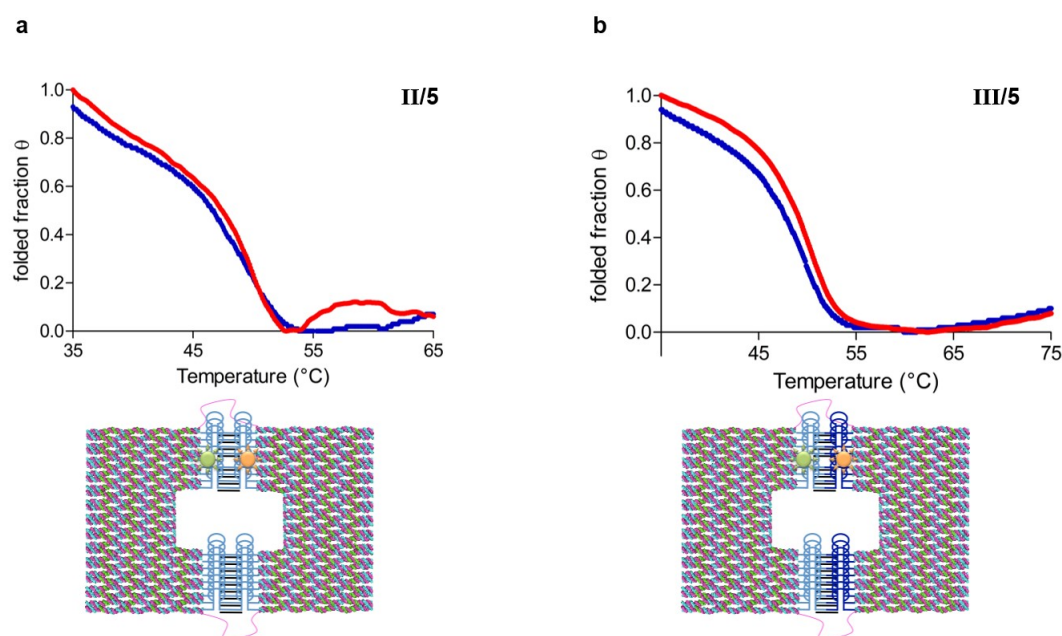


Figure 3-9: Constructs type II and III bearing two identical or two different sets of parallel hairpin loops along the seam (details of the design are reported section 4.2.1.1). FRET reporters have been placed at position 5 in both constructs (II/5 and III/5). The normalized FRET efficiency curves for the melting (red) and cooling (blue) process are reported.

To clarify the disparity in thermal stability between the samples labeled at position 5 or 15, a three-dimensional modeling of the structure using the CanDo software tool (figure 3-10) and a thermal-dependent UV spectroscopy experiment (figure 3-11) were performed. The algorithm of the CanDo software predicts the shape and the flexibility of the programmed DNA nanostructure in solution, expressed in root mean square flexibility (rmsf). This is represented in color-code, from a minimal (blue) to a maximal (red) relative value. The CanDo software, uses a mechanical model of the DNA molecule

that assumes the DNA double-helix as a homogeneous elastic rod with axial, twisting, and bending moduli, based on experimentally investigated data [115]. The results demonstrate that the integration of the hairpin motifs along the seam sequence **(b)** enhances the flexibility of the structure, but still remains symmetrically distributed around the seam when compared to the closed state of the device **(a)**. Consequently, the anisotropic nature of the different constructs and disparity in their thermal stability may be reasonably attributed to different sequence-dependent rather than geometrical microenvironments.

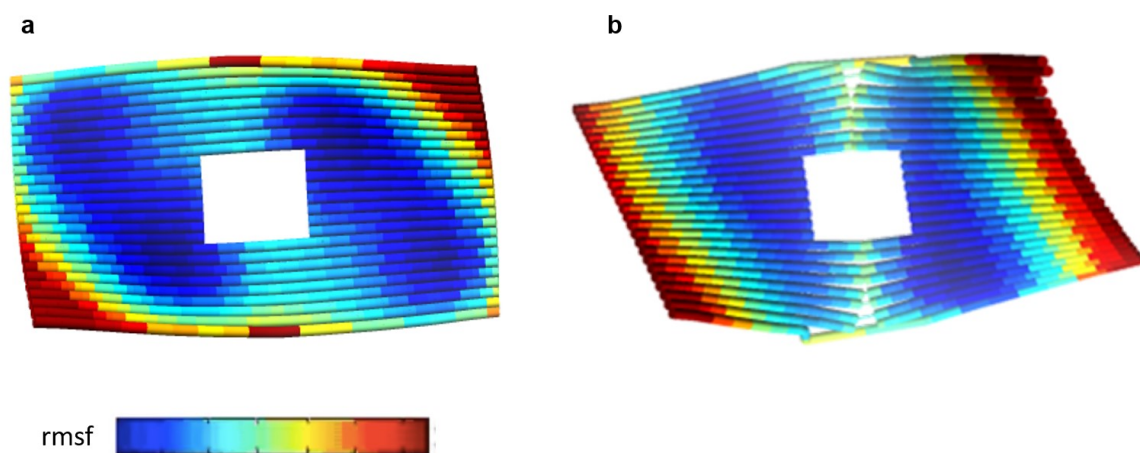


Figure 3-10: CanDo three-dimensional model of the presented DNA nanostructure, omitting **(a)** or featuring **(b)** the single stranded hairpin motifs tethered along the seam (<https://cando-dna-origami.org>). Shown here is the data obtained by an algorithm which calculates the structural flexibility of the device in root mean square flexibility (rmsf), from a minimal flexibility (blue) to a maximal (red), using experimental obtained geometrical parameters of the DNA molecule.

This highly thermal heterogeneity was further proven by UV spectroscopy experiments (figure 3-11). The obtained curves show high hysteresis behavior which underlines the non-reversibility of the process. This effect can be explained by the occurrence of different sequence-dependent regions within the origami nanostructure, resulting in different thermal properties.

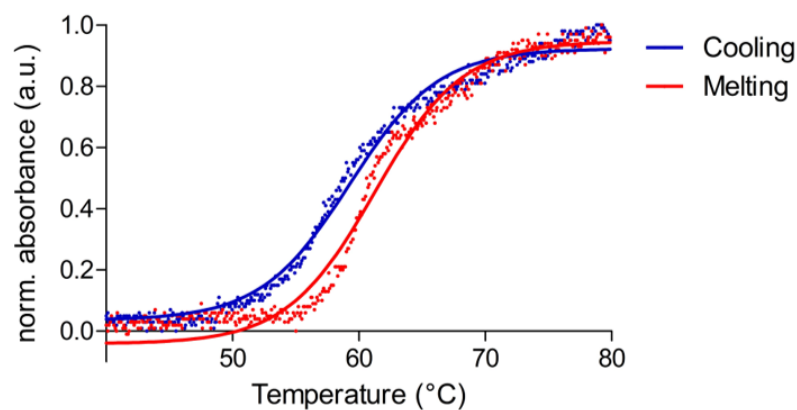


Figure 3-11: Normalized thermal cooling (blue) and melting (red) curve of sample I/5 analyzed by UV spectroscopy. Non-reversibility of the process is confirmed by the demonstrated hysteresis of the thermal transition. This effect may be based on different sequence-dependent regions within the origami nanostructure, resulting in different thermal properties.[114].

The ΔG and T_m values obtained for all constructs analyzed, both in the closed and open form are given in figure 3-12. The diagram reveals two interesting phenomena. (i) As expected, the reduction in the thermal stability of the samples is proportional to the number of single stranded hairpin features tethered along the seam region ($0/5 > I/5 > II/5 \approx III/5$ (**a**)). This means that a rigid seam connection as in construct 0, where no dynamical features were integrated inside the nanostructure is thermally more stable than similar a connection bearing one set or two sets of hairpin motifs (construct I, II and III). However, insertion of hairpin motifs is necessary for the operational reversibility of the presented nanoarchitecture, although the prominent level of flexibility of the molecular motors appears to destabilize the device. (ii) A sufficiently rigid anchoring surface is important to visualize the thermal transition and to evaluate the influence of the structural surroundings on the thermal stability of the labeled motifs (investigated for construct I/5 (**b**)). The results of these experiments demonstrated that the removal of strands around the fluorescent reporters destabilizes the structure and that this energy depletion is proportional to the number of lacking strands ($I/5 > I/5^{12,13} \approx I/5^{12-17}$) and to their vicinity to the labels ($I/5^{16,17} > I/5^{12,13} > I/5^{6,7} \approx I/5^{2,3}$), supporting the role of the surface tethering.

Upon completion, the thermal stability of the open device in the duplex state was evaluated. The data of free energy change for a free duplex in solution were obtained with the Mfold software tool, using the same experimental conditions. The data gained for the duplex freely moving in solution were almost comparable with the fully anchored duplex (free in solution: -21.4 kcal/mol and I/5: $\Delta G = -25.4$ kcal/mol), giving evidence

that tethering the open duplex to the origami support did not significantly enhance the thermal stability of the duplex system. Furthermore, going along with the results obtained for the closed single stranded hairpin motifs, the thermal stability of the structures decreases for duplexes tethered within less stable regions of the device and/or by reducing the number of duplexes surrounding the labeled region.

One open question, still remaining, is the observed overall increase in thermal stability of the open duplex form (see table 3-1 and table 3-2). One possible hypothesis is based on the kinetic effects induced by the organized DNA origami environment: the melting of a duplex might be partially prevented/delayed due to momentary (partial) hybridizations by other fuel-strands, which are locally available in high amounts as released from the neighboring hairpins. To test this hypothesis an experiment was prepared using five different types of construct I/5 (maximally tethered) in the duplex form, differing one another in the initial fuel concentration used to attain them. The energetic parameters of the thermal denaturation/renaturation process were extracted for all samples (**c**). The results demonstrate that by increasing the fuel concentration, the free energy change of duplex denaturation decreases. This is opposite to the hypothesis postulated above and indicates that the interpretation of the results is not biased by such a possible effect. Although the energy landscape of the whole system appears to be complex and dependent from many experimental and design parameters, the significance of this work relies in the evidence of a cooperative effect between spatially near and organized DNA motors and is based on comparative values between the same collection of motifs in identical experimental conditions and differing only in their structural contexts. Investigating the effect of other experimental parameters, such as temperature, pH, DNA concentration, ionic force and others, may probably lead to a much more complex picture, which is at the moment beyond the scope of this present study.

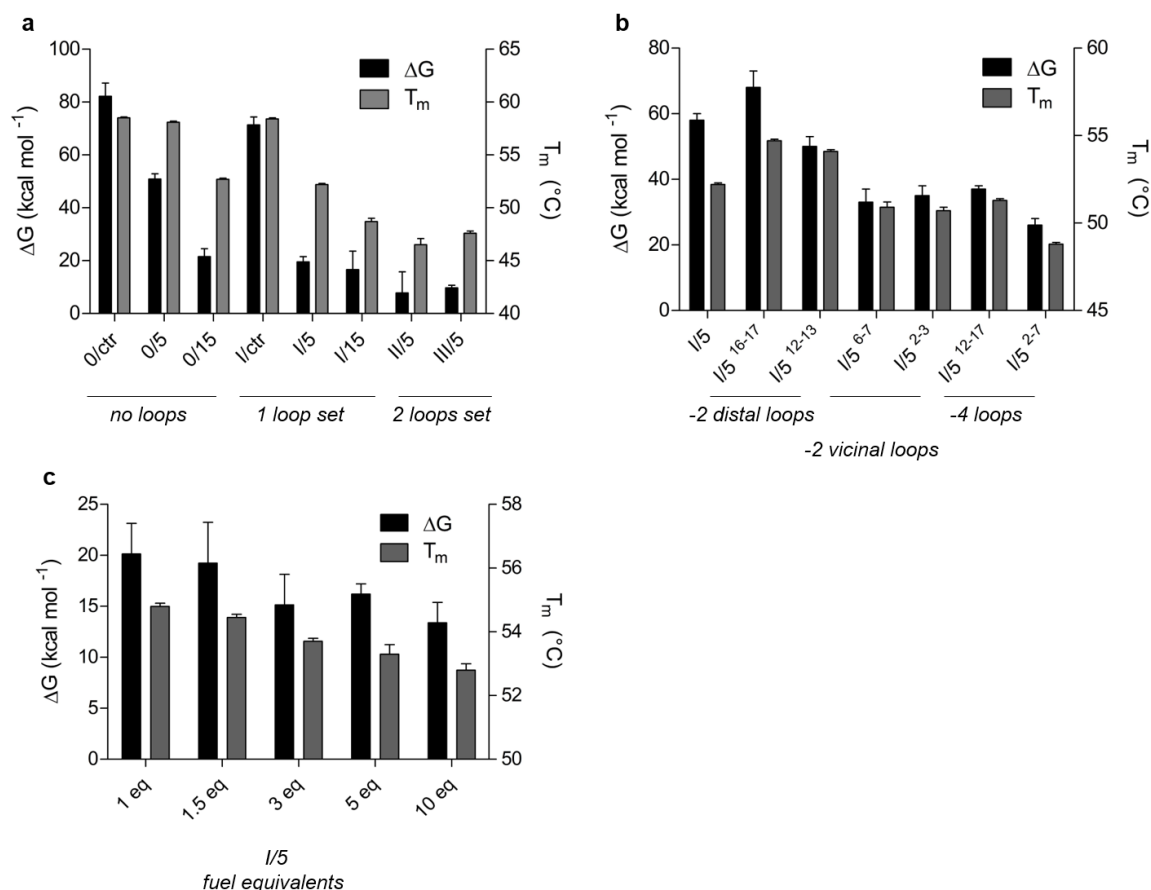


Figure 3-12: Data collection of the free energy change (ΔG , grey bars) and melting temperature (T_m , black bars) attributed to the cooling process of the compact hairpin (**a,b**) and the duplex (**c**). Shown are the mean values + SEM. The obtained values demonstrate that the thermal stability is affected by a change in the surrounding microenvironment, i.e. by the degree of direct or indirect tethering to the origami scaffold (**a**) and by the number and position of lacking hairpin loops (**b**). (**c**) Free energy changes for construct 1/5 in its duplex state and in presence of different equimolar amounts of fuel strand (from 0.25 mM to 2.5 mM). With increasing the fuel concentration, the free energy change as well as the melting temperature decreases, indicating that the enhanced thermal stability of the duplex system is not referred to a local crowding effect of fuel strands in near proximity of the duplexes. However, the general result obtained during the analysis of the thermal stability for both the closed (hairpin) and the open (duplex) constructs is: the higher the degree of immobilization, the higher their thermal stability.

The complete data set of all obtained values is listed in table 3-1 for the cooling and table 3-2 for the melting process.

Table 3-1: Thermodynamic parameters obtained from temperature-dependent FRET experiments for the cooling process. Only samples giving reversible and cooperative thermal transitions were treated by the van't Hoff analysis, allowing to extract the values (mean \pm SEM) of melting temperature (T_m) enthalpy (ΔH), entropy (ΔS) and free energy (ΔG) change at 25°C. The number of hairpin motifs inserted within the seam of the origami structure is also indicated (n°).

		COOLING									
n°		<i>closed device</i>				<i>open device</i>					
		T_m	ΔG	ΔH	ΔS	T_m	ΔG	ΔH	ΔS		
17	I/5	52.2 (± 0.1)	19.5	-58 (± 2)	-0.26 (± 0.01)	52.0 (± 0.2)	23.5	-66 (± 8)	-0.30 (± 0.04)		
17	I/9	58.8 (± 0.1)	--	--	--	58.6 (± 0.1)	--	--	--		
17	I/15	48.7 (± 0.3)	16.6	-52 (± 7)	-0.23 (± 0.04)	49.0 (± 0.3)	17.6	-51 (± 10)	-0.23 (± 0.04)		
17	I/18	--	--	--	--	--	--	--	--		
18	I/CTR	58.4 (± 0.03)	71.4	-182 (± 3)	-0.85 (± 0.02)	58.1 (± 0.1)	75.3	-193 (± 6)	-0.90 (± 0.02)		
13	I/5 ^{-2,3,6,7}	48.8 (± 0.1)	9.8	-26 (± 2)	-0.12 (± 0.01)	50.5 (± 0.1)	10.8	-28.0 (± 0.4)	-0.13 (± 0.01)		
14	0/ctr ^{-2,3,6,7}	58.4 (± 0.1)	75.3	-193 (± 19)	-0.9 (± 0.1)	58.4 (± 0.1)	57.7	-151 (± 6)	-0.70 (± 0.03)		
13	I/5 ^{-12,13,16,17}	51.3 (± 0.1)	13.7	-37 (± 1)	-0.17 (± 0.01)	52.2 (± 0.1)	14.7	-39 (± 2)	-0.18 (± 0.01)		
14	0/ctr ^{-12,13,16,17}	58.3 (± 0.1)	42.2	-166.5 (± 0.4)	-0.70 (± 0.10)	58.4 (± 0.1)	56.7	-149 (± 6)	-0.69 (± 0.03)		
15	I/5 ^{-2,3}	50.7 (± 0.2)	12.7	-35 (± 3)	-0.16 (± 0.01)	51.5 (± 0.3)	19.5	-55 (± 6)	-0.25 (± 0.03)		
15	I/5 ^{-6,7}	50.9 (± 0.3)	11.7	-33 (± 4)	-0.15 (± 0.02)	51.1 (± 0.5)	13.7	-40 (± 1)	-0.18 (± 0.01)		
15	I/5 ^{-12,13}	54.1 (± 0.1)	18.6	-50 (± 3)	-0.23 (± 0.01)	54.3 (± 0.1)	25.4	-67 (± 4)	-0.31 (± 0.02)		
15	I/5 ^{-16,17}	54.7 (± 0.1)	24.4	-68 (± 5)	-0.31 (± 0.02)	54.5 (± 0.1)	27.4	-74 (± 1)	-0.34 (± 0.01)		
0	0/5	58.1 (± 0.1)	50.9	-128 (± 2)	-0.60 (± 0.01)	--	--	--	--		
0	0/15	52.7 (± 0.1)	21.5	-62 (± 3)	-0.28 (± 0.01)	--	--	--	--		
0	0/ctr	58.5 (± 0.1)	82.2	-207 (± 5)	-0.97 (± 0.02)	--	--	--	--		
34	II/5	46.5 (± 0.6)	7.8	-28 (± 8)	-0.12 (± 0.03)	--	--	--	--		
34	III/5	47.6 (± 0.2)	9.7	-32 (± 1)	-0.14 (± 0.01)	--	--	--	--		

Table 3-2: Thermodynamic parameters obtained from temperature-dependent FRET experiments for the melting process. Only samples giving reversible and cooperative thermal transitions were treated by the van't Hoff analysis, allowing to extract the values (mean \pm SEM) of melting temperature (T_m) enthalpy (ΔH), entropy (ΔS) and free energy (ΔG) change at 25°C. The number of hairpin motifs inserted within the seam of the origami structure is also indicated (n°).

		MELTING									
n°		closed device				open device					
		T_m	ΔG	ΔH	ΔS	T_m	ΔG	ΔH	ΔS		
17	I/5	52.9 (± 0.1)	-21.5	65 (± 2)	0.29 (± 0.01)	52.9 (± 0.1)	-25.4	70 (± 3)	0.32 (± 0.02)		
17	I/9	59.5 (± 0.1)		--	--	59.6 (± 0.1)	--	--	--		
17	I/15	48.4 (± 0.1)	-15.6	50 (± 7)	0.22 (± 0.03)	49.2 (± 0.2)	-14.6	48 (± 2)	0.21 (± 0.01)		
17	I/18	--		--	--	--	--	--	--		
18	I/CTR	59.5 (± 0.1)	-	267 (± 6)	1.25 (± 0.03)	59.4 (± 0.1)	-	262 (± 2)	1.23 (± 0.01)		
13	I/5 ^{-2,3,6,7}	49.7 (± 0.1)	-10.2	28.6 (± 0.3)	0.13 (± 0.01)	51 (± 0.3)	-11.7	30 (± 2)	0.14 (± 0.01)		
14	0/ctr ^{-2,3,6,7}	59.6 (± 0.1)	-78.3	193 (± 11)	-0.91 (± 0.1)	59.8 (± 0.1)	-95.0	233 (± 2)	1.10 (± 0.01)		
13	I/5 ^{-12,13,16,17}	52.2 (± 0.1)	-17.6	48 (± 2)	0.22 (± 0.10)	52.2 (± 0.2)	-17.6	54 (± 11)	0.24 (± 0.05)		
14	0/ctr ^{-12,13,16,17}	59.6 (± 0.1)	-71.5	176 (± 2)	0.83 (± 0.01)	59.7 (± 0.1)	-93.0	229 (± 3)	1.08 (± 0.03)		
15	I/5 ^{-2,3}	52.7 (± 0.08)	-22.4	67 (± 1)	0.30 (± 0.01)	52.3 (± 0.4)	-19.5	55 (± 12)	0.25 (± 0.05)		
15	I/5 ^{-6,7}	52.0 (± 0.2)	-12.7	41 (± 2)	0.18 (± 0.01)	51.7 (± 0.5)	-11.7	36 (± 5)	0.16 (± 0.03)		
15	I/5 ^{-12,13}	55.2 (± 0.03)	-26.4	69 (± 1)	0.32 (± 0.01)	54.8 (± 0.2)	-28.4	76 (± 6)	0.35 (± 0.03)		
15	I/5 ^{-16,17}	55.9 (± 0.08)	-29.3	84 (± 8)	0.38 (± 0.04)	56.1 (± 0.10)	-22.5	64 (± 4)	0.29 (± 0.02)		
0	0/5	60.0 (± 0.1)	-50.9	125 (± 8)	0.59 (± 0.04)	--	--	--	--		
0	0/15	53.6 (± 0.1)	-18.6	53 (± 1)	0.24 (± 0.01)	--	--	--	--		
0	0/ctr	59.6 (± 0.1)	-99.8	249 (± 3)	1.17 (± 0.02)	--	--	--	--		
34	II/5	47.6 (± 0.5)	-8.8	30 (± 10)	0.13 (± 0.05)	--	--	--	--		
34	III/5	49.0 (± 0.2)	-11.7	39 (± 1)	0.17 (± 0.01)	--	--	--	--		

3.2.3 Considering the tethered hairpin motifs as elastic springs

The analysis of the thermal stability of the systems evaluated during this study demonstrated that the higher the degree of hairpins immobilization, the higher was their thermal stability (section 3.2.2). Within this and the following section (3.2.4) this effect was analyzed and quantified.

The spring model is one of the most fundamental models in sciences and has been used to idealize mechanical and non-mechanical processes. It allows to predict the response of a system after application of a defined action on it, which moves it away from its initial equilibrium state. This action can be regarded as an applied mechanical force, which acts along a certain distance (Δx). The system responds with a counter-acting force, which tends to re-establish the initial equilibrium condition and is proportional to the displacement and to a constant k , the so-called spring constant, which represents the stiffness or rigidity of the system. In this study, the opening of the hairpin motifs tethered to the origami structure into single stranded forms may be viewed as a displacement of the system from an initial equilibrium condition to a higher energy state. According to this, the hairpin motif was idealized as a spring (eq. [3-1], Hooke's law):

$$F = -k * x$$

Eq. [3-1]

Considering the displacement Δx and the force F as vectors, the minus sign indicates that the direction of the restoring force is opposite to the applied force that generates the displacement [116].

3.2.3.1 Construct I – set of springs in parallel

In case of construct I, different amounts of identical hairpin motifs were aligned in parallel, tethered to the central seam of the origami device. Applying the spring model stated above, the unfolding process of each hairpin loop can be estimated as an unfolding of a spring with an elastic constant k . Considering two springs tethered in parallel ((a), figure 3-13) and performing the same transition Δx , the total force (F_{par}) can be calculated from each single spring element (k_1 and k_2 , eq. [3-2] - eq. [3-4]):

$$\Delta x_1 = \Delta x_2 = \Delta x$$

Eq. [3-2]

$$F_{par} = (k_1 * \Delta x_1) + (k_2 * \Delta x_2) = (k_1 + k_2) * \Delta x$$

Eq. [3-3]

$$k_{par} = k_1 + k_2$$

Eq. [3-4]

As a consequence, the total action of n springs in parallel can be estimated as equivalent to the action produced by one element with an additive spring constant (eq. [3-5]-eq. [3-6]):

$$F_{par} = \sum_{i=1}^n F_i = \sum_{i=1}^n (k_i * \Delta x) = \left(\sum_{i=1}^n k_i \right) * \Delta x = k_{par} * \Delta x$$

Eq. [3-5]

$$k_{par} = \sum_{i=1}^n k_i$$

Eq. [3-6]

In the presented construct I, identical spring-like elements were tethered to the origami frame, thus simplifying the equation (eq. [3-7] - eq. [3-8]):

$$k_1 = k_2 = \dots = k_i = k$$

Eq. [3-7]

$$k_{par} = n * k$$

Eq. [3-8]

3.2.3.2 Construct II & III – two sets of springs in parallel

Considering the case of two springs in series, these may display either identical or different spring constants, here k_1 and k_2 and therefore be associated to identical **(b)** or different hairpins **(c)**, figure 3-13. In this case, the applied force F will result in two defined translational dislocations, Δx_1 for hairpin one and Δx_2 for hairpin two. As the force experienced by each spring is the same, the following equation is valid to describe the system (eq. [3-9] - eq. [3-10]):

$$\Delta x_{Tot} = \Delta x_1 + \Delta x_2 \quad \text{Eq. [3-9]}$$

$$F_{ser} = k_1 * \Delta x_1 = k_2 * \Delta x_2 = k_{ser} * \Delta x_{tot} \quad \text{Eq. [3-10]}$$

Substituting eq. [3-9] into eq. [3-10] the effective spring constant will be related to the individual constants of each single element according to eq. [3-11]:

$$\frac{1}{k_{ser}} = \frac{1}{k_1} + \frac{1}{k_2} \quad \text{Eq. [3-11]}$$

This will allow to describe the global spring constant of construct III **(c)**, containing n different pairs of springs in parallel (eq. [3-12]):

$$\frac{1}{k_{tot}} = \frac{1}{n} * \left(\frac{1}{k_1} + \frac{1}{k_2} \right) \quad \text{Eq. [3-12]}$$

In case of two sets of identical springs (construct II **(b)**), each with a spring constant k , the relation simplifies as in (eq. [3-13]):

$$k_{tot} = \frac{n}{2} * k$$

Eq. [3-13]

The spring model applied to all systems described in this study (3.2.3.1 and 3.2.3.2) is schematically summarized in figure 3-13.

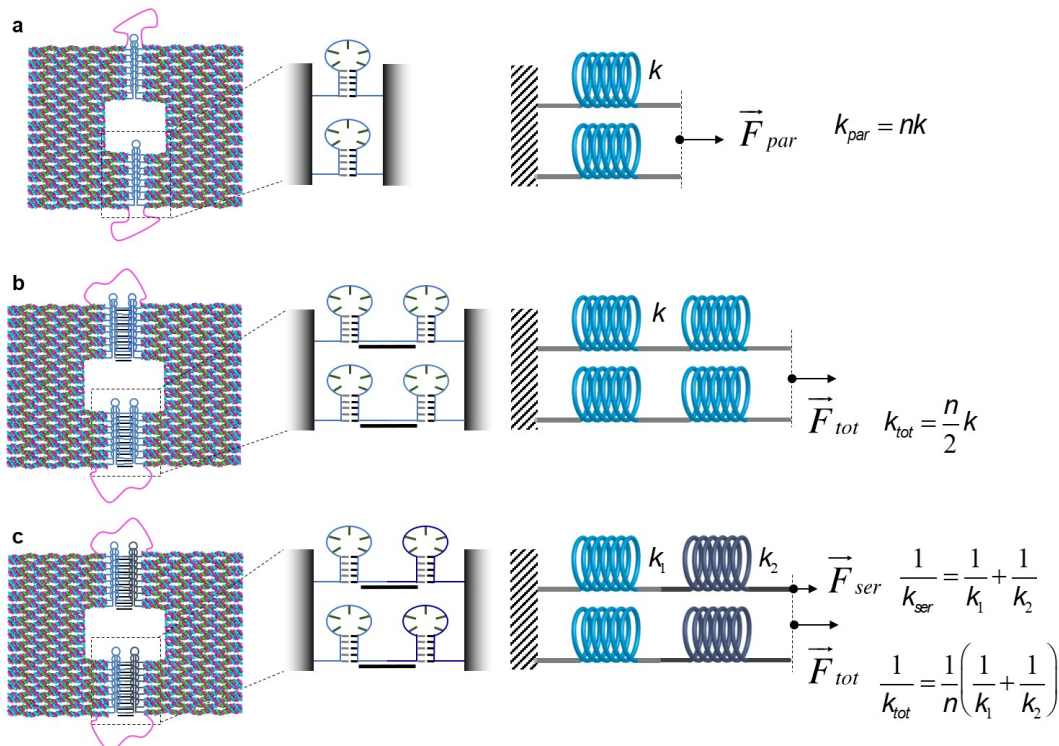


Figure 3-13: Representation of the spring model estimation for the constructs obtaining one, two identical or two different hairpin motifs in series tethered to the origami frame ((a) I, (b) II and (c) III). (a) Considering each hairpin as a spring element, the physical properties of the here schematic visualized two spring system in parallel can be calculated as a single spring with an additive spring constant, having in mind that the elements are identical. (b) Construct II features two identical hairpin in series, halving the total spring constant compared to construct I. (c) The spring model for two different loops in series allows to calculate the characteristics for the ensemble of springs.

3.2.4 Tethering effect according to a nearest-neighbor/WLC model

Upon close observation of the energy values of the transformation of the compact closed hairpin states in various geometric arrangements, it could be shown that tethering a critical number of hairpin loops to a DNA origami scaffold leads to an enhanced

thermal stability of the hairpin motif under investigation. This chapter will attempt to rationalize this effect in quantitative terms.

At this purpose, an innovative hybrid spring model was developed, which, besides the thermodynamic base-pairing contributions, described by the nearest neighbor model (NN), adds a statistical contribution from the worm-like chain (WLC) approximation.

Figure 3-14 schematically illustrates the newly developed energy landscape of the organized collection of hairpin motifs tethered to the described DNA origami platform. The conformational transition between the compact closed hairpin state and the more stable double helical open state is driven by fuel addition (orange). The change in free energy between the closed and open state (ΔG_{trans}) can be described by means of the formation of a base-pairing bond upon hybridization of the fuel strand to the hairpin motif. Keeping in mind that the energy state is path independent, the transformation from one to the other state can be described as the sum of two variables, namely the unfolding of the stem region (ΔG_{unfold}), gaining a higher energy state, and consequentially the hybridization (ΔG_{hybr}) with the fuel complement resulting in a thermodynamically more stable duplex.

For a hairpin motif freely diffusing in solution, i.e. not affected by scaffolding into a precise nanoarchitecture, the energetic pathway for the unfolding and refolding process can be described by the NN model [117;118]. This would result in a total free energy change of unfolding solely based on the base pairing disruption of the single stranded hairpin motif in the used experimental conditions. This leads to a value of 6.8 kcal/mol (Mfold software tool; calculated for T₃C₅T₅G₅T₃ in 4 mM sodium, 10.5 mM magnesium and 25°C; figure 3-15). When comparing this value to the data obtained in section 3.2.2, it emerges that the NN model is not sufficient to describe the energetic transformation of the hairpin loops when tethered to a common origami scaffold and that another energetic contribution is necessary to account for the observed effect. Anchoring both extremities of the hairpin motif to a DNA nanostructure (see section 3.2.1), has led to divergent thermal motions profiles and mechanical forces when compared to the single motor units freely moving in solution. Basically, the spatial configurations accessible to the motor units are reduced and this results in altered energetic profiles. In previous studies, the WLC model has often been used in combination with the nearest-neighbor (NN) model to describe the unzipping (i.e. the mechanical unfolding) of DNA hairpin motifs [117;119]. The principle is based on idealization of the DNA motif as an entropic spring, whose extension is counteracted by a loss of

conformational entropy. Therefore, it can be assumed that the “immobilization” of such motor units within a rigid DNA origami frame would lead to a comparable circumstance. In conventional single molecule experiments, using for example optical tweezers as reported by Bell and coworkers [120], the WLC approximation was used to describe the end-to-end distance of single molecules during mechanical unfolding [121-123]. In the present study, the small reconfigurable motifs are scaffolded to a DNA origami device instead of a solid support like a polystyrene bead or an AFM tip. Nevertheless, the mechanical forces applied for the unzipping of the motifs upon fuel addition can be reasonably described using the WLC model to account for the entropic spring effect, as schematically shown in figure 3-14. Thus, ΔG_{teth} is the total unfolding energy change between the compact closed and the extended single stranded hairpin motif and consists of the thermodynamic base-pairing term ΔG_{unfold} (estimated by the NN model) and an additional entropic energy term derived from the scaffolding effect (ΔG_{spring}) and approximated by the WLC model. As already stated in section 3.2.3, the total ensemble of n scaffolded hairpin motifs, each characterized by a defined spring constant k , can be evaluated by an additive spring constant $k_{\text{tot}} = nk$ (figure 3-13). The transition along the helical axes, i.e. the opening of the motifs/device, requires a force which counteracts the tethering of all hairpin motifs along the seam of the structure, holding it together. This force is proportional to the number of springs integrated within the structure and to their elongation. Thus, the higher the degree of scaffolding the higher is the contribution estimated by the WLC model and therefore the total global energy change necessary to actuate the device. Combining the WLC model with the thermodynamic base-pairing term (NN model), it was possible to calculate energetic contribution of a hairpin motif embedded in the DNA nanoarchitecture and to predict the effect of a distinct number of hairpin features tethered in parallel. Finally, hybridization of the single-stranded extended loop (ΔG_{hybr}) to the complementary fuel strand was described by the NN parameters and compared with the values obtained for the open structure. In this case, indeed no significant change in the end-to-end distance is expected and therefore any elastic contribution to the energy change can be neglected (3.2.2). In conclusion, the NN/WLC approximation, presented in figure 3-14, allowed to calculate the total free energy change of the hairpin-to-duplex transition for a collection of embedded hairpin loops ($\Delta G_{\text{trans}} = \Delta G_{\text{hybr}} - \Delta G_{\text{teth}}$), combining the elastic properties of DNA unzipping with the thermodynamics of duplex disruption. This represents a tool to investigate the stability and mechanical performance of prearranged molecular motifs,

based on their number and spatial arrangement in combination with the spring model presented in section 3.2.3.

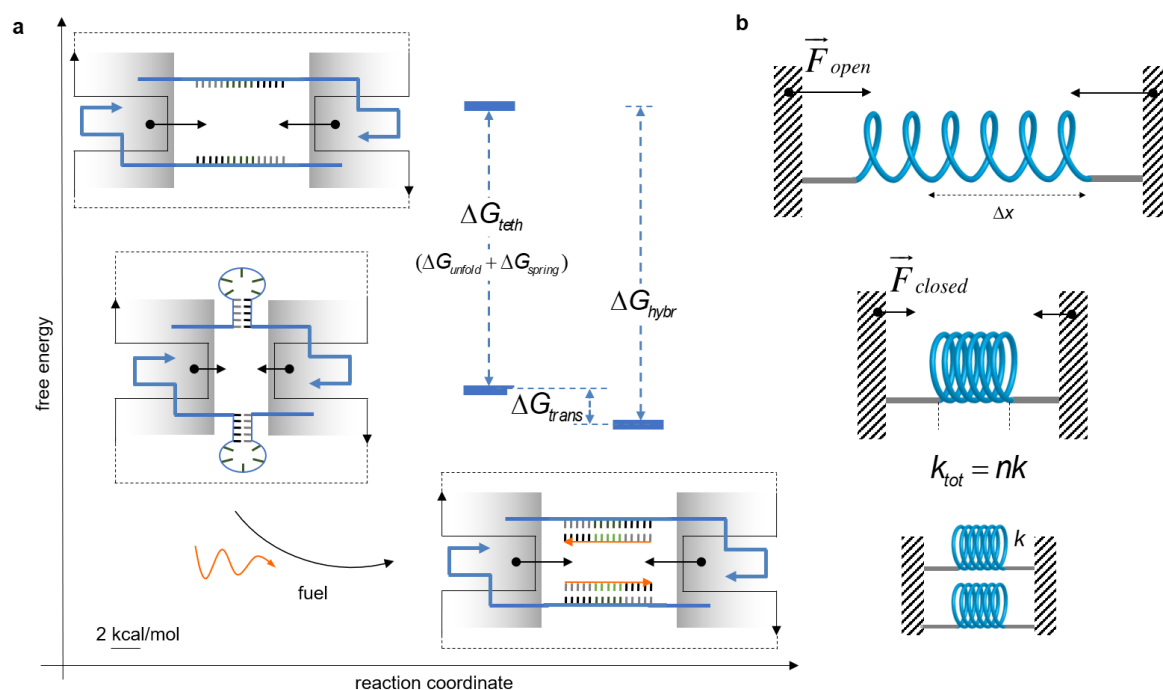


Figure 3-14: Proposed free energy landscape of the organized collection of hairpin motifs tethered to the DNA nanoarchitecture according to a hybrid nearest neighbour/worm-like chain model. (a) The hairpins were embedded in parallel along the seam, anchored at both ends to the two halves of the structure. This scaffolding in combination with the circular scaffold path create a force (F) which counteracts the unfolding of the closed hairpin to the extended single form, resulting in an increased energy between the both states (ΔG_{teth}). The elastic contribution can be described by the WLC approximation (ΔG_{spring}), whereas the base-pairing energy term is calculated by the NN model (ΔG_{unfold}). Adding the complementary fuel strand leads to hybridization of the unfolded single-stranded loop to a more stable duplex, which energetic parameters can be estimated by the NN model (ΔG_{hybr}). This allows to calculate the global transition free energy change (ΔG_{trans}) of the closed and open state of the device. (b) The elastic energy contribution can be estimated by regarding the switchable motors as a small spring with a spring constant k (described in detail in 3.2.3). The energetic levels are in scale (scale bar 2 kcal/mol).

To strengthen the idea of the proposed model, figure 3-15 illustrates the energetic diagram for a free hairpin in solution (all energy values are provided as free energy changes and were calculated using the Mfold software/ DNAmelt, according to the NN approximation, within the theoretical errors introduced by uncorrected salt conditions). The results show that such a path description is unsuitable to describe both the unfolding energy and the hairpin-to-duplex transition of a tethered hairpin, as in the presented DNA origami system.

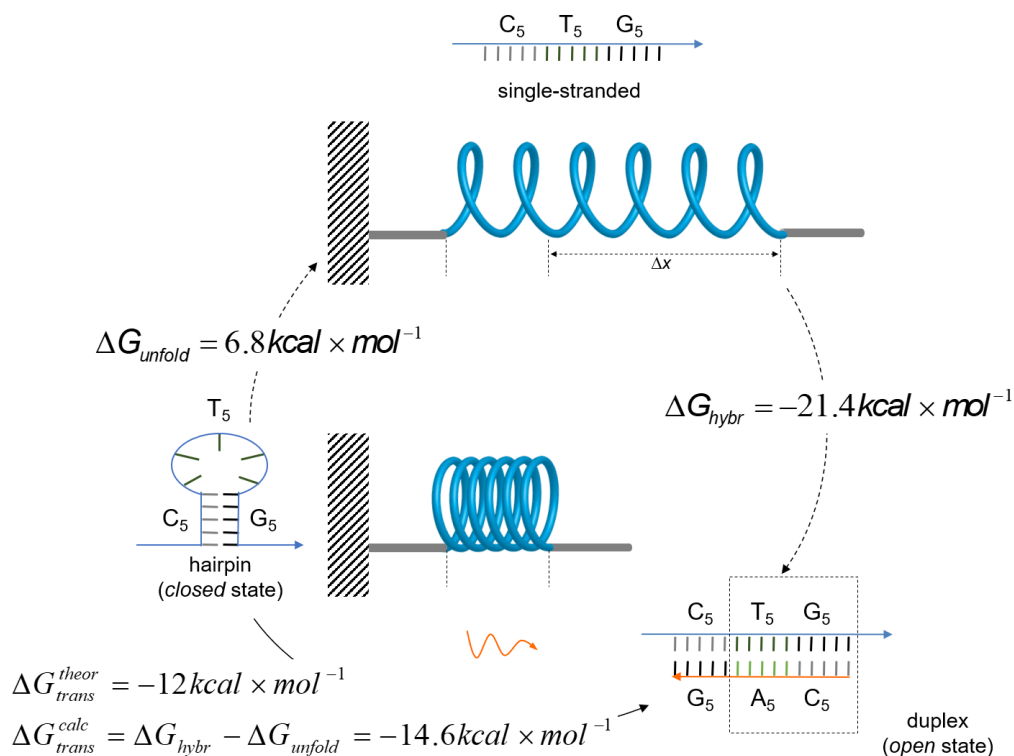


Figure 3-15: NN model approximation of the transition of a single hairpin motif ($T_3C_5T_5G_5T_3$) in its closed state to its open state (additional formation of 10 bp: T_5G_5/C_5A_5), upon hybridization with a complementary fuel strand (orange), obtained with the *mfold* software tool corrected, when possible, for salt concentrations (50 nM strand concentration at 25°C, 4 mM sodium and 10.5 mM magnesium) [117;118;124]. The hybridization energy of the double helical segment was predicted by the *DINAMelt* package ($\Delta G_{trans} = -14.6 \text{ kcal/mol}$ for hybridization between two different strands). Assuming that the transition is a process consisting out of two terms: the unfolding of the single stranded hairpin and the further hybridization to the complementary fuel strand, the energies predicted by the *DINAMelt* software are, respectively, $\Delta G_{unfold} = 6.8 \text{ kcal mol}^{-1}$ (two-state melting) and $\Delta G_{hybr} = -21.4 \text{ kcal mol}^{-1}$ (hybridization between two different strands). The resulting calculated transition energy would be therefore $-12 \text{ kcal mol}^{-1}$, which agrees with the expected theoretical value ($-14.6 \text{ kcal mol}^{-1}$). This indicates that the simplified scenario described can be used to describe the structural reconfiguration of the small hairpin motif used in this work.

From this discrepancy, the need for a modified NN model emerges. As described above, a combined NN/WLC model is proposed that takes into consideration not only the canonical base-pairing interactions, but also the elastic component derived from the restricted conformational entropy of the tethered DNA motifs. However, the free energy change of the transition according to the nearest-neighbor approximation is in almost perfect agreement with the theoretical data obtained by considering the hybridization – unfolding contribution, thus validating the proposed energetic path for analysis

of tethered hairpins. In the following, this hybrid model is used to quantify the tethering effect observed.

The persistence length (L_p) of a polymer is the mechanical property that describes its stiffness. Intuitively, L_p is the length below which the polymer can be considered as a “rigid rod”. Polymers with high L_p are more rigid than polymers with a low L_p . The persistence length of a polymer has been described in statistical terms using different models, as for example the worm-like chain (WLC) model also used in this study. It can be assumed that the end-to-end distance of the single stranded closed hairpin (R_{cl}) is equal the diameter of a DNA double helix (2 nm) and that its extension to a duplex form leads to an end-to-end distance (R_{op}) of about 5.1 nm (dependent on the formation of a 15 bp duplex with a helical rise of 0.34 nm/bp). This results in a total displacement of about 3 nm (R). Using a persistence length (L_p) of single-stranded DNA of 1.5 nm and a helical rise of 0.65 nm/base [119;121], the entropic force experienced at the ends of the hairpin spring in both the closed ($F_{spring,cl}$) and extended ($F_{spring,op}$) form can be calculated with eq. [3-14]:

$$F_{spring} \approx \frac{k_B T}{L_p} \left(\frac{1}{4 \left(1 - \frac{R}{L_c}\right)^2} - \frac{1}{4} + \frac{R}{L_c} \right)$$

Eq. [3-14]

with:

$k_B T$: constant, Boltzman factor at 25 °C, 4.1 pN nm

L_c : contour length of the 21 base-long hairpin motif =13.6 nm

The total force experienced at the end of the single hairpin tethered to the origami structure is 0.8 pN in the closed state and 1.7 pN in its open single stranded form. Note that, using the same equation, the entropic force contribution generated by the unpaired segment at the top (140 bases) and bottom extremity (141 bases) of the m13mp18 scaffold of the structure is negligible (0.09 pN and 0.089 pN in the closed form). By summing up the contributions of 17 identical hairpin motifs aligned in parallel along the central seam, the global entropic force is 11.3 pN for the closed and 25.1 pN for the open single stranded form (3.2.3.1).

The free energy stored in this entropic spring [105] in both states can be calculated by integrating the force (eq. [3-14]) from 0 to R (with $R = R_{cl}$ or R_{op}), as described in eq. [3-15].

$$E_{spring} = \int_0^R F_{spring}(R)d(R) = \frac{k_B T L_c}{4L_p} \left(\frac{3\left(\frac{R}{L_c}\right)^2 - 2\left(\frac{R}{L_c}\right)^3}{\left(1 - \frac{R}{L_c}\right)} \right)$$

Eq. [3-15]

Substituting with the parameters of our system, this results in a difference in entropic conformational energy between the open and the closed configuration of a single hairpin motif ($\Delta G_{spring} = E_{spring,op} - E_{spring,cl}$) of 0.7 kcal/mol. The total energy for 17 hairpins in parallel will be therefore 12.4 kcal/mol (ΔG_{spring}). This can be attributed to the unfolding of 17 hairpin motifs tethered to construct I/5. Adding the thermodynamic NN term from the base-pairing disruption ($\Delta G_{unfold} = 6.8$ kcal/mol) one obtains a theoretical value of 19.2 kcal/mol for 17 hairpins embedded within the reconfigurable region of the origami structure ($\Delta G_{teth} = \Delta G_{spring} + \Delta G_{unfold}$), which is in perfect agreement with the experimental values observed during this thesis for construct I/15 (19.5 kcal/mol), and reasonably support the validity of the applied model. This value of energy corresponds to the maximal thermal stability observed during this study, i.e. for full tethering of the FRET labeled hairpin in the most stable region of the nano-device. Variations in the scaffold environment and geometric arrangement led to deviation till about 13% from the predicted values estimated by our model, which is still acceptable. By decreasing the degree of scaffolding, i.e. reducing the amount of integrated molecular motors as well as the structural rigidity of the microenvironment, compromises the application of the WLC contribution because of a less defined end-to-end distance in the initial and final state of the hairpin. For example, one individual hairpin tethered to the nanostructure does not show an increased thermal stability when compared to a hairpin free in solution. A critical number of neighboring hairpins are necessary to reach sufficient rigidity and therefore for the scaffolding effect to become evident. Close observation of the data of construct I/5²⁻⁷, where the labeled region lacks the four hairpin motifs in near proximity, two below and two above the anchoring points, results in a free energy change of unfolding of about 9.8 kcal/mol, which is only slightly higher than the calculated value for a free hairpin motif in solution (6.8 kcal/mol). In construct I/5^{2,3} and I/5^{6,7} the number

of adjacent loops were increased coming along with a remarkable increase in thermal stability (12.7 kcal/mol, 11.7 kcal/mol respectively). Here only 2 neighboring loops were left out within the reconfigurable region of the structure, either above or below the labeled hairpin, leading to a total amount of 15 loops embedded. In construct I/5^{12,13} even a higher value of free energy change has been found (18.6 kcal/mol). Here the loops on the other side of the structure were omitted, that is, in a region rather distant to the analyzed hairpin. The higher thermal stability observed is in agreement with the idea that the energy change is dependent on the structural surrounding microenvironment and that this effect is more evident when nearby the labeled motif.

Additionally, to estimate the contribution given by scaffolding, a bulk solution experiment was performed on a freely diffusing hairpin using the same amount of motors tethered to our DNA origami structure. No detectable signal was observed (figure 3-16). This demonstrated that a “scaffolding” effect indeed occurs and that a simple NN thermodynamic model cannot fully explain the phenomenon observed, as the hybridization energies are identical in both cases. Although the value of thermal stability observed for the fully tethered hairpin is about “only” three-fold higher than the expected value for the same motor freely moving in solution, these data show that such a small difference is indeed sufficient for visualization of the process even at nanomolar concentrations.

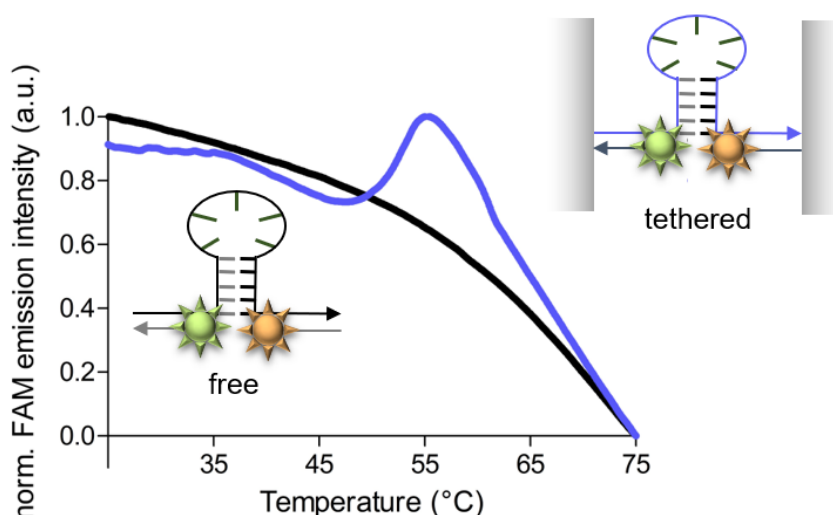


Figure 3-16: Comparison of the normalized FAM emission intensity during the cooling process of the labeled hairpin motif ($C_5T_5G_5$), either free in solution (black curve) or embedded within the origami surface at position 5 of the seam (purple curve, attributed to construct I/5). Visualization of the thermal transition at around 53°C only comes observable by tethering the hairpin motif to sufficient rigid surrounding, indicating the importance of the scaffolding effect, which instead not evident for the same hairpin motif freely moving in solution. Even though the obtained data of the free energy is only about three-fold higher than the theoretical value for the same motif freely in solution, the results indicates that such a small variation is indeed sufficient for visualization of the process even at nanomolar concentrations.

A direct consequence of the structural tethering, is a reduced value of transition energy between the initial single stranded closed hairpin and the final open duplex state. This can be quantified as $\Delta G_{op} - \Delta G_{cl} = \Delta G_{trans}$ (figure 3-14). For construct I/5, being fully tethered, the hairpin-to-duplex transition energy is -3.9 kcal/mol, indicating a three-fold lower value than expected by the NN model, calculate with identical concentration of freely moving motifs in the experimental conditions used (-12 kcal/mol; figure 3-15). Again, this is in perfect agreement with the theoretical expectations and strengthens the validity of the hybrid model to describe the energy landscape of a collection of embedded molecular motors.

3.2.5 Tug-of-war between opposite forces

Applying the hybrid NN/WLC model (3.2.4), it was possible to describe the energy landscape of an ensemble of spring-like motor units tethered to a defined DNA nanostructure and quantify its global dynamical characteristic. The following task relied on the possibility to employ the calculated pulling forces to mechanical unfold a nano-architecture, which was designed to perfectly fit inside the inner cavity of the DNA

origami device (figure 3-17). Based on the results described above, system I/5 was chosen for this purpose, because it showed the maximal degree of structural tethering and consequently led to the highest mechanical forces attainable. Therefore, two 21 bp long protruding arms were placed at the opposite edges of the inner cavity and pointing towards its center. The arms had the following sequences: (TGG)₇ for the left and (TTG)₇ for the right one (grey bold lines, figure 3-17, full list of sequence listed in E Supplementary Information). The inner cavity of the device in its closed state was then filled out with a bimolecular G-quadruplex of sequence (G₄T₄G₄)₂, binding to the protruding arms through elongated complementary sequences (orange: (CCA)₇G₄T₄G₄ and green: (CAA)₇G₄T₄G₄).

The addition of fuels to the embedded hairpin loops within the reconfigurable region of the structure generates a pulling force (white arrows, figure 3-17) opposite to the forces (Hoogsteen hydrogen bonds and stacking interaction), which try to keep in place the G4 architecture trapped inside the inner cavity of the device (black arrows, figure 3-17). As in a tug-of-war competition, the winning component will define the final state of the device (open: for stronger hairpin opening force and closed for stronger G4 intermolecular forces). Depending on the base content and buffer compositions G4-motifs can display different thermal stabilities. For the sequences used in the present work, values between 5 and 10 kcal/mol are normally reported in the literature [125;126]. Therefore, the energy required to open the device (12.4 kcal/mol) should be sufficient to effectively unfold the G4-based architecture placed within its inner cavity, resulting in mechanical rupture of the internalized structure. To prove this assumption, the 5'-end of the left sided protruding arm was labeled with a FAM fluorophore (green symbol, figure 3-17) and 3'-end of the complementary elongated G4 sequence was labeled with a TAMRA fluorophore (orange symbol, figure 3-17). This design will allow to achieve a high FRET efficiency in the closed state of the device, in concomitance with correct formation of the G4-architecture. In a simple experiment at constant temperature the change in FAM emission intensity over the time before and after fuel addition was investigated. As visualized in figure 3-17, the low FAM emission intensity demonstrates correct G4-formation in the closed state of the device (blue curve, figure 3-17). The fluorophore emission increases drastically upon addition of the fuel strands, demonstrating the opening of the structure (red curve, figure 3-17).

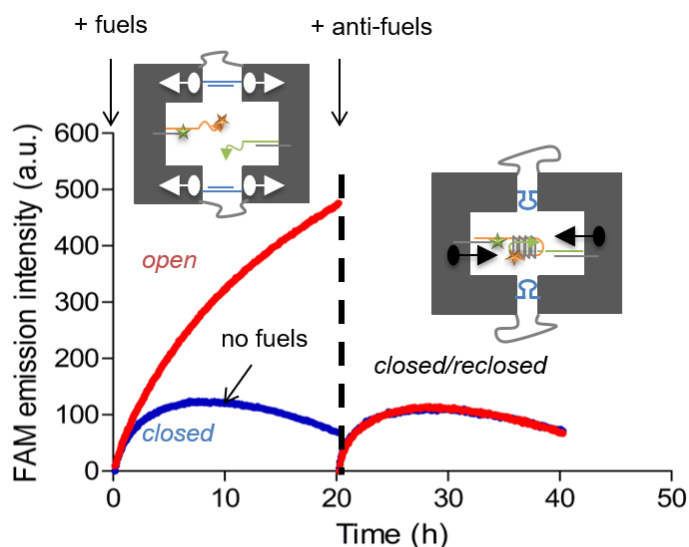


Figure 3-17: Monitored FAM emission intensity during a mechanical unfolding/refolding process of a G4 motif connected into the inner cavity of the reconfigurable I/5 construct. For analyzing this effect time dependent FRET spectroscopy was used. The rupture and correct reformation of the G4 motif was investigated at constant temperature after fuels addition (left-side red curve) and anti-fuels (right-side red curve), compared to a control sample where no fuels were added (blue curves).

This gave evidence that the employed forces upon fuel addition were sufficient enough to unfold the G4 motif within the cavity and thus open the nanodevice. However, this process was rather slow and took more than 20 hrs [44]. Adding the fully complementary antifuel strands led to a rapid drop of the FAM emission signal, revealing fast refolding kinetics and fully reversibility of the process with correct reformation of the G4-architecture in absence of the pulling forces (second red line, figure 3-17). This result demonstrates the significant role of structural scaffolding to fulfill a certain mechanical task, which wouldn't be possible by molecular motors freely diffusing in solution and further supports the validity of the here proposed model to quantify this effect.

All in all, it was possible to show, that an organized tethering of small switchable molecular motors within a DNA nanostructure triggers a translational movement and alters the energy landscape of the motifs. This can be interpreted by a hybrid spring model, which besides the thermodynamically base-pairing term (NN model) adds the elastic contribution estimated by the WLC model. It could be visualized that rigid scaffolding of such motifs, as compared to the same motifs freely moving in solution, enhances their thermal stability and mechanical performance, enabling to mechanical unfold a defined architecture linked inside the inner cavity of the device. Although the intrinsic flexibility of the hairpin motifs represents a disadvantage for the application of such systems as rigid mechanical devices, this idea can be applied to more rigid

nanodevice, whose inner cavity can be programmed to catch other motifs or proteins in a size selected fashion and in a predictable orientation. This work emphasizes the importance of tight fastening, compactness and organized distribution of switchable motifs in the design of DNA nanomechanical devices, where the synchronized and coordinated action of multiple motors can be used to apply higher forces and actuate large-scale transformations otherwise impossible to achieve in a random state.

3.3 Development of a versatile DNA nanochamber for defined protein encapsulation

Nature uses compartmentalization strategies to achieve control over spatial matter distribution in time, i.e. enzyme/substrate interactions, local concentration gradients and/or metabolic channeling [50;83]. All rely on a similar fundamental rule, namely the use of (many) weak non-covalent interactions in a defined geometrical arrangement [68]. Following this basic principle, scientists were able to construct synthetic, supramolecular hosts to stabilize reactive intermediates [4] and to enhance enzymatic catalyzed reactions [5]. These synthetic self-assembled constructs, built up by DNA nanotechnology, can address specific molecules with nanometer precision [6], allowing to construct innovative nanocompartments with programmable size, mechanical properties and loading capability for specific chosen guests [7-11]. Several works showed that DNA-encapsulating hosts alter protein function, probably because of enhanced protein lifetime and/or modulated conformational changes, responsible for improved enzymatic activity [33;86;127;128]. It has been postulated that the high negatively charged DNA layer may exert a chaperon like role, in stabilizing the encapsulated protein [89], although alternative hypotheses have been also advanced. Until now, there is no common explanation for this observed effect, which indeed still needs to be clarified completely. As described above, successful protein encapsulation has been done until now using covalent chemical strategies, which alter permanently the outer surface of the protein of interest, i.e. its natural properties, resulting in a lack of regioselectivity and stoichiometric control of the overall protein modification [53;67;68;129].

At this purpose, a method was developed for the selective trapping of a protein into a defined 2D-DNA frame by means of non-covalent interactions, thus surpassing the limitations of current synthetic methods and taking inspiration from natural recognition strategies. The focus was set on the effect of the DNA "environment" on the chemical properties the encapsulated protein, specifically the thrombin, belonging to the S1 family of the serine proteases. The following properties were analyzed: (i) the binding

affinity of the protein to a specific ligand and (ii) the enzymatic activity of the protein to a specific FRET substrate. Thrombin plays an important role during thromboembolic diseases, hemostasis, metastasis and tumor invasion and therefore embodies an attractive target for antithrombotic therapy. Until now the role of this protein during the coagulation pathway is one of the best described processes *in vivo*. Several studies revealed that the thrombin protein displays two binding sites (exosite I and II), positioned at opposite sides of the protein, which are targeted respectively by the protein fibrinogen (at exosite I) and heparin (exosite II). To date, heparin commonly serves as a drug for inhibition of thrombin, it is however accompanied by several side effects like enhanced risk of hemorrhage and allergenic immune response. At this purpose, DNA aptamers, specifically targeting the two exosites of the thrombin molecule have drawn ever more attention [130]. In literature, two well-defined DNA aptamers (thrombin binding aptamers, TBA1 und TBA2, specification and characteristics listed in E Supplementary Information), have been described, which form a G-quadruplex and specifically bind to the two electropositive exosites on the outer surface of the protein [70;71]. Here, by strategic positioning of these two G4-motifs within the inner cavity of the DNA frame, controlled formation of a 1:1 host-guest complex was achieved, without the need of protein engineering, which may affect the natural properties of the encapsulated protein. Similar to antibodies, it could be already shown that TBAs display a high avidity effect against thrombin after their mutual conjugation with an optimal linker [135] or when they are co-printed on a sensor surface with optimal density [136]. In that way, researches could demonstrate that the affinity against thrombin could be significantly enhanced by 100 to 10,000 fold. In our system, the TBAs are also somehow linked one another through the DNA origami scaffold. In addition, the active site of the protein is placed in its inner domain. The interplay between the active site and the two electropositive exosites governs the temporal sequence of binding events that characterize clot formation *in vivo*. Basically, in this *in vitro* system here, the binding and the active regions, can be independently addressed, allowing to separate the contributions to each of the two functions. In this way, their mutual relationship through postulated allosteric mechanisms can be investigated in a rational way. Both these properties are related to the reactivity of the protein, that in chemical terms refers to the capability of the protein to recognize, bind to and operate on an external molecule. In this sense, thrombin is an interesting candidate for this study because it enables to analyze both the binding and activity aspect in two distinct regions of the tertiary structure.

The main question to address was: “*is the reactivity of the protein affected by the surrounding DNA environment?*” More specifically: “*is the DNA frame acting as a simple linker between the two aptamers or is it also actively affecting the avidity entropy of the two aptamers towards the same protein target?*”. Finally, the study should elucidate how the DNA frame affects the TBA/thrombin binding energy and the allosteric substrate recognition.

Therefore, five distinct designs were developed to encapsulate thrombin using two G-quadruplexes linked at opposite sides of the inner cavity of the DNA frame and featuring different intermolecular distances and distinct degrees of rotational freedom (for detailed information see section 4.2.1.1, figure 4-7).

3.3.1 Successful G-quadruplex formation characterization for cargo loading

Particularly crucial for this study is the correct integration and configuration of the chosen G-quadruplexes when embedded within the inner cavity of the structure in the experimental conditions used. Therefore, a FRET assay combined to gel electrophoresis analysis was performed to evaluate the correct formation of TBA1 and TBA2 (details in section 4.2.2.2 and 4.2.5.1). Figure 3-18 shows the results obtained by non-denaturing PAGE and demonstrates correct assembly of the proposed G4-motifs when free in solution in the experimental conditions used. The FRET samples (lane 1 and 2, containing both labels within the sequence, FAM= green and TAMRA= red) show a high FRET efficiency as almost no FAM signal (green) is visible when compared to the samples containing only the donor fluorophore within the sequence (lane 3 and 4, green fluorescence signal). As expected, addition of the full complementary sequence resulted in hybridization of the aptamer and opening of the G4-configuration with the formation of a duplex, consequently lowering the FRET signal. This was visible in lane 5 (TBA1) and 6 (TBA2) as a fluorescence signal, due to merging of the green (FAM) and red (TAMRA) emission signals.

The same two-color analysis was performed for the G4-motifs integrated within the inner cavity of the various DNA origami designed during this thesis (D0, D1, D2, D3S and D3L; section 4.2.1.1, figure 4-7). These designs differ in the length and rotational freedom of the protruding arms to which the TBAs bind. At this purpose, the two protruding arms and the corresponding complementary aptamers used for design 1 were embedded into the DNA-host in a one-step assembly process. The correct integration

and configuration of the architectures inside the inner cavity of the origami were proven by gel electrophoresis (4.2.5.1, shown in figure 3-19).

The fluorescence bands of the labeled aptamers co-migrate with the origami nano-chambers (compare FAM and TAMRA signals to the ethidium bromide staining image) and the intensities of the FAM/TAMRA bands confirm correct formation of the G-4 architectures within the inner cavity of the nanodevice.

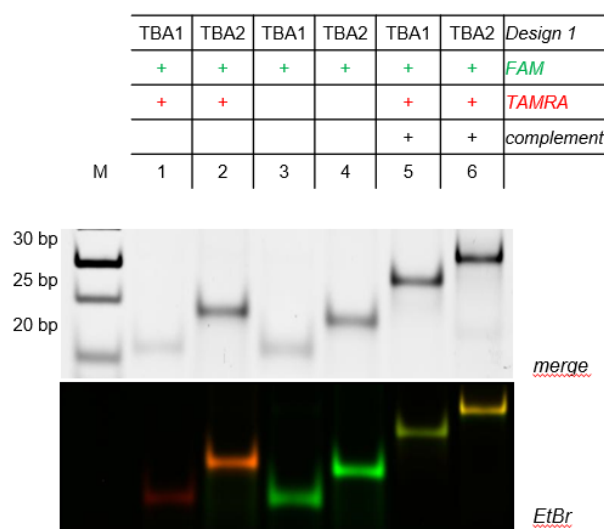


Figure 3-18: 25% non-denaturing PAGE characterization of the correct G-quadruplex formation free in solution, relying on design 1, using FRET analysis. The two motifs were labeled within the aptamer sequence with a FAM (green) and a TAMRA (red) fluorophore to ensure high FRET efficiency in concomitance with G4 formation (detailed on the design described in section 4.2.2.2), visualized in lane 1 and 2 for TBA1, TBA2 respectively. Integrating the only the donor fluorophore in comparison to the FRET samples shows no FRET signal (lane 3 and 4). Adding the fully complementary G4-sequence demonstrated a lower FRET efficiency and a drastic change in electrophoretic mobility (lane 5 and 6). Gel running parameters: 80 V, 2 h at 4°C in 1x TBEMg. Lane M contains a 10 bp ladder.

Also in this case, a change in FRET efficiency is visible for all samples compared to the control samples containing the donor-only label. Lane 1 has a lower FAM intensity as compared to the sample loaded in lane 2. Less evident is the FRET effect from lane 5 to 6 and 7 to 8, corresponding respectively, to formation of TBA2 and both the TBA1 and TBA2. This may be accounted for by a slight difference in the total amount of DNA origami loaded.

Addition of the fuels fully complementary to the integrated and fluorescently labeled G4-arms appended with a short toehold sequence, led to single strand displacement of the embedded aptamers and formation of a duplex in solution with consequent

disappearance of the FAM and TAMRA fluorescence signals in all origami samples (lane 3, 6 and 9).

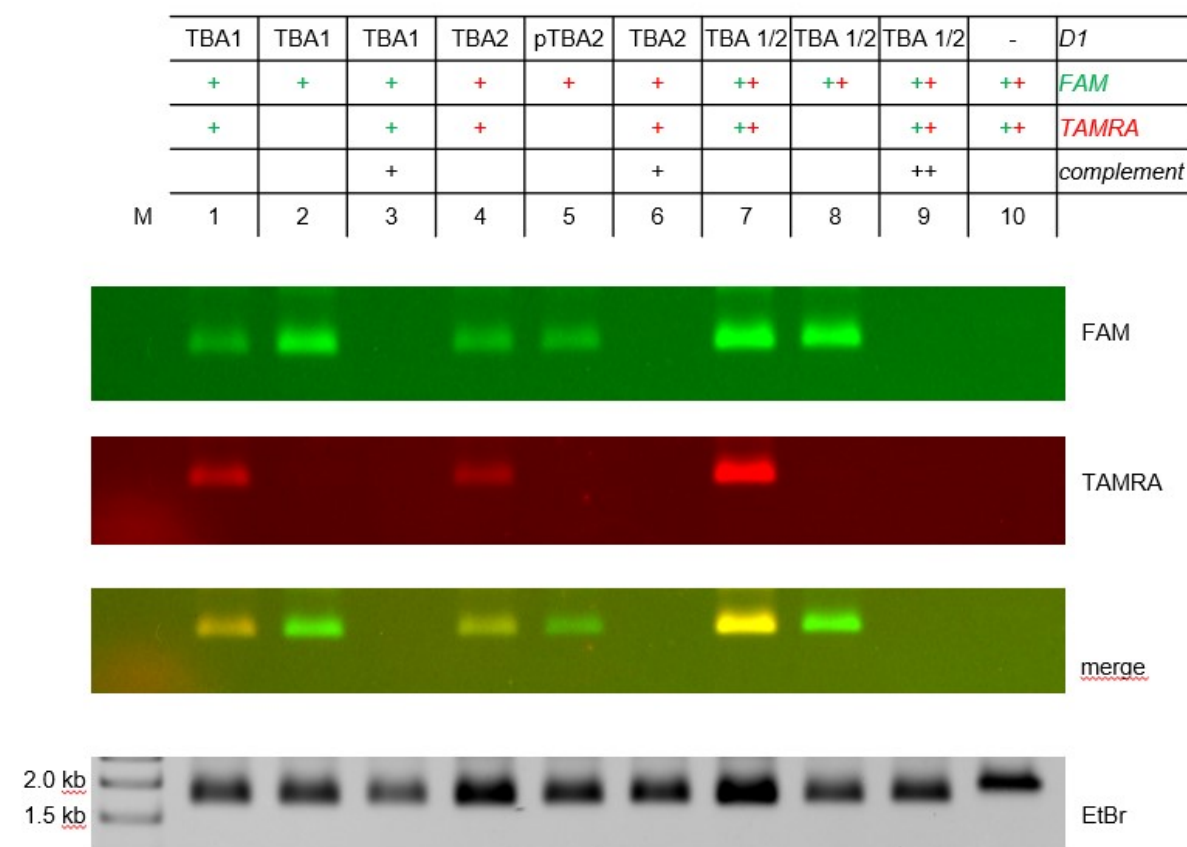


Figure 3-19: Gel electrophoresis characterization of the correct configuration of the embedded G4-motifs within the inner cavity exemplary shown for design 1 (details described in 4.2.1.1). The gel images show efficient integration of the aptamers within the nanostructures, visualized by superimposable migration rates of the fluorescence labeled arms and the origami devices. The high FRET efficiencies visualized in lane 1, 4 and 7 normalized to the total amount of structures analyzed during this experiment (ethidium bromide image) compared to the constructs containing only the donor fluorophore (2,5 and 8), demonstrate correct configuration of the G4-architectures, when embedded within the origami structure and the used experimental conditions. Efficient strand displacement of the short toehold appended aptamers was visualized by adding fully complementary sequences (lane 3, 6, and 9) going along with the disappearance of the fluorophores. Furthermore, the specificity of the G4-motif extended arms to the embedded protruding arms was successfully shown in lane 10. Gel running parameters: 0.75% agarose, 2.5 h, 80 V by 4°C in TBEMg 1x. Lane M contain a 1 kb DNA ladder. This analysis was performed by Bianca Hoofe during her bachelor thesis in the Saccà laboratory.

A control sample, where the protruding arms were omitted during the assembly process shows the specificity of the catching arms: no G4-formation is possible in absence of the protruding arms pointing towards the center of the inner cavity (lane 10).

3.3.2 Thrombin stability

Beside correct formation of the DNA host in high and quantitative yields and the efficient integration and precise folding of the protein ligands (in this case G-quadruplexes), the stability of the protein during the experimental manipulation, analysis and purification procedures is mandatory. Figure 3-20 shows a time-course analysis of the protein stability. Examined was the proteolytic grade and autodigestion of the protein at different timepoints, in TEMg 1x buffer, either at RT or at 37°C. No apparent change in the band intensities and formation of no visible degraded protein byproducts reveals the stability of the protein within the time frame and experimental conditions used.

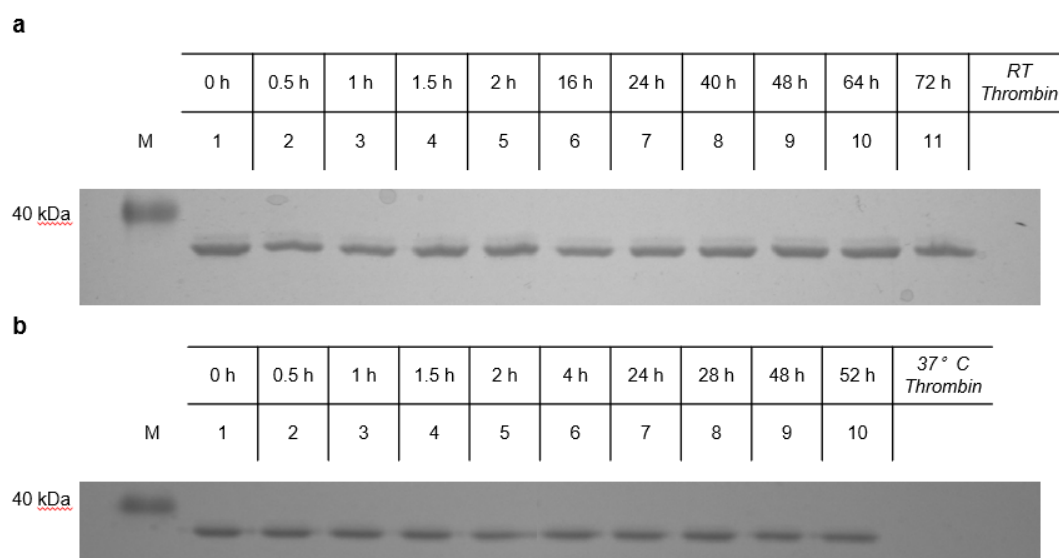


Figure 3-20: Thrombin stability characterization by SDS-PAGE gel electrophoresis at room temperature (a) and 37°C (b). The not apparent shift of band intensities during the evaluated time frame in concomitance with no observable autodigestion of the protein justifies the use of the protein for further investigations at the given conditions. 120 V for 1 h at RT with 15% resolving and 5% stacking gel in 1x SDS running buffer. Lane M contains a low-range protein marker (1.7 to 40 kDa). This analysis was performed by Bianca Hoofe during her bachelor thesis in the Saccà lab.

3.3.3 Binding affinity of a thrombin molecule embedded into DNA origami frame

A frequent approach to enhance the detection sensitivity and specificity of an immunoassay is the use of a multivalent antibody construct that recognizes different epitopes of a target and exhibits a synergistic binding affinity called avidity. In a similar way, multivalent aptamer constructs can be prepared to improve aptamer-based detection assays [131-133]. Because TBA1 and TBA2 can bind to distinct epitopes of the same thrombin molecule, their binding affinity was greatly enhanced by simply coanchoring

a pair of distinct aptamers on a tiny surface such as a microarray spot [134]. Aptamers linked to each other by a longer spacer showed higher binding affinity. However, the length was not the only factor. Indeed, oligonucleotide spacers (like 12dT) had a higher effect than aliphatic chains, probably because the negative charge of the DNA linker bring the aptamers far apart to create room for target-induced folding [134]. Also, the effect of spacer length on TBA1 could be more important than on TBA2. Indeed, TBA1 lacks an additional duplex portion in its structure (which is instead present in TBA2) and thus requires an effective spacer to help in the target-induced folding more than TBA2 needs. Therefore, synergistic effect of DNA spacer and avidity can be systematically investigated by different geometrical designs of the aptamers (D0, D1, D2, D3S and D3L, detailed design in figure 4-7) embedded within the cavity of the DNA frame. Briefly D0, was designed to display shorter and less flexible arms, but a larger inner room compared to D1. This latter had longer, more flexible arms but a smaller room available inside the inner cavity. D2 displayed a higher degree of rotational freedom and flexibility, but less inner space. Finally, in D3 the TBA1 is linked to the complementary strand through a short (T₁₀, D3S) or a long (T₁₆, D3L) spacer, whereas the anchoring of the TBA2 arm is identical to D1. The effect of all these designs on the binding efficiency of thrombin were analyzed by means of AFM imaging (4.2.5.2) and gel electrophoresis mobility assays (4.2.5.1).

AFM analysis allowed to characterize all designs (0, 1, 2, 3S and 3L) and quantify the efficiency of protein loading at the single molecule resolution. Representative AFM images are presented in figure 3-21 and figure 3-23. Figure 3-21 illustrates the AFM results obtained for D0, D1 and D2, bearing either the TBA1 aptamer within the left edge of the cavity (left column) or the TBA2 aptamer integrated at right edge of the cavity (middle column), as well as both aptamers (right column; schematic illustration of the designs are reported in the insets of all images). Design D0 led to a total protein loading efficiency of 15.2% (\pm 9.5), 18.2% (\pm 8.4) for TBA1 and TBA2 ligands, respectively. Protein loading was increased by embedding both G4-motifs within the inner cavity of the structure (45.1% \pm 12.5). The same tendency could be observed for design D1: TBA1 led to a total protein encapsulation of 5.0% (\pm 3.5), TBA2 to 20.4% (\pm 4.5) and both aptamers to 44.1% (\pm 13.6). These results confirm previous observation by Lao *et al.* [134], which state that the binding affinity of TBA2 for the thrombin molecule is larger than that of TBA1. The values described in the literature for the K_D (dissociation constant) of the aptamers are in perfect agreement with the obtained AFM

characterization data (TBA1: 75-100 nM and TBA2: 0.5 nM), explaining the higher loading efficiency observed in samples containing the TBA2-only motif [70;71]. Additionally, the negatively charged origami frame can be regarded as a rigid linker between both motifs, leading to a synergistic encapsulation avidity effect. The charge hereby would support the repulsion between the two anchored G-quadruplexes and therefore assist the conformational folding similarly to the action of an oligo (dT) spacer. Interestingly, there is a difference between the binding yield of TBA1 in D0 (shorter and less flexible arm but larger inner room available) compared to D1 (longer, more flexible arm but smaller room available). This highlights the importance of structural flexibility and room accessibility in the frame of a putative target-induced folding effect.

The values of loading efficiency obtained for D2, featuring the higher degree of rotational freedom and flexibility, but the less inner space, were drastically decreased (TBA1: 9.1% (\pm 3.9), TBA2: 5.1% (\pm 3.4) and TBA1&2: 15% (\pm 7.3) in comparison to D0 and D1. The structural flexibility of the ligands, that is, how they are anchored to the DNA origami surface, and the accessibility room within the inner cavity of the device, strongly affect the binding efficiency of the corresponding protein molecule. However, an avidity effect appears to be present in any case analyzed. By anchoring both aptamers within the inner cavity of the DNA origami frame, the loading capacity increased. To better understand all these issues and possibly unify under a more general perspective, molecular dynamic simulations of design D2 under the used experimental conditions were performed by the Sánchez-García group, by Dr. Kenny Bravo-Rodriguez. The investigations revealed that simultaneous binding of one thrombin unit to both DNA helices in construct D2 is likely difficult to occur, due to the excessive length of the double helices, which bring their termini too near each other. The geometric arrangement inside the cavity will therefore restrict the mobility of the binding motifs and therefore the available space between the two DNA helices to host the protein (figure 3-22).

Indeed, double protein binding events were negligible in all designs (0: 0.29% \pm 0.7, 1: 1.29% \pm 1.0 and 2: 0.63% \pm 0.9).

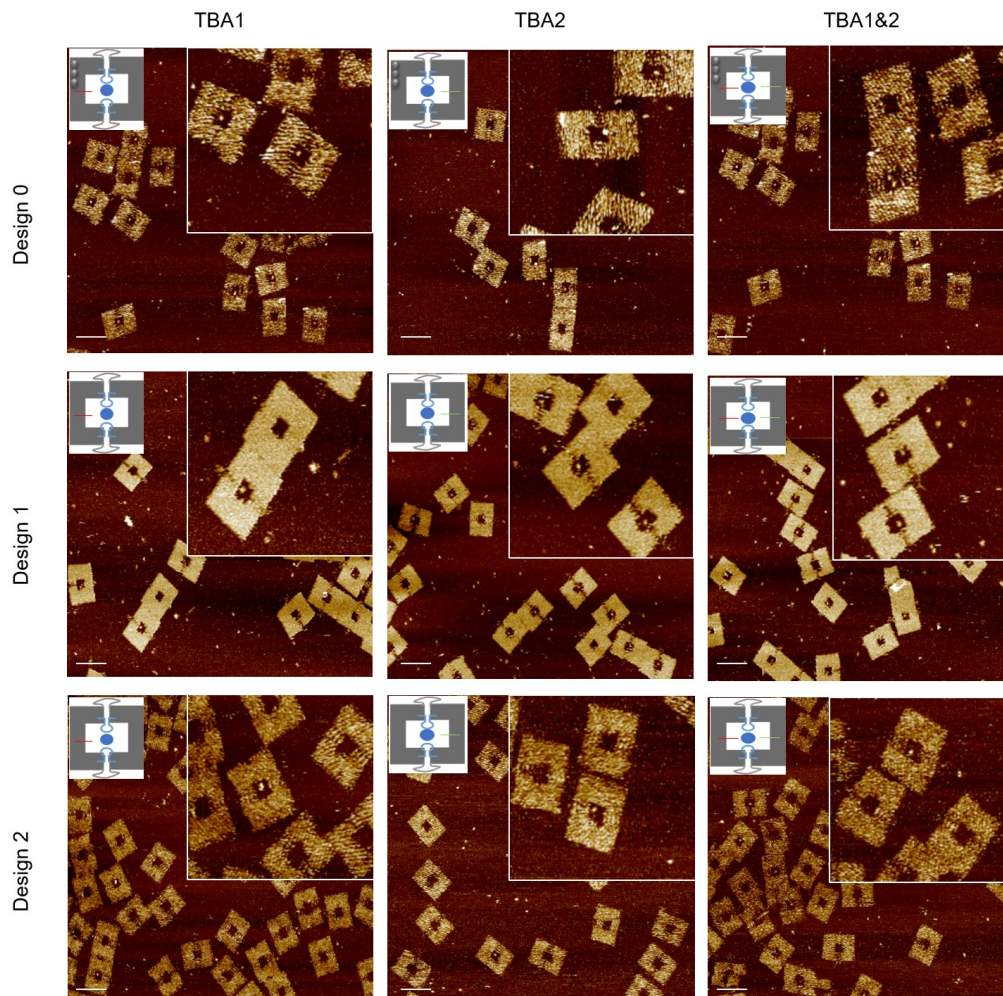


Figure 3-21: AFM characterization of the presented designs 0 (upper row), 1 (middle row) and 2 (lower row) for protein encapsulation. Loading of the DNA chamber with the thrombin protein mostly results in the appearance of single brighter dots in the center of the cage of all designs, visualizing effective protein binding in most cases in a 1:1 ratio. The inner free space of design 0 was chosen to theoretical be able to envelope two thrombin molecules (upper row, right column). Differentiation of thrombin binding to TBA1 (left, left column) and TBA2 (right, middle column) therefore in case for design 0 was performed using 5'-end biotinylated oligo strands, extending orthogonal to the left half of origami plane. Streptavidin addition, served as topographical marker, led to clear discrimination of the responsible binding aptamer. For clarity, a schematic presentation of each samples is presented as small inset in all images. The streptavidin proteins are presented as a single grey circle. Analysis was performed in TEMg 1x buffer. Scale bar are 100 nm.

Contradictorily, in the same condition, the loading efficiency for D1 and D2, increased when bearing only TBA1 (D1: 21.0% \pm 16.9; D2: 19.4% \pm 10.2) and did not change when bearing instead TBA2 (D1: 21.1% \pm 8.5; D2: 4.4% \pm 3.8).

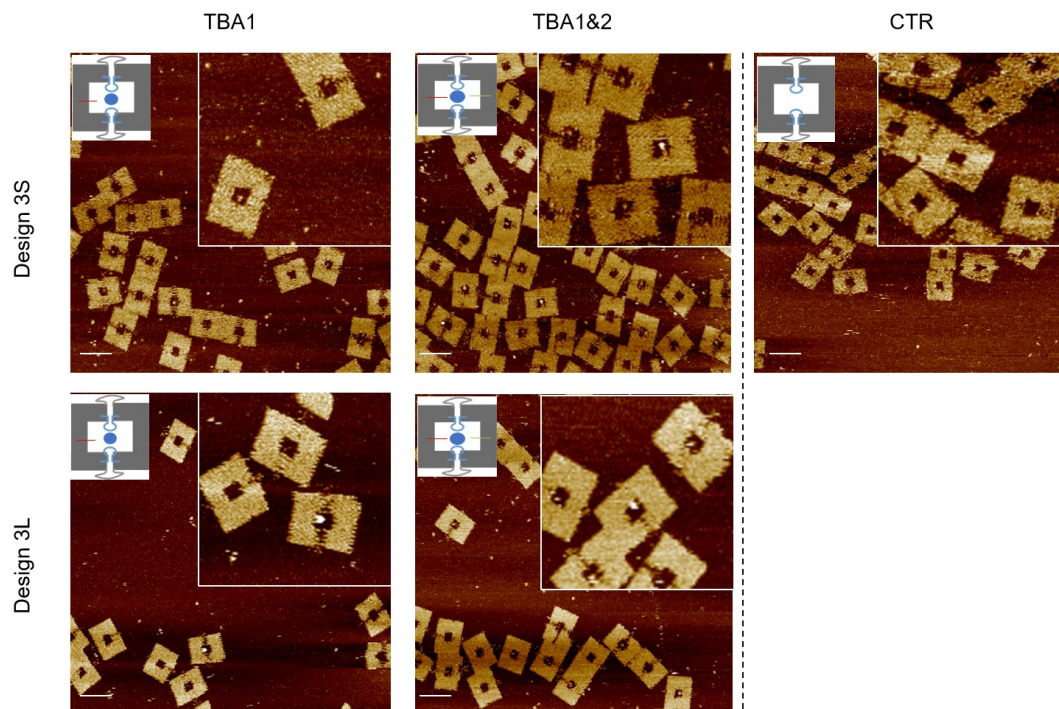


Figure 3-23: AFM characterization of the presented designs 3S (upper row) and 3L (lower row) for protein encapsulation. Loading of the DNA chambers with the thrombin protein mostly results in the appearance of single brighter dots in the center of the cage of both designs, visualizing effective protein binding in most cases in a 1:1 ratio. The analysis for the TBA2 motif was left out as there was no difference of internalization compared to design 1 already presented in figure 3-21. A chamber, bearing no integrated aptamers, demonstrates the binding specificity of the protein to the integrated G4-architectures, resulting in no apparent protein encapsulation. For clarity, a schematic presentation of each samples is presented as small inset in all images. The streptavidin proteins are presented as a single grey circle. Analysis was performed in TEMg 1x buffer. Scale bar are 100 nm.

As control sample, a DNA cage lacking both aptamers within the inner cavity was used, resulting in negligible values of protein encapsulation and thus, demonstrating the specificity of the developed systems to efficiently bind one thrombin molecule within the free space of the inner cavity (CTR: 0.9% \pm 1.4).

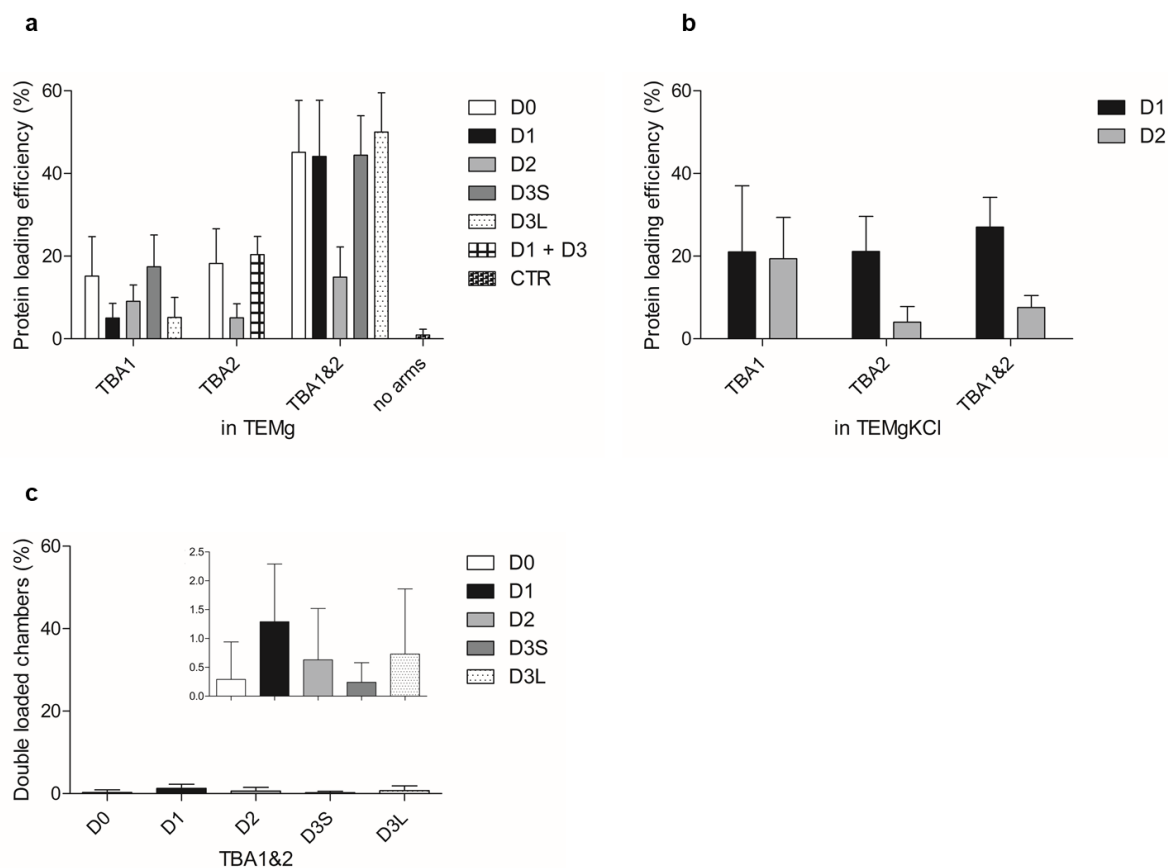


Figure 3-24: Summary of the data (mean + SEM) gained by AFM characterization of the DNA-loaded nanocage with the protein thrombin. Evaluated were the influences of ligand designs on protein loading efficiency as well as the effect of buffer composition. No significant difference could be observed comparing the distinct designs of D0, D1, D3S and D3L. In comparison to that D2 reveals a decreased loading efficiency, suggesting that simultaneous binding of one thrombin unit to both DNA helices is probably more but difficult due to the higher length of the double helices. Furthermore, addition of potassium ions drastically decreases the yield of protein loading in presence of both internalized ligands.

The complete set of data obtained by AFM analysis of the designs is listed in table 3-3.

Table 3-3: AFM- analysis data for yields of protein encapsulation within the presented designs (mean \pm SEM).

Design	Aptamer	Loading efficiencies (%) 1x TEMg	Loading efficiencies (%) 1x TEMg KCl	Double loading efficiency (%) 1x TEMg
D0	TBA1	15.2 (\pm 9.5)	-	-
	TBA2	18.2 (\pm 8.4)	-	-
	TBA1&2	45.1 (\pm 12.5)	-	0.29 (\pm 0.7)
D1	TBA1	5.0 (\pm 3.5)	21.0 (\pm 16.9)	-
	TBA1&2	44.1 (\pm 13.6)	27.8 (\pm 7.2)	1.29 (\pm 1.0)
D2	TBA1	9.1 (\pm 3.9)	19.4 (\pm 10.2)	-
	TBA2	5.1 (\pm 3.4)	4.4 (\pm 3.8)	-
	TBA1&2	15 (\pm 7.3)	7.6 (\pm 2.9)	0.63 (\pm 0.9)
D3S	TBA1	17.4 (\pm 7.7)	-	-
	TBA1&2	44.4 (\pm 9.6)	-	0.24 (\pm 0.3)
D3L	TBA1	5.2 (\pm 4.8)	-	-
	TBA1&2	50.0 (\pm 9.5)	-	0.73 (\pm 1.1)
D1 + D3	TBA2	20.4 (\pm 4.5)	21.1 (\pm 8.5)	-
w/o arms	-	0.9 (\pm 1.4)	-	-

Additionally, to prove successful protein encapsulation, gel electrophoresis was performed, however, leading to unsatisfactory results (figure 3-25). To enable optical characterization of the encapsulated protein, this latter was previously modified with fluorescent dyes on its outer surface, using standard chemical modification techniques (see section 4.2.2.3). Unfortunately, this compromised the stability of the protein and high protein amounts were lost during the purification process. Therefore, only very low levels of protein could be identified by gel electrophoresis (very weak band visible in lane 3).

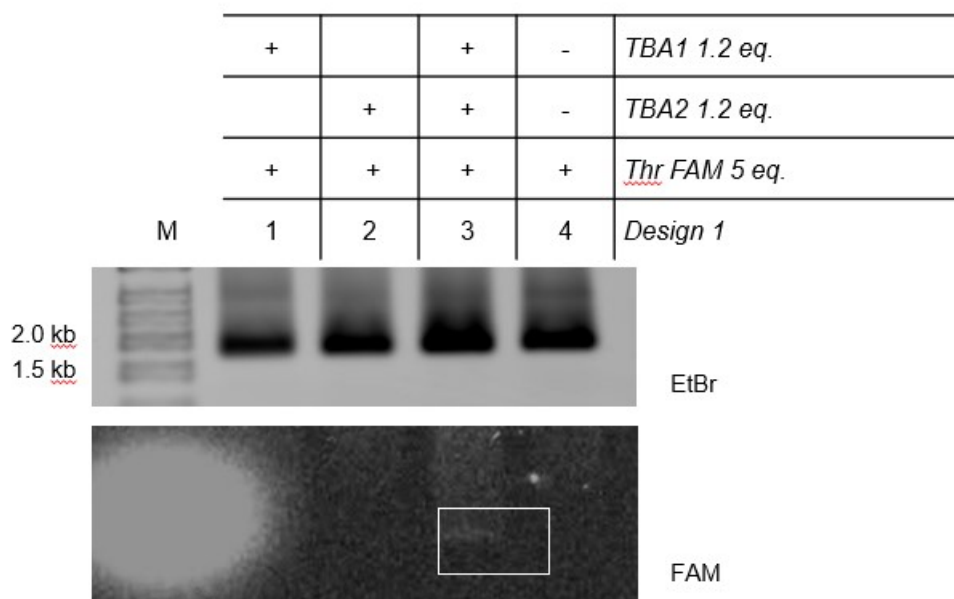


Figure 3-25: Gel electrophoresis characterization of design D1. Only lane 3 containing the sample with both internalized ligands show a slightly weak band. The labelling strategy applied and the extensive protein manipulation used are therefore unsuitable for characterization of protein binding by gel electrophoresis. Gel running parameters: 0.75% agarose, 2.5 h, 80 V by 4°C in TBEMg 1x. Lane M contain a 1 kb DNA ladder.

3.3.4 Proteolytic activity of the caged thrombin protein within the DNA origami frame

The data shown until now demonstrated that through the manipulation of the ligand-to-ligand binding distances and ligand flexibility within the inner cavity of the devices (D0, 1, 2, 3S and 3L), the loading efficiency of thrombin could be affected. The avidity effect plays an enormous role for bivalent binding and distinct buffer compositions have massive impact on the binding efficiency of the protein. In this section, the influence of the DNA environment on the proteolytic activity of the encapsulated protein will be examined.

At this purpose a specific catalytic assay at appropriated conditions was established to define the enzymatic characteristics of the enveloped protein. Here a defined FRET substrate (FAM-GG-D-Phe-PR-SGGG-Lys[BHQ-1]-K-OH) and a substrate, containing the donor fluorophore only (FAM-GG-D-Phe-PR-SGGGK-K-OH) were used to determine the Michaelis-Menten kinetic parameters of the hosted thrombin protein in

TEMg 1x at 37°C (see Supplementary Information, Evaluation of the proteolytic activity of the caged protein).

Figure 3-26 illustrates the data obtained for the D1 internalized ligand configuration **(a)** and for the same aptamers freely moving in solution **(b)**. The initial enzymatic reaction rates were evaluated for a starting thrombin concentration of 30 nM and DNA origami devices/aptamers in 100 nM concentration upon addition of different FRET substrate concentrations ranging from 0 to 50 μM .

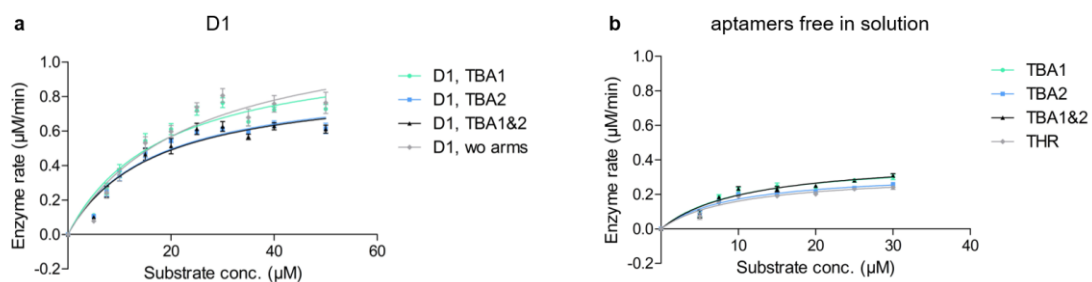


Figure 3-26: Activity of thrombin within the DNA origami device featuring the ligands in D1 configuration **(a)** compared to the aptamers freely moving in solution **(b)** evaluated at 100 nM. Thrombin was diluted in TEMg 1x, pH 7.6, to a final concentration of 30 nM. The reaction was performed at 37°C using different FRET substrate concentration ranging von 0-50 μM diluted in DMSO. The data revealed an enormous enhancement of proteolytic activity of the protein upon caging compared to freely moving aptamers in solution. Interestingly in construct D1 a reduction in activity can be observed accompanied by the integration of the number of binding aptamers: no arms (wo) > D1, TBA1 > D1, TBA2 > D1, TBA1&2. Shown are mean values \pm SEM obtained out of three independent experiments made by triplicates. The assay was performed at 37°C in 1x TEMg.

The analysis revealed that the proteolytic activity is *per se* enhanced in presence of DNA, as clearly shown by the slight increase of enzymatic rate (v_{max}) when going from the protein-only sample (THR: $0.32 \pm 0.03\%$) to the samples containing free aptamers in solution (TBA1: $0.40 \pm 0.04\%$, TBA2: $0.33 \pm 0.03\%$ and TBA1&2: $0.41 \pm 0.04\%$) **(b)**. Interestingly, the integration of the aptamer ligands within the origami frame led to an almost three-fold improvement of the enzymatic activity of the protein as compared to the freely diffusing DNA ligands (D1, TBA1: $1.1 \pm 0.09\%$, D1, TBA2: $0.9 \pm 0.06\%$, D1, TBA1&2: $0.8 \pm 0.09\%$) **(a)**. This is in agreement with the results Zhang *et al.* observed [84]. The locally dense negative environment provided by the surrounding DNA structure, may induce the formation of an ordered hydration layer in the near proximity of the protein surface, stabilizing the protein and supporting substrate channeling by

dynamical long-range interactions between polar and charged groups. These characteristics compared to bulk water were shown to be very crucial for protein activity and protein folding reaction [68;135;136]. Furthermore, the data revealed a slight reduction in protein activity accompanied by the integration of the aptamers: no arms (wo): $1.2 \pm 0.1\%$ > D1, TBA1: $1.1 \pm 0.09\%$ > D1, TBA2: $0.9 \pm 0.06\%$ > D1, TBA1&2: $0.8 \pm 0.09\%$. This effect could be due to allosteric configurational changes of the protein upon aptamer binding, eventually altering the accessibility of the substrate to the active site of the protein [130;137]. The reduced conformational freedom of the tertiary structure upon binding of the aptamers to the outer surface of the protein restrains the flexibility of the protein and may be even more pronounced in presence of the surrounding DNA origami frame than in the presence of freely diffusing aptamers. This consequently might have an even higher influence on the allosteric effect including long range correlated motions, which in turn alter the kinetic characteristics of the thrombin molecule. Molecular dynamics simulation already demonstrated that, upon aptamer binding, the ground state of the protein is thermodynamically and kinetically favored [138]. Therefore, it can be assumed that scaffolding the protein to a more rigid platform might lead to a higher structural change accompanied by conformational free energy alterations, which may strongly affect protein's function as a result of deviations in the local environment.

Table 3-4 and table 3-5 summarize the obtained data for design 1 and the aptamers freely moving in solution.

Table 3-4: Summary of Michaelis-Menten kinetic evaluation (mean \pm SEM) for aptamers moving free in solution, i.e. not tethered to the DNA origami platform.

Values	TBA1	TBA2	TBA1&2	THR
Michaelis-Menten- kinetic				
V_{max}	0.40 (\pm 0.04)	0.33 (\pm 0.03)	0.41 (\pm 0.04)	0.32 (\pm 0.03)
K_m	10.4 (\pm 2.5)	9.3 (\pm 2.0)	11.2 (\pm 2.6)	10.1 (\pm 2.2)
k_{cat}	20.0 (\pm 1.9)	16.6 (\pm 1.3)	20.7 (\pm 1.9)	16.1 (\pm 1.4)
R²	0.91	0.92	0.92	0.93

Table 3-5: Summary of Michaelis-Menten kinetic evaluation (mean \pm SEM) for design 1.

Values	D1, TBA1	D1, TBA2	D1, TBA1&2	D1, wo arms
Michaelis-Menten- kinetic				
V_{max}	1.1 (\pm 0.09)	0.9 (\pm 0.06)	0.8 (\pm 0.09)	1.2 (\pm 0.1)
K_m	18.6 (\pm 3.7)	16.6 (\pm 2.7)	14.6 (\pm 4.7)	23.6 (\pm 5.7)
k_{cat}	54.7 (\pm 4.6)	45.3 (\pm 2.9)	37.9 (\pm 4.5)	61.9 (\pm 6.9)
R²	0.91	0.94	0.79	0.9

For clarifying the impact of the distinct designs, particularly in terms of structural flexibility of the integrated aptamers, the enzymatic rates for D1, D2 and D3, all featuring both ligands within the inner space of the structure, were evaluated and compared to the proteolytic activity of the protein in presence of freely diffusing aptamers (figure 3-27, **(b)**). The results show that D1 displays the highest proteolytic activity compared to the other analyzed systems: D1 $0.8 \pm 0.09\%$ > D2 $0.7 \pm 0.05\%$ > D3L $0.5 \pm 0.03\%$ \approx D3S $0.4 \pm 0.02\%$ \approx aptamers free in solution $0.4 \pm 0.04\%$. As the initial concentration of bound protein can be assumed to be almost equal in all systems (demonstrated by AFM analysis, section 3.3.3), this effect might be due to different allosteric configurational effects upon ligand binding to the surface of the protein as a result of the different geometric arrangements of the internalized G4-motifs in the origami frame.

Additional molecular dynamic simulations and/or structural studies of the DNA-protein constructs will be necessary to better explain this observation. However, the data obtained show the potential use of DNA nanotechnology for the construction of biomaterials with controllable enzymatic activity, applicable for biotechnological purposes.

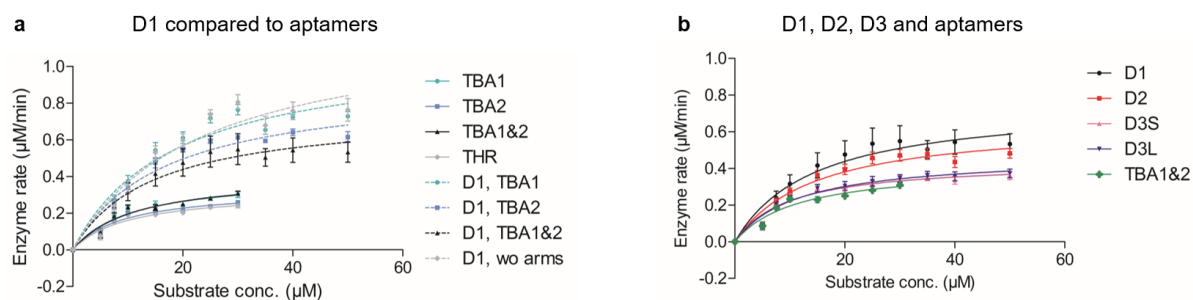


Figure 3-27: Activity of thrombin within the DNA origami device featuring the ligands in a D1 configuration compared to the aptamers freely moving in solution (a) and data set for the distinctive designs applied during this study (b), all evaluated at 100 nM. Thrombin was diluted in TEMg 1x, pH 7.6, to a final concentration of 30 nM. The reaction was performed at 37°C using different FRET substrate concentrations ranging von 0-50 µM diluted in DMSO. Shown are the results for all systems with both integrated aptamers. The values obtained for construct D1 show the highest proteolytic activity of the protein compared to the other systems investigated during this study: $D1 > D2 > D3L \approx D3S > \text{aptamers free in solution (TBA1\&2)}$. Shown are mean values \pm SEM obtained out of three independent experiments made by triplicates. The assay was performed at 37°C in 1x TEMg.

Table 3-6 gives an overview of the data for all analyzed DNA cage designs and the aptamers freely moving in solution.

Table 3-6: Summary of Michealis-Menten kinetic evaluation (mean \pm SEM) for design 1, 2, 3S, 3L and both aptamers moving free in solution.

Values	D1	D2	D3S	D3L	TBA1&2
Michaelis-Menten- kinetic					
V_{\max}	0.8 (\pm 0.09)	0.7 (\pm 0.05)	0.4 (\pm 0.02)	0.5 (\pm 0.03)	0.4 (\pm 0.04)
K_m	14.6 (\pm 4.7)	14.5 (\pm 2.8)	9.6 (\pm 1.7)	11.4 (\pm 2.0)	11.2 (\pm 2.6)
k_{cat}	37.9 (\pm 4.6)	32.8 (\pm 2.4)	21.9 (\pm 1.2)	23.7 (\pm 1.4)	20.7 (\pm 1.9)
R^2	0.79	0.91	0.91	0.91	0.92

4 Material and Methods

4.1 Material

All materials used during this study are listed in the supplementary information sections (see E Supplementary Information).

4.2 Methods

4.2.1 Development of a versatile DNA nano-chamber with modular and programmable size

4.2.1.1 Design of the DNA reconfigurable nanostructure

The reconfigurable DNA origami nano-chamber was designed using SARSE (available at <http://cdna.au.dk/software/> and caDNAo), as already reported by our group [44;113].

For the construction of the DNA origami devices, the single stranded m13mp18 plasmid, produced from phage DNA in *E.coli* (see section 4.2.1.2) [139], was folded into a rectangular shape with the help of short, computational pre-designed oligonucleotides, so called staple strands. The construct mimics a reconfigurable plug with about 90 nm in length x 65 nm in width and an internal cavity about 20 nm x 20 nm. Due to the circular scaffold folding pathway used in most two-dimensional origamis, the structure consists of two halves joint together by a central seam. Control over the size of the inner chamber size was achieved by modifying the sequences of the central seam of the origami structure with small, mechanically switchable hairpin loop motifs, enabling to manipulate the end to end distance of the two halves of the structure in a trigger dependent fashion. Therefore, the seam of the structure was adapted to bear different number of hairpin motifs, depending on the design (construct 0, I, II & III, see figure 4-1), which connects the two adjacent halves at both ends. All hairpins are identical, they are all tethered to the central seam and aligned in parallel (in total 18 for construct I and 36 for construct II & III).

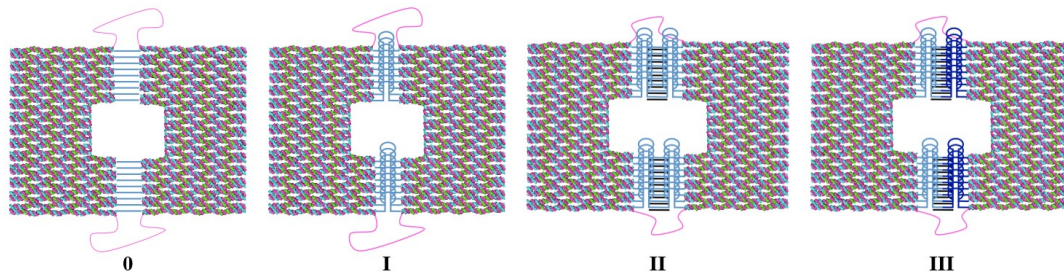


Figure 4-1: Overview of the distinctive designs used in this study. Four classes of constructs were designed, differing in the number and type of hairpin motifs located in the central seam of the structure: no hairpins (0), one set of parallel hairpins (I), two identical (II) or two distinct (III) sets of parallel hairpins.

Additionally, an unpaired scaffold segment at the top and the bottom extremity (140 and 141 bases, indicated by magenta lines) lends the structure a higher degree of flexibility and therefore allows the two parts to move apart during the mechanical device operation driven by the DNA-induced conformational transition. The inner loop features of all designs can be addressed with “fuel” strands (orange) complementary to the hairpin motifs, containing a toehold sequence at the 3’-end. The hybridization of the fuel oligonucleotide to the hairpin motif of the compact closed device leads to a formation of a more stable 15 bp long double helical domain in case of construct I, 42 bp respectively for construct II & III, and therefore to a conformational transition along the helical axes (open state) with an increased size of the inner cavity. The increased size in construct I is about 5 nm, for construct II and III is about 10 nm. Switching back to the initial closed state is achieved by single-strand displacement. For this purpose, fully complementary “antifuel” strands (in green) are hybridized to the toehold-appended fuels (orange), which are then displayed by the central seam in the open state of the device. This process can be theoretically repeated, allowing full reversibility of the mechanical devices operation. This process is schematically shown in figure 4-2 [44;113].

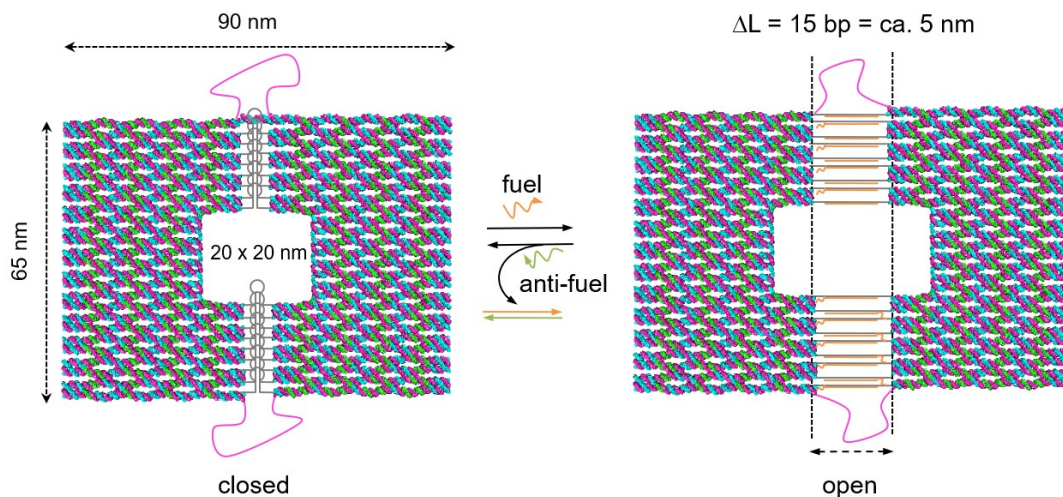


Figure 4-2: Schematic representation of the operational movement for construct I. The two halves of the device are joint by integrated hairpin motifs in the common seam sequences and an unpaired scaffold segment at the bottom and top extremity. These features confer the whole structure a distinctive degree of flexibility and therefore permit the operational movement of the device. Opening of the plug is achieved by addition of “fuel” strands (orange), which leads to a DNA-induced transition along the helical axes leading to a more stable double helical domain. The reversible switching to the initial closed state is realized with the help of fuel strands containing a short toehold sequence at the 3'-end. Due to addition of fully complementary “antifuel” strands (green), the “fuel” strands can be removed from the origami structure by single strand displacement.

Figure 4-3 illustrates the design of the inner seam sequence of construct I. The motifs were designed to display an internal 15 nucleotides hairpin region, featuring a C₅T₅G₅ secondary structure (grey). The hybridization of the fuel strands (orange) with a short CGCG toehold leads to an extension along the helical axes of about 5 nm. The addition of the fully complementary antifuel strand (green) allows to switch back to the initial closed state of the device, giving the device the dynamic operational characteristic.

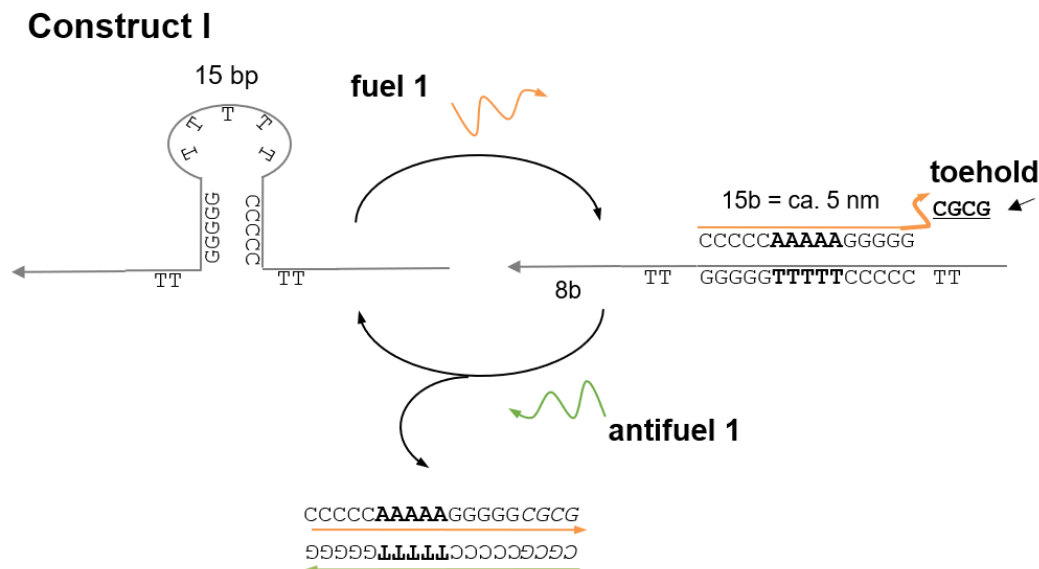


Figure 4-3: Detail design of the hairpin motif used in construct I. Presented is the DNA induced transition of the correct folded 15 bp long hairpin loop (grey) along the helical axes. Hybridization of the fuels (orange) with a CGCG toehold and addition of fully complementary antifuel strands (green) allow the realization of an efficient reconfiguration of the operation mode, switching back to the initial closed state.

In contrast to construct I, construct II bears two identical sets of parallel 15 bases-long hairpin motifs in series which are joined by two 12 bp long double helical inner segments (segment A or B, see figure 4-4). This results in a total end to end distance between the two halves of about 4 helical turns, enabling them to lay in the same orientation in respect to the plane of the construct. The sequence of the 2 loops are identical to the hairpin used in construct I (C₅T₅G₅). Upon fuel addition (in orange), the length of the inner cavity is about 10 nm (2x5 nm given by the loops extension summed up to the previously present 12 bp inner segment). This enlarges the structural complexity of the system, allowing to place molecules of different shapes and dimensions inside its inner cavity.

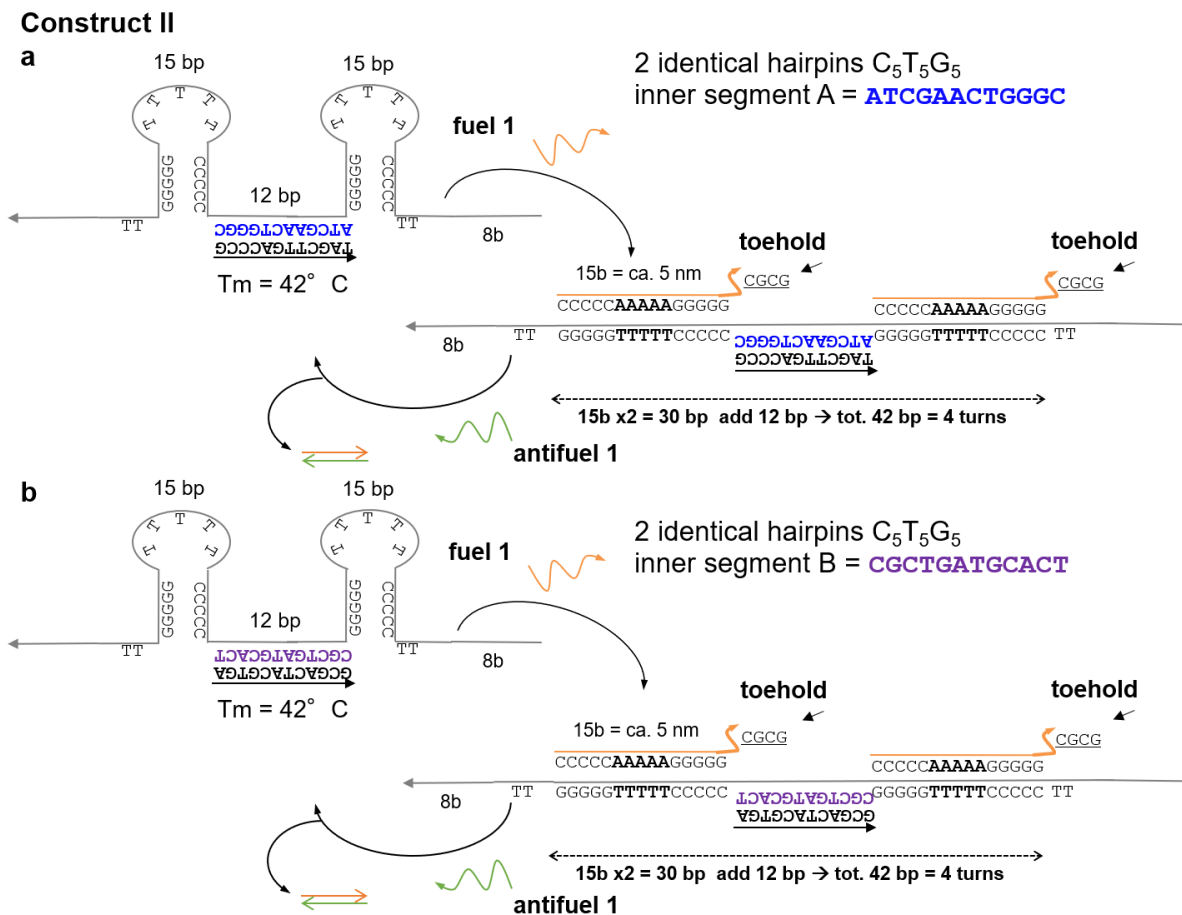


Figure 4-4: Design of the hairpin motifs for construct II. The sequences of the hairpins ($C_5T_5G_5$) are identical with the hairpin used in construct I. Two inner segments, which form a double helical domain and connect the two hairpins, were designed using NUPACK (segment A 5'-ATCGAACTGGGC-3' (a) and segment B 5'-CGCTGATGCACT-3' (b)). In the assembled design, the inner segments were stabilized by fully complementary oligonucleotides (stabilizing segments). The conformational transition upon fuel addition (in orange) leads to an increase of the size of the inner cavity of about 10 nm of the nanostructure compared to 5 nm in construct I.

This concept can be further extended, creating a four-state device. Therefore, construct III was designed to display two different sets of parallel hairpin motifs, one next to the other in series (see figure 4-5). Each motif (hairpin 1: $C_2TC_2T_5G_2AG_2$; hairpin 2: $GCTGCT_5GCAGC$) can be individually addressed with the corresponding complementary fuel strands (orange). In contrast to construct I and II, the fuel strands of construct III have been designed with a 10 bases-long toehold in order to reach a higher selectivity. Here only the connecting inner segment B was inserted to stabilize the motif. Two different inner segments have been explored in construct II and screened for their efficiency in cycling the device operation (named A and B, see Figure 5.4). Segment B was found to be more efficient and therefore chosen in construct III to stabilize the

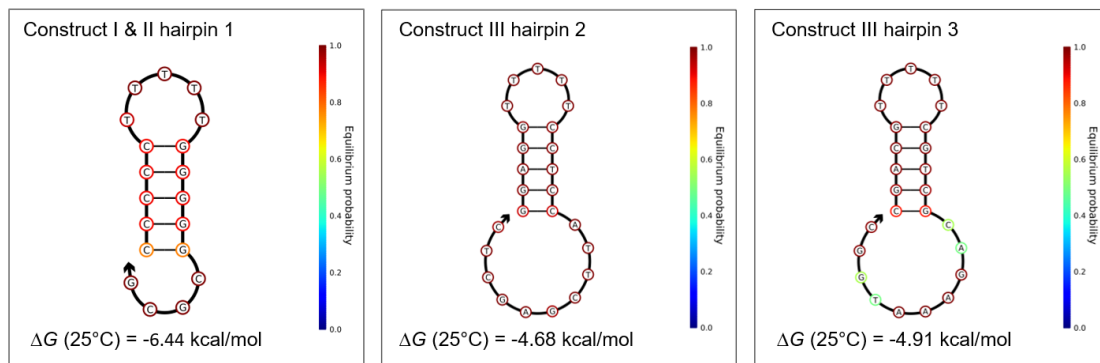


Figure 4-6: NUPACK analysis of the different hairpin motifs used in this study for construct I, II and III. The energetic parameters of the different hairpins are comparable with each other. The small difference can be addressed to the variance in base content.

As mentioned above, the focus of this study was to adapt the size of the inner cavity of the structure to encapsulate cargos of different shapes and dimension. At this purpose, the extent of the linear translations, which can be modulated by the different sets of hairpin motifs/fuel strands displayed by different constructs (either 1 (I), 2 identical (II) or 2 different (III) hairpins), is important. Applying these proposed design principles will thus generate more versatile nanochambers with modular and programmable size. In literature, two well-known aptamers, defined by SELEX and forming a G-quadruplex structure, here named as TBA1 (5'-GGTTGGTGTGGTTGG-3') and TBA2 (5'-AGTCCGTGGTAGGGCAGGTTGGGGTGACT-3'), are described as binding to the positively charged surface of the protease thrombin with high affinity [70;71]. Therefore, the inner cavity of the reconfigurable plug was modified to display these two G-quadruplexes at different intermolecular distances and with distinct degrees of rotational freedom and such to face the corresponding binding sites of the protein thrombin surface. TBA1 binds primarily to the fibrinogen recognition exosite I (left anchoring point of the inner cavity, in green) and TBA2 binds to the heparin binding exosite II (right anchoring point, in red) of the protein surface. For the activity and binding studies (section 4.2.3 and 4.2.2.3) a total of 4 distinctive designs (0-4) were realized (see figure 4-7). D0 (**a**), was designed to display shorter and less flexible arms, but a larger inner room available compared to D1 (**b**) longer, more flexible arm but smaller room available inside the inner cavity), D2 (**c**) higher degree of rotational freedom and flexibility, but the less inner space) and D3 (**d**), where TBA1 is linked to the complementary strand through a short (T₁₀, D3S) or a long (T₁₆, D3L) spacer. In D3, the anchoring of the TBA2 arm is identical to D1.

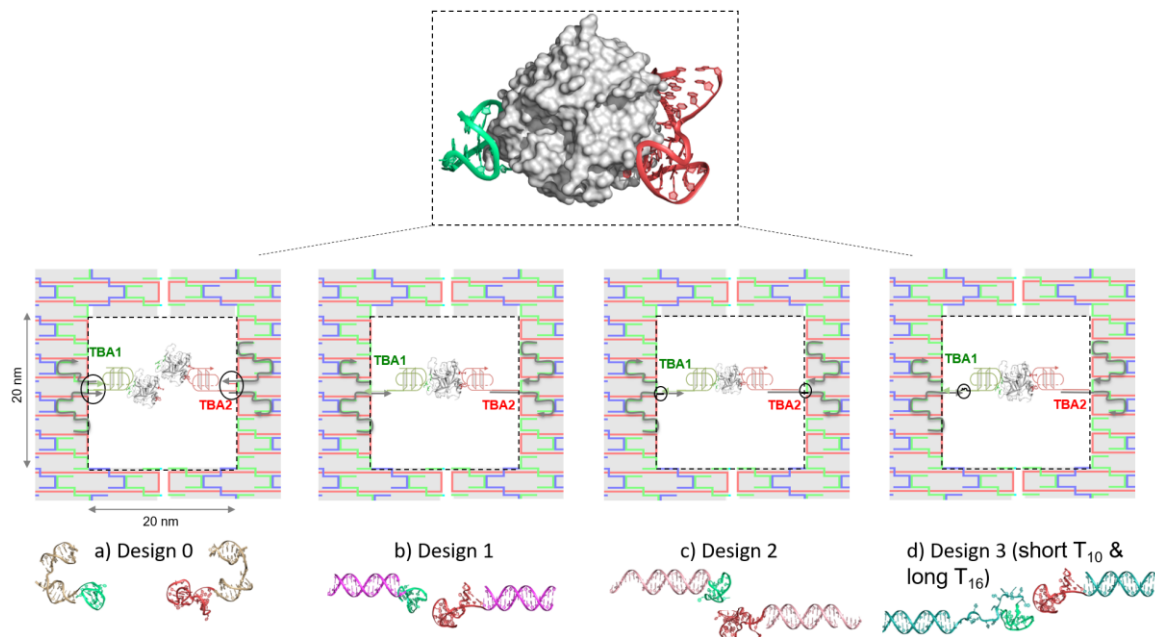


Figure 4-7: Schematic representation of the modification of the inner cavity to encapsulate the protein thrombin. In total 4 staple strands of the original cage design were replaced to integrate protruding arms, pointing towards the center of the inner cavity (in grey). These protruding arms are complementary to the modified ends of the thrombin binding aptamers (TBA1 and TBA2), which are responsible for binding to two highly positively charged parts of the surface of the protein, the fibrinogen exosite I (in green) and the heparin exosite II (in red). The theoretical diameter of the protein molecule is about 5 nm. Thus, in design 0 (a) the available space inside the cavity can be filled theoretically by two protein molecules. The distance between the two protruding arms in design 1 (b) is about 12 nm, enabling to place one protein inside the inner cavity. Additional 7 bases were added at each arm in design 2, making the design more flexible (c). (d) Lending the TBA1 catching arm a higher degree of flexibility a T_{10} or a T_{16} spacer was integrated in design 3 (short & long) compared to design 1. Black circles mark the difference between the distinct designs. [PDB codes: 4DIH & 4I7Y].

4.2.1.2 Scaffold m13mp18 preparation

All cell culture procedures were performed under sterile conditions using a laminar flow clean bench (Scanlaf) to avoid contaminations. All buffers, antibiotics and reagents were used sterile.

For the assembly of the DNA host system (see section 4.2.1.1) a long, circular ssDNA is needed, which can be folded in the desired shapes with the help of short computational pre-designed staple strands. In our study, we choose the single stranded m13mp18 plasmid from the m13mp18 phage. The phage DNA was produced using *E.coli* as previously reported [139]. Briefly, 25 μ l XI1 blue *E. coli* (# 200249, Agilent Technologies) competent cells were resuspended with 50 nM of the phage DNA (# 4263193, Affymetrix). The cells were then placed on ice for 10 min and afterwards heat

shocked at 42 °C for 30 sec. After 5 min incubation on ice, the cell/DNA solution was suspended in 200 µl NZA media without any supplements. Cells were recovered by placing the solution in a thermoshaker (Eppendorf) at 37 °C for 1.5 h at 150 rpm, and then plated onto pre-warmed standard I agar plates, containing 12.5 µg/ml tetracycline (tetra), 40 µg/ml IPTG and 100 µg/ml X-gal, overnight at 37 °C. In parallel an overnight culture of the XL-1 blue *E. coli* competent cells was started in 100 ml NZA media containing 12.5 µg/ml tetra at 37 °C and 180 rpm (New Brunswick Scientific).

During the next morning 2 l of 2x YT media (12.5 µg/ml tetra, 5 mM MgCl₂) was inoculated by the overnight culture in a 1:40 ratio and the culture grown at 37 °C and 180 rpm (New Brunswick Scientific) till an optical density of 0.3 at 600 nm wavelength (OD₆₀₀) was reached. Afterwards, the culture was infected with selected, plasmid-transfected plaques from the overnight grown agar plate. The cell culture was then incubated further for 3.5 h at 37 °C and 180 rpm (New Brunswick Scientific).

After the end of the incubation time the bacteria were pelleted by centrifugation at 4,000 rcf at 4 °C for 15 min (5810 R, Eppendorf). The supernatant was transferred into a fresh flask. By adding 40 g/l PEG 8000 and 30 g/l NaCl to the supernatant and incubating the solution stirred on ice for 30 min, the phage particles inside the solution were precipitated, causing a turbid solution. The phages were pelleted by centrifugation at 4,000 rcf at 4 °C for 15 min (5810 R, Eppendorf). This time the supernatant was decanted and the remaining supernatant at the bottom of the flask was carefully removed from the phage pellet. Afterwards the pellet was actively resuspended in 1/100 of the original volume with 10 mM Tris buffer pH 8.5. To get rid of the remaining *E. coli* particles, the pellet was centrifuged by 21,000 rcf for 15 min at 4 °C (5430 R, Eppendorf). The cleared supernatant was then transferred in a fresh container and stored at -20°C until further processing.

The lysis of the phage was achieved by thawing the supernatant on ice and adding 2 volumes of lysis buffer (Macherey-Nagel). The solution was gently mixed by inversions. After addition of 1.5 volumes of the neutralization buffer (Macherey-Nagel), the mixture was incubated in an ice-water bath for 15 min and then centrifuged at 16,000 rcf for 10 min at 4 °C (5430 R, Eppendorf). The supernatant was transferred into a clean flask before adding 1 volume of 99.9% pure ethanol and incubating the solution in an ice-water bath for 30 min. Afterwards, the solution was centrifuged by 16,000 rcf for 15 min at 4 °C (5430 R, Eppendorf). The supernatant was discarded, and the residual pipetted out carefully. Here after, the pellet was resuspended in a suitable amount of 10 mM

Tris, pH 8.5 (2-4 ml). The isolated scaffold can be quantified using the absorption maximum of the aromatic purine- and pyrimidine-bases. The determination of the concentration and the degree of purity of the total amount of isolated DNA was carried out by spectroscopic analysis at 260 nm wavelength using a DeNovix (Delaware) instrument. The calculation of the DNA concentration and molarity by means of the OD is based on the Lambert-Beer law. It allows to connect the intensity of the light transmitted with the concentration of the measured sample, as shown in equation (eq. [4-1] - eq. [4-3])

$$E = \log\left(\frac{I_0}{I}\right) = \varepsilon * c * d$$

Eq. [4-1]

$$c \left[\frac{\mu\text{g}}{\text{ml}} \right] = OD_{260} * V * F$$

Eq. [4-2]

$$c \left[\frac{\mu\text{mol}}{\text{ml}} \right] = \frac{OD_{260} * F * V}{M}$$

Eq. [4-3]

with:

E: extinction

I₀: intensity of the entering light

I: intensity of the exiting light

ε: absorption coefficient (depending on the sample and wavelength)

d: thickness of the cuvette

c: concentration

OD: optical density

V: dilution factor

F: extinction coefficient (ssDNA 33 μg/ml; dsDNA 50 μg/ml;)

M: molecular weight

The achievement of a properly folded DNA origami structure is strictly dependent on the quality of the m13mp18 scaffold used: not only the sample should be pure but the

sequence should be correct. To verify the correctness of the cloned sequence (i.e. the desired m13mp18 sequence), capillary electrophoresis was used. This method is based on standard Sanger sequencing. Therefore, different primers (1-17) (see E Supplementary Information, table e-14) were adjusted to 10 μM and the m13mp18 to 100 ng/ μl . The different samples were then sequenced by the company GATC. Evaluation of the sequencing results were evaluated using the DNASTAR Lasergene 12, SeqMan Pro, Version 12.2.0(82), 421 software.

4.2.1.3 Assembly of the DNA origami host

All DNA nanochamber constructs described above were assembled by slow thermal annealing and characterized using gel electrophoresis analysis (section 4.2.5.1) and atomic force microscopy (section 4.2.5.2).

In general, the assembly protocol of the DNA structures was based on the Rothmund procedure, using different molar ratios (as stated in the different experiments) between the m13mp18 scaffold (from 2 nM to 50 nM) and each of the staple strands in 1x TEMg buffer (100 nM, 250 nM) in a total volume of 1 ml [19]. The structures were assembled from 70 $^{\circ}\text{C}$ to 20 $^{\circ}\text{C}$ at a $-1^{\circ}\text{C}/\text{min}$ on a thermocycler (Mastercycler Nexus Gradient, Eppendorf) with an initial denaturation at 90 $^{\circ}\text{C}$ for 5 min. The opening process of the device was initiated by adding 1.2- or 1.5-equimolar amount of fuel strands (for construct I and II, III, respectively) and letting the DNA hybridize from 40 $^{\circ}\text{C}$ to 20 $^{\circ}\text{C}$ at $-1^{\circ}\text{C}/\text{min}$, followed by at least 12 h incubation at room temperature. Switching back to the initial closed state of the structure was achieved by adding, respectively, 1.5- (construct I) or 5- (construct II and III) equimolar amounts of antifuel strands in respect to the previously added toehold appended fuels and following the same hybridization protocol used during the opening process. After purification of the structures (see section 4.2.1.4), all devices were characterized by gel electrophoresis (see section 4.2.5.1) and atomic force microscopy (AFM, section 4.2.5.2).

4.2.1.4 Purification of the assembled nanostructures

If not stated differently, the assembled structures were purified using PEG precipitation according to the protocol developed by Stahl and coworkers [140]. This allowed to achieve a high purity grade of the samples, a high concentration of the origami structures for further experimental processing and – in case – a resuspension of the structure in a desired buffer solution.

Briefly, the total Mg concentration in the samples was adjusted to 21 mM in 1x TEMg. After the PEG buffer had been added in a 1:1 ratio to the sample mixture, the solution was suspended by slight inversion and centrifuged at 16,000 rcf for 30 min at room temperature (5424 R, Eppendorf). The supernatant was carefully removed and the samples dissolved in the desired target buffer, mostly TEMg 1x. In the last step, the solutions were incubated at room temperature overnight prior to further use. In some rare cases, samples were concentrated using 100 kDa centrifugal filters (4,500 rcf, 5 min, 20 °C, 4 times, 5424 R, Eppendorf) to a volume of about 30 µl instead of using PEG precipitation.

4.2.1.5 Determination of the concentration of the assembled DNA nanostructures using quantitative Real Time-Polymerase Chain Reaction (qRT-PCR)

A robust qRT-PCR method to determine the concentration of the assembled nanostructures was developed during this study. For this, a specific TaqMan probe, targeting the m13mp18 scaffold backbone of each design, was designed using Custom TaqMan® Assay Manufacturing and Plating software tool (Thermo Fisher scientific). A calibration curve for concentration evaluation was obtained using a dilution series of the m13mp18 plasmid, further amplified by the custom-built probe (# 4331348, Thermo Fisher Scientific): The equation fit was then used to calculate the concentration of a desired DNA origami structure. PCR experiment and data analysis were performed using a CFX96 real time system and the software's CFX Manager™ 3.0 (BioRad). All running parameters are listed in table 4-1 to table 4-3.

Table 4-1: Assay-Mix (# 4331348).

Reagents	Concentration [µM]
Primer for	18
Primer rev	18
TaqMan probe	5

Table 4-2: Master-Mix qRT-PCR.

Reagents	Volume [μ l]
Mastermix (# 4369016)	10
Assay-Mix (# 4331348)	1
DNase free water	7
DNA origami sample	2

Table 4-3: Cycle parameter.

Reaction	Time	Temperature [$^{\circ}$ C]	Cycles
Uracil-n-glycosylase activation	2 min	50	1
Taq polymerase activation	10 min	95	1
Denaturation	15 sec	95	40
Annealing/Extension	1 min	60	40

4.2.2 Protein processing

Structural characterization of the protein binding to the DNA frame device would require (i) a topographical marker for atomic force microscopy (AFM) analysis (section 4.2.5.2) and an appropriated thrombin fluorescence label for the gel electrophoresis characterization (section 4.2.5.1, see figure 4-8). To distinguish the protein aptamer pair forming inside the inner cavity, three staples on the left half of the structure were modified at their 5'-end to bear each a biotin moiety pointing above the origami plane. These biotin molecules are capable to bind to the protein streptavidin, resulting in the appearance of bright spots under AFM inspection, i.e. they can be used as topographical markers. Using this method, protein binding to TBA1 (left side of the structure) can be differentiated from protein binding to TBA2 (right side of the structure), in case both aptamers are integrated into the design (see figure 4-7 in section 4.2.1.1).

Furthermore, the fuel strands used to achieve the translational movement along the helical axes (section 4.2.1.1) can be modified to feature a biotin molecule at the 5'-end. The binding of streptavidin to the biotin molecule can therefore be used to characterize the operational reconfiguration of the proposed designs (construct 0, I, II and III). However, commercially available streptavidin has a high tendency to aggregate.

To circumvent this drawback, a genetically modified streptavidin protein, including only the amino acids 16-133, was produced (section 4.2.2.1).

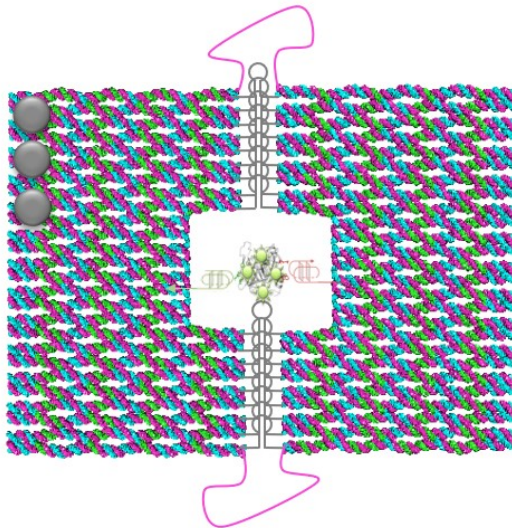


Figure 4-8: Schematic representation of the DNA origami structure modified with three oligonucleotides on the left side of the device (topographical marker) and containing a biotin molecule at the 5'-end, extending out of the origami plane. These are capable to bind three single streptavidin molecules (grey circles). Inside the inner cavity the fluorescence labeled thrombin molecule is caught by the two binding aptamers (TBA1 and TBA2).

4.2.2.1 Expression and purification of the streptavidin protein

Streptavidin was produced using the pTSA-13 plasmid, a gift from Takeshi Sano Laboratory (Addgene plasmid # 17327) [141]. The plasmid was delivered in a bacterial glycerol stock and one bacterial clone was isolated by means of dilutions plating on a NZA agar plate containing 200 $\mu\text{g}/\text{ml}$ ampicillin (amp) overnight at 37 $^{\circ}\text{C}$. To reproduce the plasmid DH5 α *E. coli* cells (Thermo Fisher Scientific) were used. Therefore a 22 ml DH5 α *E. coli* cell culture with 200 $\mu\text{g}/\text{ml}$ amp was inoculated overnight at 37 $^{\circ}\text{C}$ by constant shaking (180 rpm, New Brunswick Scientific) with one clone isolated during dilution plating. Afterwards, the plasmid was purified out of the overnight culture using the Nucleo Spin Plasmid Mini Prep Kit (# 740588.10, Macherey-Nagel) following the manufacturing protocol. The concentration of the plasmid was defined using the Lambert-Beer law (described in section 4.2.1.2).

For the streptavidin production, the obtained pTSA-13 plasmid was transformed into BL21(DE3) (# CMC0015, Sigma Aldrich) cells. Therefore, 40 μL cell suspension were completely thawed on ice (15 min) and mixed with about 1.8 μg of pTSA-13 plasmid DNA. Afterwards the cells were heat shocked for 45 sec at 42 $^{\circ}\text{C}$ and again incubated on ice for 5 min. For cell recovery, the cell DNA solutions was resuspended in 300 μL Expression Recovery Medium for 1 h at 37 $^{\circ}\text{C}$ and 150 rpm (Eppendorf), before plating the cells on a NZA agar plate containing 100 $\mu\text{g}/\text{ml}$ amp und 30 $\mu\text{g}/\text{ml}$ chloramphenicol (cam) overnight at 37 $^{\circ}\text{C}$.

Successful transformed clones were picked and incubated in 100 ml NZA media (+ amp, + cam) overnight at 37 °C and at 180 rpm (New Brunswick Scientific). Out of the overnight suspension a glycerol stock was produced. Therefore, the cell suspension was mixed in a 1:1 ratio with 50% sterile glycerol in a cryotube and stored at -80 °C till further processing.

From this glycerol stock, a preculture was incubated in 50 ml NZA- media (+ amp, + cam) overnight at 37 °C and 180 rpm (New Brunswick Scientific). The next day, 1 l main culture was inoculated with the preculture in a 1:40 ratio and incubated for 2 h at 37 °C to reach a OD₆₀₀ of about 0.8. At OD₆₀₀ 0.8 the protein expression was induced by adding 0.5 mM IPTG to the cell suspension and the cell culture was incubated overnight at 37 °C by 180 rpm (New Brunswick Scientific). After the incubation time, the culture was centrifuged at 5,000 rcf for 20 min at 4 °C (JLA 91000, Beckman Coulter). The supernatant was discarded and the pelleted cells resuspended in 25 ml Tris-A buffer before centrifuging at 20,000 rcf for 30 min at 4 °C (JA 25.50, Beckman Coulter). The supernatant again was discarded, the sediment slightly scraped from the vessel wall and then resuspended in 15 ml pre-chilled Tris-B buffer resuspended by constant stirring on a magnetic stirrer. Afterwards the cells in the suspension were disrupted in 5 cycles by means of a pre-cooled cell press (1200 bar, Thermo Fisher Scientific). The lysate was centrifuged by 21,100 rcf for 30 min at 4 °C (FA-45-16-17, Eppendorf) and the remaining inclusion bodies (IBs) stored at -20 °C for further processing.

For the purification process of the protein, the IBs were thawed on ice and washed in three different buffers including a centrifugation step in between (20,100 rcf, 30 min, 4°C, 5424 R, Eppendorf). The first purification step was done in 20 ml Tris-B buffer containing 2% TritonX, the second in 20 ml Tris- B buffer containing 1 M NaCl and the last step in 20 ml Tris-B buffer. During the last purification step the supernatant was discarded carefully and the remaining IBs were stored at -20 °C.

The IBs were then thawed on ice and resuspended in freshly prepared 6 M guanidine HCl, pH 1.5 (8 ml) for 1 h at 4°C during continuous stirring on a magnetic stirrer. Afterwards the solution was filtrated by means of a dialysis tube, SpectraPor, MWCO: 6-8 kDa (Thermo Fisher Scientific) overnight at 4 °C in 300 ml 6 M guanidine HCl, pH 1.5. The insoluble residues were separated by centrifugation (20,100 rcf, 20 min, 4 °C, 5430 R, Eppendorf). Subsequently, the pellet was discarded. For proper refolding of the protein, the solution was carefully and slowly pipetted in drops (to ensure complete suspension) into a stirred 500 ml, pre-chilled, 1x PBS pH 7.4 buffer. Afterwards the

solution was incubated overnight at 4 °C without stirring. To separate the protein aggregates from the correctly folded protein, the solution was centrifuged (20,000 rcf, 30 min, 4 °C, JA 25.50, Beckman Coulter). To induce protein precipitation, $(\text{NH}_4)_2\text{SO}_4$ was added to the supernatant to reach a saturation of 40% (Note! The $(\text{NH}_4)_2\text{SO}_4$ salt has to be finely mortared before use) and the mixture was inoculated for 4 h at 4 °C. During this step, monomeric streptavidin and impure protein should isolate from the solution. Afterwards, the protein solution was centrifuged (20,100 rcf, 20 min, 4 °C, Sorvall) and the supernatant mixed with a suitable amount of $(\text{NH}_4)_2\text{SO}_4$ to reach a final salt concentration of 70% while stirring at 4 °C overnight.

In the final step, the solution (containing the protein precipitate) was centrifuged at 20,100 rcf for 20 min at 4 °C. The supernatant was discarded and the protein pellet resuspended in 2 ml 1x PBS with addition of 2.2 M $(\text{NH}_4)_2\text{SO}_4$ to ensure the complete separation of protein impurities. Afterwards the solution was centrifuged (20,100 rcf for 20 min at 4 °C, Sorvall) and the protein resuspended in 1 ml 1x PBS. Insoluble protein aggregates were separated by filtration with a 0.45 μm filter device (VWR).

The samples were analyzed finally by SDS PAGE and Western Blotting (see section 4.2.5.1) and quantified at 270 nm using the Lambert-Beer law (see section 4.2.1.2).

4.2.2.2 Characterization of correct G-quadruplex formation using fluorescence resonance energy transfer (FRET)

During this study, the binding affinity of the thrombin protein to different defined origami systems was investigated (section 4.2.1.1.). To ensure correct formation of the embedded G4-aptamers TBA1 and TBA2, used in this study, a two-colors analysis using FRET was performed. Therefore, the two G-quadruplexes were labeled with two fluorophores (FAM and TAMRA, as shown in figure 4-9). The change in FRET efficiency between the donor-acceptor and the donor-only samples proved correct formation of the G4-structure. As an additional control the fully complement to the aptamer sequence was added, resulting in opening of the structure in concomitance with a lower FRET signal.

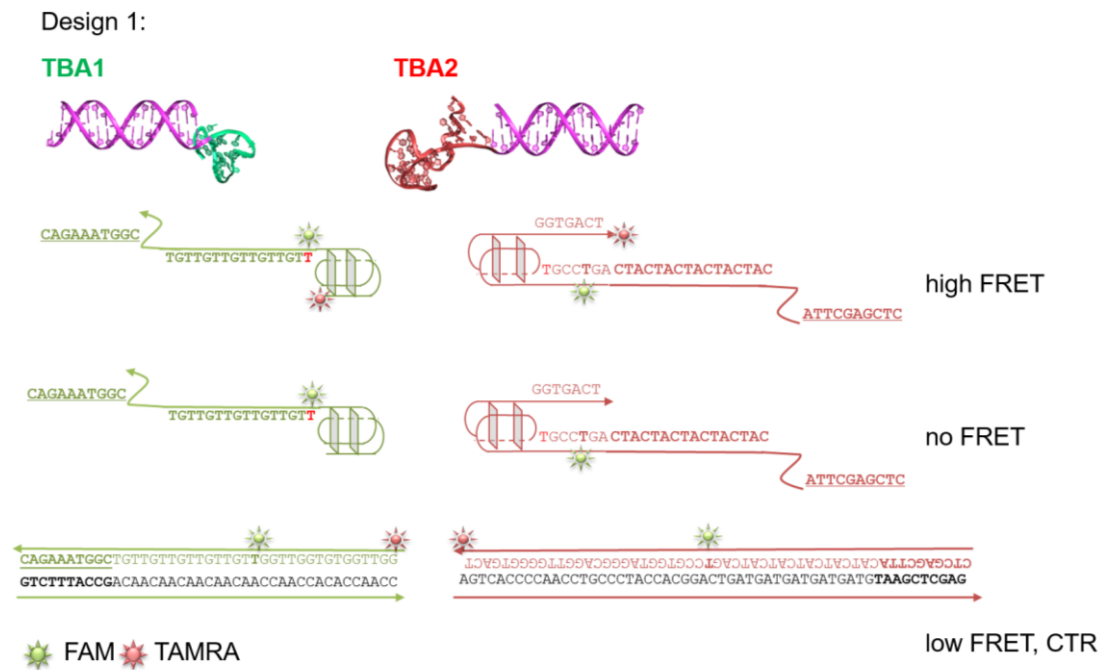


Figure 4-9: Schematic representation of the aptamer modification for analysis of correct G-quadruplex formation using FRET spectroscopy for design D1. Therefore, the two aptamers were labeled within the sequence with a FAM (middle of the sequence) and a TAMRA fluorophore at the 5'-terminus (TBA1; green), at the 3'-terminus (TBA2, red), respectively, ensuring a high FRET efficiency in concomitance with correct G4- formation (high FRET samples). The modification of the aptamers marked with just a FAM label and the addition of the fully complement of the G4-motif served as control showing no or low FRET efficiency (no FRET, low FRET CTR).

In our experiments, 2.5 μ l of 10 μ M aptamer stock solution in 5 μ l TEMg 1x was incubated with the DNA origami sample bearing the protruding arms within its inner cavity and annealed from 40-20 $^{\circ}$ C (1 $^{\circ}$ C/min). The products were afterwards analyzed by non-denaturing PAGE (4.2.5.1).

4.2.2.3 Protein labeling

To characterize protein encapsulation by gel electrophoresis analysis (see section 4.2.5.1), the thrombin protein (# 13188, Cayman Chemical Company) was labeled with different dyes in the NHS-ester form, in order to covalently bind them to amino groups, mostly accessible in the lysine side chains of the protein. The total amount of lysine's residues of the thrombin protein is 19. Theoretically, this should be sufficient for successful labeling. Therefore, in this study a cyanine 3 (Cy3, # 21020, Lumiprobe GmbH), cyanine 5 (Cy5, # 23020, Lumiprobe GmbH) and a fluorescein isothiocyanate (FITC, # 46410, Thermo Fisher Scientific) were used as dye labels. All labels were dissolved

in a suitable amount of DMSO to reach a final concentration of 20 mM under argon atmosphere. For efficient labeling, the protein should have a conc. of at least 40 μM . Therefore, before suspending the protein with the dye labels, the protein was concentrated using 3 kDa centrifugal filters (10,000 rcf, 4°C, 50 min, 5424 R, Eppendorf). Afterwards, about 100 to 150 μL of the protein were mixed with 57-equivalent excess (3 eq. x 19 lysine) of the different dye label and incubated for 2 h at room temperature in a shaker (Eppendorf). To remove the high excess of fluorescence dye, fluorescence dye removal columns from Thermo Fisher Scientific were used, according to the manufacturer protocol (# 22858). The characterization of the fluorescently labeled protein was done by SDS PAGE (see section 4.2.5.1) and the concentration was determined spectroscopically using the Lambert-Beer law (see section 4.2.1.2).

4.2.2.4 Functionalization and loading of the DNA origami host with thrombin or other proteins

As already stated above (4.2.1.1) four staple strands out of the original design and placed at opposite sides of the cavity (see figure 4-7, in grey) were replaced by extended protruding arms pointing towards the center of the inner cavity in order to hybridize with two complementary aptamer sequences selectively binding to thrombin. Therefore, the protruding arms and aptamer sequences (both in a 1.2-equimolar excess to the amount of the protruding arms) were added during the assembly process of the DNA origami host (4.2.1.3) to ensure formation of the desired structure. Protein loading into the host's cavity was achieved by adding the protein in a 5-equimolar excess to the total amount of aptamer catching sequences and incubating the solution at room temperature for 1 h before purification (see section 4.2.1.4). All procedures were performed in 1x TEMg buffer. The samples were characterized by gel electrophoresis (4.2.5.1) and AFM analysis (4.2.5.2).

4.2.3 Enzyme studies

Enzymatic assays were performed to investigate the effect of the DNA cage on the proteolytic activity of the encapsulated thrombin and compared to the same mixture of freely diffusing components. The kinetic evaluations were performed using the multi-mode microplate reader Spark® 10M (Tecan Group). The activity of the protease was measured by means of a FRET-substrate (FAM-GG-DPhe-PR SGGG-Lys(BHQ-1)-K-OH) and a substrate containing only the donor molecule as control (FAM-GG-DPhe-

PRSGGGKK-OH). The peptide sequence was designed with the help of the online platform MEROPS (peptide database, release 11.0) and purchased from company Intavis Bioanalytical Instruments AG. The substrates were dissolved in DMSO (2 mM). For the kinetic measurements, a suitable amount of each origami design (D1-D3, containing or lacking the aptamer arms and with scaffold concentration of 40 nM) was assembled following the protocol stated above (4.2.1.3, 4.2.2.2), purified and concentrated to a third of the initial assembly volume using PEG purification (4.2.1.4). After that 10 μ l of the origami structures (100 nM, calculated by qRT-PCR section 4.2.1.5) were incubated with 40 μ l of a 30 nM thrombin solution (# 13188, Cayman Chemical Company) and incubated for 1 h at 37°C in a 96-well plate (black flat bottom, Corning). At the end of the incubation time, 50 μ l of substrate in different concentrations (0, 5, 7.5, 10, 15, 20, 25, 30, 35, 40 & 50 μ M) were added to the mixture and the extent of substrate degradation was monitored *versus* time (ensuring synchronization of all origami/protein solutions). As control samples, the same amount of thrombin was treated with the same concentration of freely diffusing aptamers in solution (100 nM, either TBA1 or TBA2 alone or both simultaneously) and the kinetics was monitored following the same protocol.

The increase in the FAM emission signal was monitored over time. To be mentioned is that the increasing FAM signal during the measurement correlates to the amount of cleaved substrate molecules and therefore to the enzyme activity. With the help of the control substrate (containing only the FAM fluorophore) one can generate a standard curve to calculate the final FRET substrate concentration and thus, define the rate of the enzymatic reaction by means of the initial linear increase of the FAM signal during substrate degradation. Out of that initial reaction rate one can then extract the Michaelis Menten kinetic parameters (eq. [4-4] - eq. [4-5]):

$$v_0 = \frac{v_{max} \cdot [S]}{K_m + [S]}$$

Eq. [4-4]

$$v_{max} = k_{cat} \cdot E_0$$

Eq. [4-5]

with:

v_0 : initial reaction rate

V_{\max} : maximal reaction rate

S: substrate concentration

K_m : Michaelis Menten constant, defining the substrate concentration where the reaction rate is half v_{\max}

k_{cat} : turnover number, defining the highest substrate concentration converted to the final product per enzyme per second

E_0 : initial enzyme concentration

All final experiments were performed using 1x TEMg as running buffer. All further running parameters are listed in table 4-4. In total three independent runs, each in triplicates, were performed for all samples and the kinetic parameters were calculated applying a nonlinear Michaelis Menten enzyme kinetic fit provided by GraphPad Prism 5 v5.04.

Table 4-4: Running parameters used during the enzyme kinetic measurements.

Parameter	Setting
Application	SparkControl
Shaking (Double Orbital) Duration	30
Shaking (Double Orbital) Position	Current
Shaking (Double Orbital) Amplitude	1.5
Shaking (Double Orbital) Frequency	180
Mode	Kinetic
Kinetic cycles	40
Interval time	00:02:00 (hh:mm:ss)
Mode	Fluorescence Top Reading
Excitation	Monochromator
Excitation wavelength	482
Excitation bandwidth	20
Emission	Monochromator

Emission wavelength	527
Emission bandwidth	20
Gain	42
Mirror	AUTOMATIC
Number of flashes	30
Integration time	40
Lag time	0
Settle time	0
Z-Position	18455
Z-Position mode	Manual

4.2.4 Characterization of the molecular forces applied by a collection of tethered hairpin motifs

4.2.4.1 Temperature-dependent FRET spectroscopy

Thermal stability of the different constructs (0, I, II and III) presented in section 4.2.1.1 in the closed and in the open state were analyzed by temperature-dependent FRET spectroscopy. The experiments were performed using the CFX96 real time system (BioRad). 20 μ l of each DNA origami sample was imaged following the FAM emission intensity during the assembly and melting process (temperature range from 20-90 °C at a gradient of ± 0.1 °C/min) using 50 nM m13mp18 viral DNA, 250 nM staples and 100 nM of fluorophore modified seam sequences at different positions within the construct in 1X TEMg buffer. The same analysis was applied for the open state of the structure, upon addition of a 1.5 equimolar excess of fuel strands. A schematical summary of the experimental set up is given in figure 4-10. The two FRET reporters, here a FAM and a TAMRA fluorophore, were placed adjacent to the motifs to visualize their change in FRET efficiency during the assembly and melting process and to associate this solely to correct formation and integration of the hairpins into the origami frame. By altering the positions of the reporters and the amount of the integrated hairpin loops along the seam, the variation in the thermal stabilities measured provided information

about the forces and energies employed during the structural reconfiguration of the device.

Assuming that the cooling and the melting of the different designs is a two-state process, the folded fraction of the structure (θ) is directly proportional to the normalized FRET efficiency and can be related to the equilibrium constant reaction. From here the thermodynamic parameters of the process can be extracted by plotting $\ln(k_{eq})$ vs. the reciprocal temperature and calculating the enthalpy and entropy change of the process, respectively, from the slope and intercept of the curve in a restricted interval near the melting temperature (Van 't Hoff analysis, eq. [4-6] - eq. [4-10]):

$$E = 1 - \frac{DA}{D} \quad \text{Eq. [4-6]}$$

$$K_{eq} = \frac{[F]}{[U]} = \frac{\theta}{1 - \theta} \quad \text{Eq. [4-7]}$$

$$\Delta G = \Delta H - T\Delta S \quad \text{Eq. [4-8]}$$

$$K_{eq} = e^{\frac{-\Delta G}{RT}} = e^{\left(\frac{-\Delta H}{RT} + \frac{\Delta S}{R}\right)} \quad \text{Eq. [4-9]}$$

$$\ln K_{eq} = \frac{-\Delta H}{R} \cdot \frac{1}{T} + \frac{\Delta S}{R} \quad \text{Eq. [4-10]}$$

with:

E: FRET efficiency

DA: FAM fluorescence emission intensity of the sample containing the donor and acceptor molecule

D: FAM fluorescence emission intensity of the sample containing only the donor molecule

K_{eq} : equilibrium constant

- F: folded structures
 U: unfolded structures
 θ : folded fraction of the structures
 ΔG : change in Gibbs free energy
 ΔH : change in free enthalpy
 ΔS : change in entropy
 T: temperature
 R: ideal gas constant

From these data, the thermal stabilities of all constructs in the closed and open state were evaluated and the thermodynamic parameters of the conformational transition extrapolated (ΔG_{trans}). In total three independent runs were performed, each repeated four times for each sample and construct.

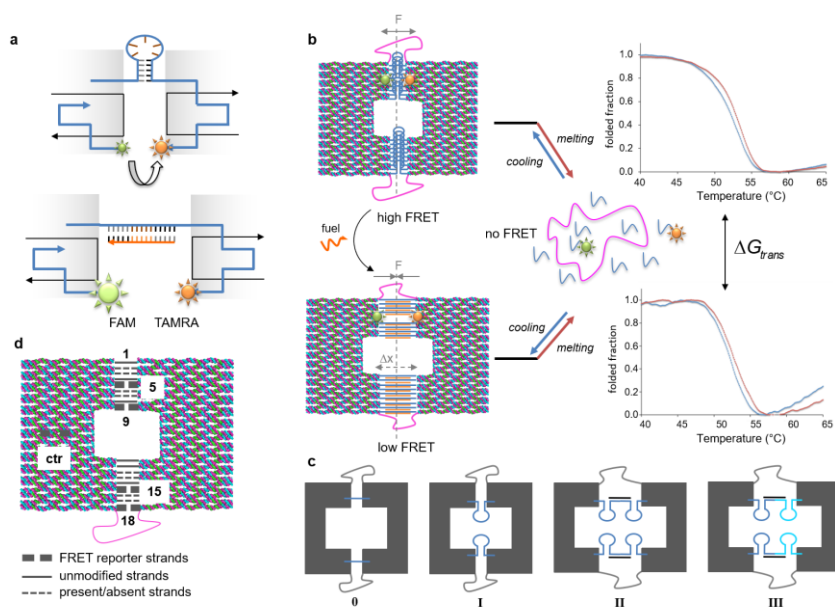


Figure 4-10: Experimental set up of the FRET-thermal analysis. (a) The two fluorophore pairs were integrated adjacent to the motor motifs to monitor the change in FRET efficiency during the thermal denaturation/assembly process. The design was selected in a way that free moving units in solution don't influence the outcome of the evaluation. Only correct integrated features enable to visualize the change in FRET intensity. (b) By comparing the results of the different device states, the thermodynamic parameters related to the conformational transition (ΔG_{trans}) can be estimated. (c) In total 4 distinct constructs were evaluated. Construct 0 with no hairpin loops integrated, I with one loop, II with two identical loops in series and III with two different hairpins in series. (d) Altering the positions of the reporters (indicated by the black numbers) and the amount of the integrated hairpin loops (dashed lines), the variation in thermal stability enables to provide information about the employed forces/energies and their dependence on the structural environment and the geometric arrangement of the constituent motor units.

4.2.4.2 Tug-of-war experiments

An interesting application of the reconfigurable origami system described in this work was realized by placing a delicate nanoarchitecture inside its inner cavity and using the forces generated by fuel/antifuel addition to unfold and refold this architecture, as presented in figure 4-11.

FRET spectroscopy was used for the investigation of this system. Two 21 bases arms (TGG₇ left and TTG₇ right; grey) were integrated into the DNA origami frame such to point towards the inner cavity. The assumed free space of 5 nm was filled with a G-quadruplex structure formed by two sequences (CCA)₇G₄T₄G₄ and (CAA)₇G₄T₄G₄ (green and orange), marked with a FRET reporter pair and partly complementary to the protruding arms (grey) anchored to the origami walls. In the closed state, the device was associated to a high FRET efficiency, while in the open state a lower FRET efficiency was observed.

The analysis was performed with 50 nM construct I (5-equimolar excess unlabeled staple strands, 2-equimolar excess dye-labeled staple strands), purified by PEG, following the protocols described in section 4.2.1.3 and 4.2.1.4. The FAM emission signal was monitored using the CFX96 real time system (BioRad). 20 µl of the DNA origami sample was imaged at a constant temperature of 40 °C for 20 h every 5 min upon addition of 1.2-equimolar amounts of fuel strands and 20 h every 5 min after adding 5 equimolar excess of antifuel strands.

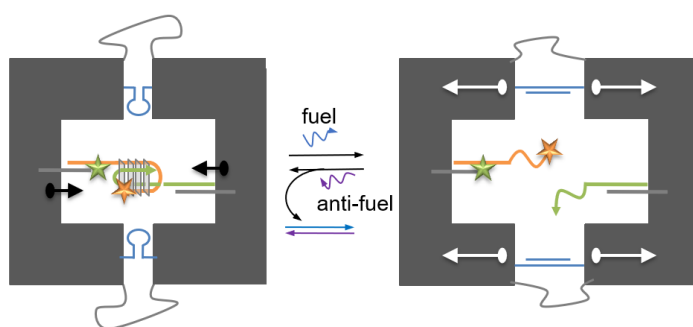


Figure 4-11: Illustration of the tug-of-war experiment using the origami design of construct I. Planned was the mechanical unfolding/refolding of a G-quadruplex motif linked to the inner walls of the cavity. The investigation was performed using FRET spectroscopy. The mechanical transition was monitored upon fuel/antifuel addition following the change in the FAM emission intensity.

4.2.4.3 Temperature-dependent UV spectroscopy

The temperature-dependent FRET spectroscopy experiments presented in section 4.2.4.1 represent the thermal stabilities of fluorescently labeled hairpins embedded within distinct geometric environments. By means of temperature-dependent UV spectroscopy the global thermal stability of the structure can be evaluated and compared with the results gained by the FRET-thermal analysis. The thermal denaturation/assembly process of one exemplary construct was used (construct I). 40 μ L of the origami sample were placed in a quartz UV microcuvette (# 6610024200, Agilent Technologies, 40 μ L, 1 cm). The sample contained the two fluorophore pairs at position 5 of the seam (2.5 nM scaffold, 12 nM staple strands and 5 nM dye modified strands) and its thermal denaturation/renaturation was analyzed monitoring the absorbance at 260 nm during a temperature gradient from 80 °C to 20 °C, at a rate of 0.1 °C/min, by means of an UV-Vis spectrophotometer (Cary 300 BIO UV-Visible Spectrophotometer, Varian Inc.). Three independent runs were performed and the fit of the averaged curve was calculated applying a sigmoidal Boltzmann equation provided by the GraphPad Prism software.

4.2.5 Imaging analysis

4.2.5.1 Gel electrophoresis analysis

All construct presented in this thesis in the sections above (4.2.1.1, 4.2.1.3, 4.2.2.1, 4.2.2.3, 4.2.2.2, 4.2.2.3, 4.2.4.1) were characterized – among other techniques – by ensemble gel electrophoresis.

Agarose gel electrophoresis

Agarose gel electrophoresis was performed using 0.75% agarose (# 840004, Biozym) in 1x TBEMg. The gels were run at 80 V for 2 h at 4 °C. Scanning of the gels was performed with a Typhoon FLA 9000 (GE Healthcare Life Sciences) scanner at different wavelengths to visualize distinct fluorescence moieties within the constructs and finally stained with ethidium bromide (# 111615, Merck).

Non-denaturing PAGE (polyacrylamide gel electrophoresis)

To prove the correct formation of G-quadruplex structures, non-denaturing PAGE was used (25% acrylamide/bis solution; 19:1; 40% w/v, Sigma Aldrich, in 1x TBEMg buffer). The gels were run at 80 V for approximately 2 h at 4 °C. Gels were first examined by

Typhoon FLA 9000 (GE Healthcare Life Sciences) scanner and then stained with SYBR Gold Nucleic Acid Gel Stain (Thermo Fisher Scientific).

Sodium dodecyl sulfate (SDS) PAGE

All proteins produced in this study were analyzed by SDS PAGE. For this purpose acrylamide/bis solution (37.5:1; 30% w/v, Sigma Aldrich) was used. 4x SDS loading dye was added to the distinct samples and the solutions denatured for 10 min at 90 °C before gel loading. The resolving gel (12%) was cast using SDS resolving gel buffer (4x) and the stacking gel (6%) with SDS stacking gel buffer (4x). The gels were run in 1x SDS running buffer at 120 V for approximately 1 h. The labeled thrombin was visualized by Typhoon FLA 9000 (GE Healthcare Life Sciences) scanner before Coomassie staining (streptavidin was only stained with Coomassie). Therefore, the gels were placed into buffer CA for 30 s and heated in a microwave by 400 W before shaking them at room temperature for 5 min. Afterwards the gels were heated for 30 s each in buffer CB and CC (450 W) and here after destained for 1 h in buffer CD. Imaging of the Coomassie stained gels was performed using a gel documentation device (Intas).

Western Blotting

During the runtime of the SDS gel the western blot membrane (# T831.1, Roth) was activated in MeOH for some minutes, washed in H₂O and equilibrated in 1x transfer buffer for 10 min. Meanwhile, pads and Whatman paper were equilibrated in 1x transfer buffer for 15 min. The unstained streptavidin gel was washed in 1x transfer buffer for 15 min after the gel run. The gel was blotted and pressed with a falcon tube to remove possible air bubbles trapped in between. The blot was run in a wet blotting device for 60 min at 110 V. For blocking of the membrane and antibody incubation the membrane was transferred into a 50 ml falcon tube, the top side of the membrane facing the inner side of the tube, and 10 ml blocking solution were added for 1 h at room temperature. The antibody solution (1:25,000; in blocking solution, streptavidin-peroxidase, # S2438, Sigma) was added into the falcon tube and incubated overnight at 4 °C. After that the membrane was washed in 10 ml 1x TBST three times and the gel imaged using the gel documentations system Amersham Imager 600 QC (GE Healthcare Life Sciences).

4.2.5.2 Atomic force microscopy (AFM) imaging and data analysis

All different origami devices described in section 4.2.1.1 and 4.2.4.1 were analyzed by AFM. The samples were deposited on a freshly cleaved mica surface (Plano GmbH) and incubated for at least 2 min at room temperature. Scanning of the sample was performed on a MultiModeTM 8 microscope (Bruker) equipped with a Nanoscope V controller, using the ScanAsyst[®] PeakForce TappingTM working mode. ScanAsyst Fluid+ tips (Bruker) with a 0.7 N/m spring constant were used in 1x TAEMg buffer. Origami structures modified with biotinylated staple strands, used as topographical marker (see section 4.2.2) were further treated with 10 μ l of a freshly prepared 1 μ M streptavidin solution and incubated for 3 min at room temperature. All images were analyzed by the NanoScope 6.14 software provided by Bruker. For statistical significance of the data, several AFM images were taken from various positions on the mica surface.

4.2.6 Molecular dynamics simulations and atomistic models

The interaction between the DNA origami and thrombin was simulated considering only the protruding arms of the origami. Initial coordinates for the protruding arms were obtained using the sequence of the arms and a canonical B structure for the DNA double helix. Later the structure of the regions covering the TBA1 and TBA2 aptamer sequences were modified in order to match the structure in 4I7Y [142] and 4DIH [143] respectively. After this, the residues in the protruding arms binding to the origami were placed 22 nm apart with the aptamer regions pointing to each other. In this way, the DNA origami design is reproduced, see figure 4-12. Coordinates for thrombin were taken from the structure in 1PPB [144].

Four different designs for the protruding arms were simulated, see figure 4-12. For designs 3 and 2 simultaneous binding of TBA1 and TBA2 to thrombin was considered. For design 1 binding of one thrombin to TBA2 or two thrombin proteins binding to TBA1 and TBA2 simultaneously were considered while for design 0 only the binding to TBA2 was considered. In total 5 different binding possibilities were explored, see figure 4-12.

The MD simulations were performed in the NPT ensemble using the CHARMM36 [145] force field and the NAMD2.12 [146] program. All systems were solvated using the TIP3P [147] water model with a minimum distance to the walls of the simulation box of

15 Å in the X-axis and 20 Å in the Y and Z-axis. All systems were neutralized and then 12.5 mM of MgCl₂ were added to match the experimental concentration of MgCl₂ used in the experiments. The residues directly bound to the origami scaffold in the protruding arms were kept fixed during the MD runs to simulate the attachment of the arms to the origami. No other restrains were used. Analysis performed by the Sánchez-García Group, by Dr. Kenny Bravo-Rodriguez.

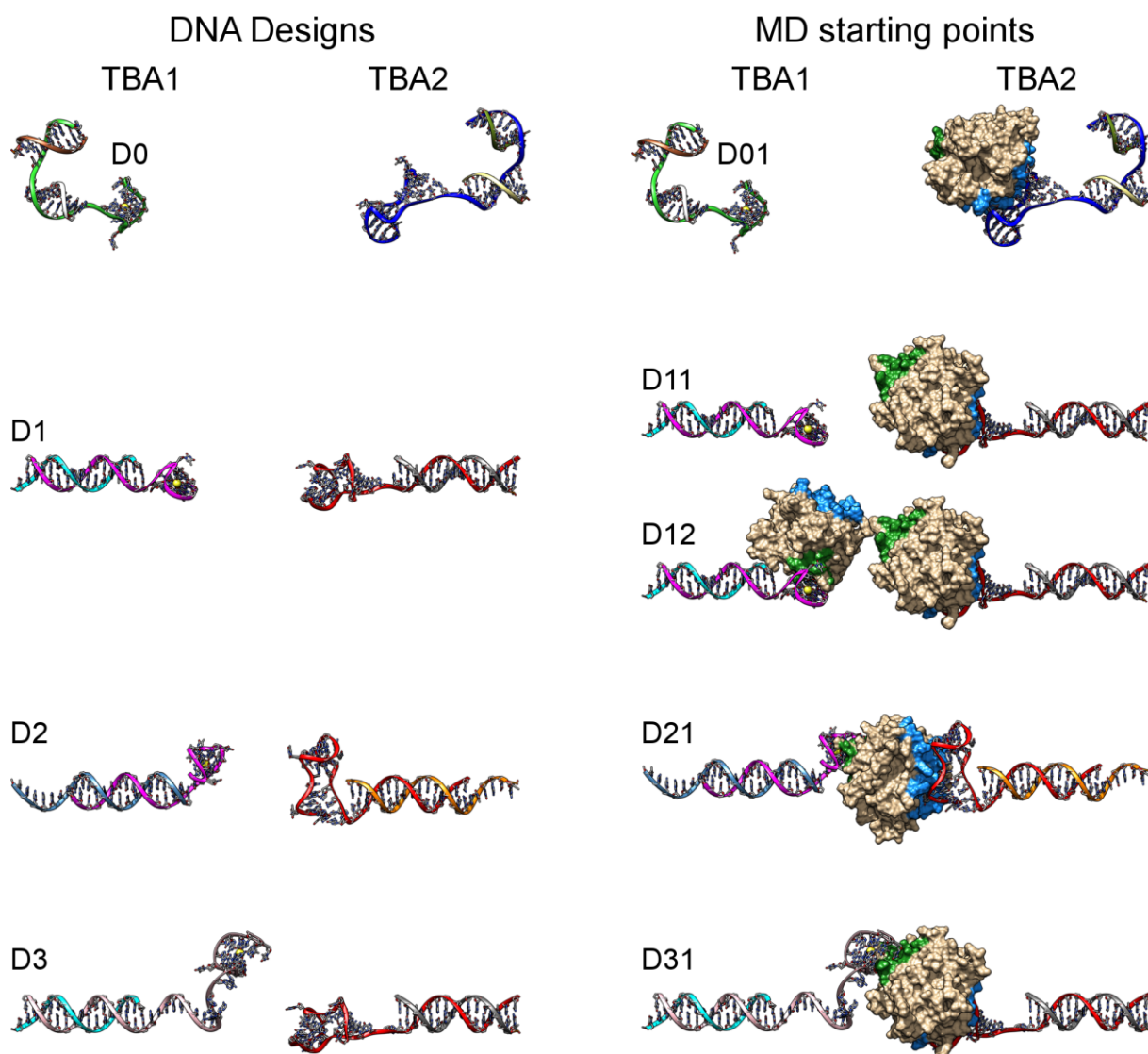


Figure 4-12: Starting setup for the five MD simulations performed. (Left) Four designs were considered here for the protruding arms. (Right) The starting points for the MD simulations. DNA strands with the same sequence are shown with the same color. Thrombin is shown with a surface representation where the blue color represents the exosite II and the green color the exosite I. The names for the MD simulations setup represent the arms design and the number of thrombin proteins present in the simulation. Analysis performed by the Sánchez-García Group, by Dr. Kenny Bravo-Rodriguez.

4.2.7 Software

Autodesk MAYA

The MAYA software developed by the Autodesk company has been used as graphical support for rendering of the DNA origami structures. Therefore, the Cadnano software (see below) was integrated as a plugin for Autodesk's MAYA software. For this thesis, a student version of Autodesk MAYA 2015 SP2 was used.

Cadnano

DNA origami design was developed using the software Cadnano (Wyss Institute for Biological Inspired Engineering, Harvard University). The DNA-origami constructs were designed using a square lattice pattern. For this thesis, the Cadnano version 2.2.0 was used as a plug-in in the Autodesk 2015 MAYA software and can be obtained free of charge at <http://cadnano.org>.

CanDo

This software is a free online platform developed by the Laboratory for Computational Biology & Biophysics at the Massachusetts Institute of Technology. It provides geometric models of a DNA-origami structure of interest. The calculations are based on a mechanical model of the DNA, assuming DNA to be an elastic rod, with distinct axial, twisting and bending stimuli, as described by Maher and coworkers (<http://cando-dna-origami.org>) [115].

CFX Manager

In this study, the FAM emission spectra obtained during the temperature-dependent FRET experiments (including isothermal analysis) were programmed and characterized by the CFX Manager™ 3.0 (BioRad) software.

DNASTAR Lasergene 12/ SeqMan Pro

The sequence results obtained by the Sanger Sequencing service of the GATC company were analyzed with the DNASTAR Lasergene 12/ SeqMan Pro Version 12.2.0(82), 421 software.

GraphPad Prism

All AFM data are expressed as mean \pm standard error of the mean (SEM) and rely on at least triplicate experiments (section 4.2.5.2). Statistical analysis was performed using GraphPad Prism 5 version 5.04 software.

ImageJ

ImageJ is an image-processing program developed at the National Institute of Health. It was used for agarose gel electrophoresis image analysis and quantification (section 4.2.5.1). ImageJ version 1.47v was used with Java 1.6.0_65 (<http://imagej.nih.gov/ij>).

Mfold software tool/ DINAMelt software

For the energy evaluations according to the nearest-neighbor model (section 4.2.4.1) Mfold and DINAMelt tool software was used. The parameters were set to 50 nM strand concentration at 25°C in presence of 4 mM sodium and 10.5 mM magnesium ion concentration (<http://unafold.rna.albany.edu/?q=mfold/download-mfold>; <http://unafold.rna.albany.edu/?q=dinamelt>).

Nanoscope & Nanoscope Analysis

For AFM imaging and data analysis (section 4.2.5.2) the built-in software tool provided by Bruker were used (Nanoscope 8.15 and Nanoscope analysis 1.50).

NUPACK

NUPACK is an online tool to analyze and design DNA structures. This was used for designing and analyzing the hairpins inserted in construct III (section 4.2.1.1; <http://www.nupack.org/>).

5 Conclusions and Outlook

In this study, it was possible to develop a user-defined and reconfigurable planar DNA origami system, which can be actuated in a trigger dependent manner. Using this platform, it was demonstrated that the organized tethering of small switchable molecular motors, aligned along the same direction within a DNA nanostructure, can be employed to trigger a global translational movement that alters the energy landscape of the internalized motifs. This energetic change can be interpreted by a hybrid spring model, which includes the thermodynamic base-pairing term (derived from the nearest-neighbor model) and the elastic contribution estimated by the worm-like-chain (WLC) approximation. Rigid scaffolding of such motifs, when compared to the same motifs freely diffusing in solution, enhances their thermal stability and mechanical performance of a three-fold factor, enabling to mechanically unfold a defined architecture linked inside the inner cavity of the device. Despite the anisotropic thermal behavior of the structures and the intrinsic flexibility of the hairpin motifs, this system can be similarly employed into more rigid nanodevices to perform more sophisticated operations. Moreover, the programmability of the size of the inner cavity can be advantageously used to catch molecules of interest in a size selected fashion and with a desired orientation. It could be shown that binding of the serine protease thrombin by two G4-motifs is increased by its confinement within the DNA nanostructure, possibly affecting also the thermodynamic and kinetic function of the protein. This demonstrates that DNA nanotechnology can be used to manipulate enzymatic reactions and in general to develop new biomaterials with user defined properties. In conclusion, this work emphasizes the importance of tight fastening, compactness and organized distribution of switchable motifs in the design of DNA nanomechanical devices, where the synchronized and coordinated action of multiple motors can be used to apply higher forces and actuate large-scale transformations otherwise impossible to achieve in a random state.

6 Summary

Dynamic DNA nanotechnology offers an innovative opportunity to build up biomimetic nanostructures with increasing complexity and precision, depending on the overall spatial and temporal control of matter distribution with nanometer accuracy and in a trigger dependent manner. Mechanically switchable hairpin motifs thereby offer the possibility to perform DNA-induced conformational transitions. By means of temperature dependent FRET spectroscopy it was possible to explore the operational capabilities, energetics and mechanical performance of a distinct collective ensemble of hairpin motifs tethered to a large DNA origami framework with the result of a novel hybrid spring model to describe the energy landscape of the integrated switchable hairpins. Consequently, the thermodynamic nearest-neighbor energy of the duplex DNA with the entropic free energy of single-stranded DNA estimated using a worm-like chain approximation was combined. Understanding of how mechanical forces can be gathered and manipulated at the molecular level is fundamental for the development of more sophisticated nanodevices and may help to gain more insights into the performance of complex natural molecular machines.

Additionally, the strategic positioning of two G4-motifs (TBA1 and TBA2) within the inner cavity of the DNA frame demonstrated the possibility to form a 1:1 host-guest complex, without altering the natural properties of the encapsulated protein, thus emulating some of the fundamental properties of natural compartmentalization systems. The results demonstrated that the binding affinity and activity of the thrombin were greatly enhanced by caging it within the origami frame and that defined geometric arrangements of the internalized aptamer ligands can be used to develop a tool for selective encapsulation and manipulation of desired molecular cargos. In conclusion, this work shows the high potential of DNA nanotechnology to build up programmable, dynamical, bioinspired artificial nanovessels, which might be used for the storage and delivery of materials and desired protein targets at precise cellular locations.

7 Zusammenfassung

Dynamische DNA-Nanotechnologie repräsentiert eine innovative Methodik biomimetische Nanostrukturen mit zunehmender Komplexität und Präzision aufzubauen. Ein großer Vorteil bei der Verwendung dieser Technik liegt in der gesamten räumlich und zeitlich kontrollierbaren Steuerung der Systeme im Nanometerbereich. Die Konfigurierbarkeit der Strukturen wurde in dieser Arbeit über sogenannte DNA Haarnadelmotive gesteuert. Mit Hilfe von temperaturabhängiger Förster-Resonanzenergietransfer (FRET) Spektroskopie war es somit möglich, die mechanische Kapazität und die Energie integrierter Ensembles dieser DNA Motoren innerhalb eines DNA Origami Systems zu bestimmen. Das Ergebnis ist ein neuartiges Modell, welches die Energielandschaft der Haarnadelmotive beschreibt. Dafür wurde das *Nearest-Neighbor* Modell, welches die thermodynamische Energie des DNA-Duplexes in der offenen Haarnadelform beschreibt, mit der freien entropischen Energie der Einzelstrang DNA (geschlossene Form), die mittels des *Worm-like Chain* Algorithmus bestimmt wurde, miteinander kombiniert. Das gewonnene Verständnis über die Steuerung und Manipulation molekularer Kräfte ist essentiell und fundamental für die Entwicklung und Konstruktion anspruchsvollerer Nanomaschinen und gewährt zudem Einblick in die Funktionsweise komplexer molekularer Prozesse.

Weiterhin war es möglich, durch die Verwendung dieser Methodik, strategisch zwei spezifische DNA Aptamere (*TBA1* und *TBA2*) innerhalb eines DNA-Origami Rahmens zu integrieren, welches die Einkapselung der Serin Protease Thrombin ermöglichte. Die entwickelte Nanofabrik erlaubte somit die 1:1 *host-guest* Komplexierung ohne die natürlichen Eigenschaften des Proteins zu verändern, welches vergleichbar mit natürlichen Kompartiment Systemen ist. Die Ergebnisse der Analysen zeigten, dass die Bindungsaffinität der Aptamer Liganden zum Protein innerhalb des Origami Systems und die katalytische Aktivität von Thrombin stark erhöht werden konnten und dass die geometrische Integration der Liganden eine effektive Methodik für die selektive Komplexierung und Manipulation eines gewünschten und vorher ausgewählten Proteins darstellt. Zusammenfassend konnte in dieser Arbeit das hohe Potential der DNA Nanotechnologie für die Konstruktion programmierbarer, bioinspirierter und künstlicher Nanokompartimentsysteme bewiesen werden, die für die Speicherung und den Transport spezifischer Materialien/Proteine zu definierten Zielorten innerhalb der Zelle verwendet werden können.

8 References

1. Feynman, R.P., *There is plenty of room at the bottom*. Eng. Sci., 1960. **23**: p. 22–36.
2. Zhao, J., L.A. Swartz, W.F. Lin, P.S. Schlenoff, J. Frommer, J.B. Schlenoff and G.Y. Liu, *Three-Dimensional Nanoprinting via Scanning Probe Lithography-Delivered Layer-by-Layer Deposition*. ACS Nano, 2016. **10**(6): p. 5656-5662.
3. Yuan, L.L. and P.R. Herman, *Laser Scanning Holographic Lithography for Flexible 3D Fabrication of Multi-Scale Integrated Nano-structures and Optical Biosensors*. Sci Rep, 2016. **6**: p. 22294.
4. Pal, R.K., A.A. Farghaly, M.M. Collinson, S.C. Kundu and V.K. Yadavalli, *Photolithographic Micropatterning of Conducting Polymers on Flexible Silk Matrices*. Adv Mater, 2016. **28**(7): p. 1406-1412.
5. Watson, J.D. and F.H. Crick, *Genetical implications of the structure of deoxyribonucleic acid*. Nature, 1953. **171**(4361): p. 964-967.
6. Watson, J.D. and F.H. Crick, *Molecular structure of nucleic acids; a structure for deoxyribose nucleic acid*. Nature, 1953. **171**(4356): p. 737-738.
7. Saccà, B., A. Sprengel and U. Feldkamp, *De Novo Design of Nucleic Acid Structures*, in *De novo Molecular Design*. 2013, Wiley-VCH Verlag GmbH & Co. KGaA. p. 495-517.
8. Seeman, N.C., *Nucleic acid junctions and lattices*. J Theor Biol, 1982. **99**(2): p. 237-247.
9. Seeman, N.C. and N.R. Kallenbach, *DNA branched junctions*. Annu Rev Biophys Biomol Struct, 1994. **23**: p. 53-86.
10. Seeman, N.C. and N.R. Kallenbach, *Design of immobile nucleic acid junctions*. Biophys J, 1983. **44**(2): p. 201-209.
11. Fu, T.J. and N.C. Seeman, *DNA double-crossover molecules*. Biochemistry, 1993. **32**(13): p. 3211-3220.
12. Yan, H., S.H. Park, G. Finkelstein, J.H. Reif and T.H. LaBean, *DNA-templated self-assembly of protein arrays and highly conductive nanowires*. Science, 2003. **301**(5641): p. 1882-1884.
13. Zhang, T.H., C.; Fischer, S.; Frank, K.; Nickels, P.; Heuer- and A.N. Jungemann, B.; Liedl, T., *3 D DNA Origami Crystals*. arXiv.1706.06965v1, 2017.
14. Zheng, J., J.J. Birktoft, Y. Chen, T. Wang, R. Sha, P.E. Constantinou, . . . N.C. Seeman, *From molecular to macroscopic via the rational design of a self-assembled 3D DNA crystal*. Nature, 2009. **461**(7260): p. 74-77.
15. He, Y., Y. Chen, H. Liu, A.E. Ribbe and C. Mao, *Self-assembly of hexagonal DNA two-dimensional (2D) arrays*. J Am Chem Soc, 2005. **127**(35): p. 12202-12203.
16. Zhang, F., S. Jiang, W. Li, A. Hunt, Y. Liu and H. Yan, *Self-Assembly of Complex DNA Tessellations by Using Low-Symmetry Multi-arm DNA Tiles*. Angew Chem Int Ed Engl, 2016. **55**(31): p. 8860-8863.
17. He, Y., Y. Tian, A.E. Ribbe and C. Mao, *Antibody nanoarrays with a pitch of approximately 20 nanometers*. J Am Chem Soc, 2006. **128**(39): p. 12664-12665.
18. He, Y., Y. Tian, A.E. Ribbe and C. Mao, *Highly connected two-dimensional crystals of DNA six-point-stars*. J Am Chem Soc, 2006. **128**(50): p. 15978-15979.
19. Rothmund, P.W., *Folding DNA to create nanoscale shapes and patterns*. Nature, 2006. **440**(7082): p. 297-302.

20. Dietz, H., S.M. Douglas and W.M. Shih, *Folding DNA into twisted and curved nanoscale shapes*. Science, 2009. **325**(5941): p. 725-730.
21. Douglas, S.M., H. Dietz, T. Liedl, B. Hogberg, F. Graf and W.M. Shih, *Self-assembly of DNA into nanoscale three-dimensional shapes*. Nature, 2009. **459**(7245): p. 414-418.
22. Yan, H., T.H. LaBean, L. Feng and J.H. Reif, *Directed nucleation assembly of DNA tile complexes for barcode-patterned lattices*. Proc Natl Acad Sci U S A, 2003. **100**(14): p. 8103-8108.
23. Kuzuya, A. and M. Komiyama, *DNA origami: fold, stick, and beyond*. Nanoscale, 2010. **2**(3): p. 310-322.
24. Nangreave, J., D. Han, Y. Liu and H. Yan, *DNA origami: a history and current perspective*. Curr Opin Chem Biol, 2010. **14**(5): p. 608-615.
25. Topping, T., N.V. Voigt, J. Nangreave, H. Yan and K.V. Gothelf, *DNA origami: a quantum leap for self-assembly of complex structures*. Chem Soc Rev, 2011. **40**(12): p. 5636-5646.
26. Liu, H., Y. Chen, Y. He, A.E. Ribbe and C. Mao, *Approaching the limit: can one DNA oligonucleotide assemble into large nanostructures?* Angew Chem Int Ed Engl, 2006. **45**(12): p. 1942-1945.
27. Hansen, M.N., A.M. Zhang, A. Rangnekar, K.M. Bompiani, J.D. Carter, K.V. Gothelf and T.H. LaBean, *Weave tile architecture construction strategy for DNA nanotechnology*. J Am Chem Soc, 2010. **132**(41): p. 14481-14486.
28. Wei, B., M. Dai and P. Yin, *Complex shapes self-assembled from single-stranded DNA tiles*. Nature, 2012. **485**(7400): p. 623-626.
29. Ke, Y., G. Bellot, N.V. Voigt, E. Fradkov and W.M. Shih, *Two design strategies for enhancement of multilayer-DNA-origami folding: underwinding for specific intercalator rescue and staple-break positioning*. Chem Sci, 2012. **3**(8): p. 2587-2597.
30. Benson, E., A. Mohammed, J. Gardell, S. Masich, E. Czeizler, P. Orponen and B. Hogberg, *DNA rendering of polyhedral meshes at the nanoscale*. Nature, 2015. **523**(7561): p. 441-444.
31. Zhang, F., S. Jiang, S. Wu, Y. Li, C. Mao, Y. Liu and H. Yan, *Complex wireframe DNA origami nanostructures with multi-arm junction vertices*. Nat Nanotechnol, 2015. **10**(9): p. 779-784.
32. Shaw, A., V. Lundin, E. Petrova, F. Fodoros, E. Benson, A. Al-Amin, . . . A.I. Teixeira, *Spatial control of membrane receptor function using ligand nanocalipers*. Nat Methods, 2014. **11**(8): p. 841-846.
33. Zhao, Z., J. Fu, S. Dhakal, A. Johnson-Buck, M. Liu, T. Zhang, . . . H. Yan, *Nanocaged enzymes with enhanced catalytic activity and increased stability against protease digestion*. Nat Commun, 2016. **7**: p. 10619.
34. Ouyang, X., J. Li, H. Liu, B. Zhao, J. Yan, D. He, . . . J. Chao, *Self-assembly of DNA-based drug delivery nanocarriers with rolling circle amplification*. Methods, 2014. **67**(2): p. 198-204.
35. Praetorius, F. and H. Dietz, *Self-assembly of genetically encoded DNA-protein hybrid nanoscale shapes*. Science, 2017. **355**(6331).
36. Zhang, H. and P. Guo, *Single molecule photobleaching (SMPB) technology for counting of RNA, DNA, protein and other molecules in nanoparticles and biological complexes by TIRF instrumentation*. Methods, 2014. **67**(2): p. 169-176.

37. Birkedal, V., M. Dong, M.M. Golas, B. Sander, E.S. Andersen, K.V. Gothelf, . . . J. Kjems, *Single molecule microscopy methods for the study of DNA origami structures*. *Microsc Res Tech*, 2011. **74**(7): p. 688-698.
38. Ke, Y., L.L. Ong, W. Sun, J. Song, M. Dong, W.M. Shih and P. Yin, *DNA brick crystals with prescribed depths*. *Nat Chem*, 2014. **6**(11): p. 994-1002.
39. Acuna, G.P., F.M. Moller, P. Holzmeister, S. Beater, B. Lalkens and P. Tinnefeld, *Fluorescence enhancement at docking sites of DNA-directed self-assembled nanoantennas*. *Science*, 2012. **338**(6106): p. 506-510.
40. Pfeifer, W. and B. Sacca, *From Nano to Macro through Hierarchical Self-Assembly: The DNA Paradigm*. *Chembiochem*, 2016. **17**(12): p. 1063-1080.
41. Gerling, T., K.F. Wagenbauer, A.M. Neuner and H. Dietz, *Dynamic DNA devices and assemblies formed by shape-complementary, non-base pairing 3D components*. *Science*, 2015. **347**(6229): p. 1446-1452.
42. Pfeifer, W., P. Lill, C. Gatsogiannis and B. Sacca, *Hierarchical Assembly of DNA Filaments with Designer Elastic Properties*. *ACS Nano*, 2017.
43. Cheng, J., S. Sreelatha, I.Y. Loh, M. Liu and Z. Wang, *A bioinspired design principle for DNA nanomotors: mechanics-mediated symmetry breaking and experimental demonstration*. *Methods*, 2014. **67**(2): p. 227-233.
44. Sacca, B., Y. Ishitsuka, R. Meyer, A. Sprengel, E.C. Schoneweiss, G.U. Nienhaus and C.M. Niemeyer, *Reversible reconfiguration of DNA origami nanochambers monitored by single-molecule FRET*. *Angew Chem Int Ed Engl*, 2015. **54**(12): p. 3592-3597.
45. Baccouche, A., K. Montagne, A. Padirac, T. Fujii and Y. Rondelez, *Dynamic DNA-toolbox reaction circuits: a walkthrough*. *Methods*, 2014. **67**(2): p. 234-249.
46. Sacca, B. and C.M. Niemeyer, *Functionalization of DNA nanostructures with proteins*. *Chem Soc Rev*, 2011. **40**(12): p. 5910-5921.
47. Suzuki, Y., M. Endo, C. Canas, S. Ayora, J.C. Alonso, H. Sugiyama and K. Takeyasu, *Direct analysis of Holliday junction resolving enzyme in a DNA origami nanostructure*. *Nucleic Acids Res*, 2014. **42**(11): p. 7421-7428.
48. Suzuki, Y., M. Endo, Y. Katsuda, K. Ou, K. Hidaka and H. Sugiyama, *DNA origami based visualization system for studying site-specific recombination events*. *J Am Chem Soc*, 2014. **136**(1): p. 211-218.
49. Douglas, S.M., I. Bachelet and G.M. Church, *A logic-gated nanorobot for targeted transport of molecular payloads*. *Science*, 2012. **335**(6070): p. 831-834.
50. Kuchler, A., M. Yoshimoto, S. Luginbuhl, F. Mavelli and P. Walde, *Enzymatic reactions in confined environments*. *Nat Nanotechnol*, 2016. **11**(5): p. 409-420.
51. Chen, A.H. and P.A. Silver, *Designing biological compartmentalization*. *Trends Cell Biol*, 2012. **22**(12): p. 662-670.
52. Seeman, N.C., *Nanomaterials based on DNA*. *Annu Rev Biochem*, 2010. **79**: p. 65-87.
53. Crawford, R., C.M. Erben, J. Periz, L.M. Hall, T. Brown, A.J. Turberfield and A.N. Kapanidis, *Non-covalent single transcription factor encapsulation inside a DNA cage*. *Angew Chem Int Ed Engl*, 2013. **52**(8): p. 2284-2288.

54. Erben, C.M., R.P. Goodman and A.J. Turberfield, *Single-molecule protein encapsulation in a rigid DNA cage*. *Angew Chem Int Ed Engl*, 2006. **45**(44): p. 7414-7417.
55. Zhang, C., C. Tian, F. Guo, Z. Liu, W. Jiang and C. Mao, *DNA-directed three-dimensional protein organization*. *Angew Chem Int Ed Engl*, 2012. **51**(14): p. 3382-3385.
56. Zhao, Z., J. Fu, S. Dhakal, A. Johnson-Buck, M. Liu, T. Zhang, . . . H. Yan, *Nanocaged enzymes with enhanced catalytic activity and increased stability against protease digestion*. *Nat Commun*, 2016. **7**.
57. Rajendran, A., M. Endo and H. Sugiyama, *Single-molecule analysis using DNA origami*. *Angew Chem Int Ed Engl*, 2012. **51**(4): p. 874-890.
58. Corey, D.R. and P.G. Schultz, *Generation of a hybrid sequence-specific single-stranded deoxyribonuclease*. *Science*, 1987. **238**(4832): p. 1401-1403.
59. Niemeyer, C.M., T. Sano, C.L. Smith and C.R. Cantor, *Oligonucleotide-directed self-assembly of proteins: semisynthetic DNA--streptavidin hybrid molecules as connectors for the generation of macroscopic arrays and the construction of supramolecular bioconjugates*. *Nucleic Acids Res*, 1994. **22**(25): p. 5530-5539.
60. Kukulka, F. and C.M. Niemeyer, *Synthesis of fluorescent oligonucleotide--EYFP conjugate: towards supramolecular construction of semisynthetic biomolecular antennae*. *Org Biomol Chem*, 2004. **2**(15): p. 2203-2206.
61. Keppler, A., S. Gendreizig, T. Gronemeyer, H. Pick, H. Vogel and K. Johnsson, *A general method for the covalent labeling of fusion proteins with small molecules in vivo*. *Nat Biotechnol*, 2003. **21**(1): p. 86-89.
62. Los, G.V., L.P. Encell, M.G. McDougall, D.D. Hartzell, N. Karassina, C. Zimprich, . . . K.V. Wood, *HaloTag: a novel protein labeling technology for cell imaging and protein analysis*. *ACS Chem Biol*, 2008. **3**(6): p. 373-382.
63. Sacca, B., R. Meyer, M. Erkelenz, K. Kiko, A. Arndt, H. Schroeder, . . . C.M. Niemeyer, *Orthogonal protein decoration of DNA origami*. *Angew Chem Int Ed Engl*, 2010. **49**(49): p. 9378-9383.
64. Meyer, R. and C.M. Niemeyer, *Orthogonal protein decoration of DNA nanostructures*. *Small*, 2011. **7**(22): p. 3211-3218.
65. Fu, J., M. Liu, Y. Liu, N.W. Woodbury and H. Yan, *Interenzyme substrate diffusion for an enzyme cascade organized on spatially addressable DNA nanostructures*. *J Am Chem Soc*, 2012. **134**(12): p. 5516-5519.
66. Endo, M., Y. Katsuda, K. Hidaka and H. Sugiyama, *A versatile DNA nanochip for direct analysis of DNA base-excision repair*. *Angew Chem Int Ed Engl*, 2010. **49**(49): p. 9412-9416.
67. Nakata, E., F.F. Liew, C. Uwatoko, S. Kiyonaka, Y. Mori, Y. Katsuda, . . . T. Morii, *Zinc-finger proteins for site-specific protein positioning on DNA-origami structures*. *Angew Chem Int Ed Engl*, 2012. **51**(10): p. 2421-2424.
68. Sprengel, A., P. Lill, P. Stegemann, K. Bravo-Rodriguez, E.C. Schoneweiss, M. Merdanovic, . . . B. Sacca, *Tailored protein encapsulation into a DNA host using geometrically organized supramolecular interactions*. *Nat Commun*, 2017. **8**: p. 14472.

69. Rinker, S., Y. Ke, Y. Liu, R. Chhabra and H. Yan, *Self-assembled DNA nanostructures for distance-dependent multivalent ligand-protein binding*. *Nat Nanotechnol*, 2008. **3**(7): p. 418-422.
70. Tasset, D.M., M.F. Kubik and W. Steiner, *Oligonucleotide inhibitors of human thrombin that bind distinct epitopes*. *J Mol Biol*, 1997. **272**(5): p. 688-698.
71. Bock, L.C., L.C. Griffin, J.A. Latham, E.H. Vermaas and J.J. Toole, *Selection of single-stranded DNA molecules that bind and inhibit human thrombin*. *Nature*, 1992. **355**(6360): p. 564-566.
72. Banerjee, A., D. Bhatia, A. Saminathan, S. Chakraborty, S. Kar and Y. Krishnan, *Controlled release of encapsulated cargo from a DNA icosahedron using a chemical trigger*. *Angew Chem Int Ed Engl*, 2013. **52**(27): p. 6854-6857.
73. Koirala, D., P. Shrestha, T. Emura, K. Hidaka, S. Mandal, M. Endo, . . . H. Mao, *Single-molecule mechanochemical sensing using DNA origami nanostructures*. *Angew Chem Int Ed Engl*, 2014. **53**(31): p. 8137-8141.
74. Endo, M. and H. Sugiyama, *Single-molecule imaging of dynamic motions of biomolecules in DNA origami nanostructures using high-speed atomic force microscopy*. *Acc Chem Res*, 2014. **47**(6): p. 1645-1653.
75. Ngo, T.A., E. Nakata, M. Saimura and T. Morii, *Spatially Organized Enzymes Drive Cofactor-Coupled Cascade Reactions*. *J Am Chem Soc*, 2016. **138**(9): p. 3012-3021.
76. Krishnan, Y. and F.C. Simmel, *Nucleic acid based molecular devices*. *Angew Chem Int Ed Engl*, 2011. **50**(14): p. 3124-3156.
77. Mao, C., W. Sun, Z. Shen and N.C. Seeman, *A nanomechanical device based on the B-Z transition of DNA*. *Nature*, 1999. **397**(6715): p. 144-146.
78. Yurke, B., A.J. Turberfield, A.P. Mills, Jr., F.C. Simmel and J.L. Neumann, *A DNA-fuelled molecular machine made of DNA*. *Nature*, 2000. **406**(6796): p. 605-608.
79. Meng, W., R.A. Muscat, M.L. McKee, P.J. Milnes, A.H. El-Sagheer, J. Bath, . . . A.J. Turberfield, *An autonomous molecular assembler for programmable chemical synthesis*. *Nat Chem*, 2016. **8**(6): p. 542-548.
80. Song, J., Z. Li, P. Wang, T. Meyer, C. Mao and Y. Ke, *Reconfiguration of DNA molecular arrays driven by information relay*. *Science*, 2017. **357**(6349).
81. Chen, J.H. and N.C. Seeman, *Synthesis from DNA of a molecule with the connectivity of a cube*. *Nature*, 1991. **350**(6319): p. 631-633.
82. Perrault, S.D. and W.M. Shih, *Virus-inspired membrane encapsulation of DNA nanostructures to achieve in vivo stability*. *ACS Nano*, 2014. **8**(5): p. 5132-5140.
83. Grossi, G., M. Dalgaard Ebbesen Jepsen, J. Kjems and E.S. Andersen, *Control of enzyme reactions by a reconfigurable DNA nanovault*. *Nat Commun*, 2017. **8**(1): p. 992.
84. Zhang, Y., S. Tsitkov and H. Hess, *Proximity does not contribute to activity enhancement in the glucose oxidase-horseradish peroxidase cascade*. 2016. **7**: p. 13982.
85. Goldstein, L., Y. Levin and E. Katchalski, *A Water-Insoluble Polyanionic Derivative of Trypsin .2. Effect of Polyelectrolyte Carrier on Kinetic Behavior of Bound Trypsin*. *Biochemistry*, 1964. **3**(12): p. 1913-+.
86. Glettenberg, M. and C.M. Niemeyer, *Tuning of peroxidase activity by covalently tethered DNA oligonucleotides*. *Bioconjug Chem*, 2009. **20**(5): p. 969-975.

87. Rudiuk, S., A. Venancio-Marques and D. Baigl, *Enhancement and modulation of enzymatic activity through higher-order structural changes of giant DNA-protein multibranch conjugates*. *Angew Chem Int Ed Engl*, 2012. **51**(51): p. 12694-12698.
88. Timm, C. and C.M. Niemeyer, *Assembly and purification of enzyme-functionalized DNA origami structures*. *Angew Chem Int Ed Engl*, 2015. **54**(23): p. 6745-6750.
89. Gray, M.J., W.Y. Wholey, N.O. Wagner, C.M. Cremers, A. Mueller-Schickert, N.T. Hock, . . . U. Jakob, *Polyphosphate is a primordial chaperone*. *Mol Cell*, 2014. **53**(5): p. 689-699.
90. Cram, D.J., M.E. Tanner and R. Thomas, *The Taming of Cyclobutadiene*. *Angewandte Chemie-International Edition in English*, 1991. **30**(8): p. 1024-1027.
91. Kang, J.M. and J. Rebek, *Acceleration of a Diels-Alder reaction by a self-assembled molecular capsule*. *Nature*, 1997. **385**(6611): p. 50-52.
92. Tomov, T.E., R. Tsukanov, M. Liber, R. Masoud, N. Plavner and E. Nir, *Rational design of DNA motors: fuel optimization through single-molecule fluorescence*. *J Am Chem Soc*, 2013. **135**(32): p. 11935-11941.
93. Tsukanov, R., T.E. Tomov, Y. Berger, M. Liber and E. Nir, *Conformational dynamics of DNA hairpins at millisecond resolution obtained from analysis of single-molecule FRET histograms*. *J Phys Chem B*, 2013. **117**(50): p. 16105-16109.
94. Tsukanov, R., T.E. Tomov, M. Liber, Y. Berger and E. Nir, *Developing DNA nanotechnology using single-molecule fluorescence*. *Acc Chem Res*, 2014. **47**(6): p. 1789-1798.
95. Nomura, S., K. Tsumoto, T. Hamada, K. Akiyoshi, Y. Nakatani and K. Yoshikawa, *Gene expression within cell-sized lipid vesicles*. *Chembiochem*, 2003. **4**(11): p. 1172-1175.
96. Douglas, T. and M. Young, *Host-guest encapsulation of materials by assembled virus protein cages*. *Nature*, 1998. **393**(6681): p. 152-155.
97. Kerfeld, C.A., S. Heinhorst and G.C. Cannon, *Bacterial microcompartments*. *Annu Rev Microbiol*, 2010. **64**: p. 391-408.
98. Green, S.J., D. Lubrich and A.J. Turberfield, *DNA hairpins: fuel for autonomous DNA devices*. *Biophys J*, 2006. **91**(8): p. 2966-2975.
99. Chou, S.H., K.H. Chin and A.H. Wang, *Unusual DNA duplex and hairpin motifs*. *Nucleic Acids Res*, 2003. **31**(10): p. 2461-2474.
100. Turberfield, A.J., J.C. Mitchell, B. Yurke, A.P. Mills, Jr., M.I. Blakey and F.C. Simmel, *DNA fuel for free-running nanomachines*. *Phys Rev Lett*, 2003. **90**(11): p. 118102.
101. Senior, M.M., R.A. Jones and K.J. Breslauer, *Influence of loop residues on the relative stabilities of DNA hairpin structures*. *Proc Natl Acad Sci U S A*, 1988. **85**(17): p. 6242-6246.
102. Antao, V.P. and I. Tinoco, Jr., *Thermodynamic parameters for loop formation in RNA and DNA hairpin tetraloops*. *Nucleic Acids Res*, 1992. **20**(4): p. 819-824.
103. Vallone, P.M., T.M. Paner, J. Hilario, M.J. Lane, B.D. Faldasz and A.S. Benight, *Melting studies of short DNA hairpins: influence of loop sequence and adjoining base pair identity on hairpin thermodynamic stability*. *Biopolymers*, 1999. **50**(4): p. 425-442.
104. Woodside, M.T., P.C. Anthony, W.M. Behnke-Parks, K. Larizadeh, D. Herschlag and S.M. Block, *Direct measurement of the full, sequence-dependent folding landscape of a nucleic acid*. *Science*, 2006. **314**(5801): p. 1001-1004.

105. Woodside, M.T., W.M. Behnke-Parks, K. Larizadeh, K. Travers, D. Herschlag and S.M. Block, *Nanomechanical measurements of the sequence-dependent folding landscapes of single nucleic acid hairpins*. Proc Natl Acad Sci U S A, 2006. **103**(16): p. 6190-6195.
106. Rief, M., H. Clausen-Schaumann and H.E. Gaub, *Sequence-dependent mechanics of single DNA molecules*. Nat Struct Biol, 1999. **6**(4): p. 346-349.
107. Renner, S., A. Bessonov, U. Gerland and F.C. Simmel, *Sequence-dependent unfolding kinetics of DNA hairpins studied by nanopore force spectroscopy*. J Phys Condens Matter, 2010. **22**(45): p. 454119.
108. Bockelmann, U., P. Thomen, B. Essevaz-Roulet, V. Viasnoff and F. Heslot, *Unzipping DNA with optical tweezers: high sequence sensitivity and force flips*. Biophys J, 2002. **82**(3): p. 1537-1553.
109. Cocco, S., R. Monasson and J.F. Marko, *Unzipping dynamics of long DNAs*. Physical Review E, 2002. **66**(5).
110. Essevaz-Roulet, B., U. Bockelmann and F. Heslot, *Mechanical separation of the complementary strands of DNA*. Proc Natl Acad Sci U S A, 1997. **94**(22): p. 11935-11940.
111. Strunz, T., K. Oroszlan, R. Schafer and H.J. Guntherodt, *Dynamic force spectroscopy of single DNA molecules*. Proc Natl Acad Sci U S A, 1999. **96**(20): p. 11277-11282.
112. Viereg, J.R. and I. Tinoco, *Modelling RNA folding under mechanical tension*. Mol Phys, 2006. **104**(8): p. 1343-1352.
113. Schoneweiss, E.C. and B. Sacca, *The collective behavior of spring-like motifs tethered to a DNA origami nanostructure*. Nanoscale, 2017. **9**(13): p. 4486-4496.
114. Wei, X., J. Nangreave, S. Jiang, H. Yan and Y. Liu, *Mapping the thermal behavior of DNA origami nanostructures*. J Am Chem Soc, 2013. **135**(16): p. 6165-6176.
115. Peters, J.P., 3rd and L.J. Maher, *DNA curvature and flexibility in vitro and in vivo*. Q Rev Biophys, 2010. **43**(1): p. 23-63.
116. Phillips, R., *Physical biology of the cell*. 2. ed. ed. 2013, London [u.a.]: Garland Science.
117. SantaLucia, J., Jr., *A unified view of polymer, dumbbell, and oligonucleotide DNA nearest-neighbor thermodynamics*. Proc Natl Acad Sci U S A, 1998. **95**(4): p. 1460-1465.
118. Zuker, M., *Mfold web server for nucleic acid folding and hybridization prediction*. Nucleic Acids Res, 2003. **31**(13): p. 3406-3415.
119. Alemany, A. and F. Ritort, *Determination of the elastic properties of short ssDNA molecules by mechanically folding and unfolding DNA hairpins*. Biopolymers, 2014. **101**(12): p. 1193-1199.
120. Ashkin, A., *Acceleration and Trapping of Particles by Radiation Pressure*. Physical Review Letters, 1970. **24**(4): p. 156-&.
121. Odijk, T., *Stiff Chains and Filaments under Tension*. Macromolecules, 1995. **28**(20): p. 7016-7018.
122. Smith, S.B., L. Finzi and C. Bustamante, *Direct Mechanical Measurements of the Elasticity of Single DNA-Molecules by Using Magnetic Beads*. Science, 1992. **258**(5085): p. 1122-1126.
123. Wang, M.D., H. Yin, R. Landick, J. Gelles and S.M. Block, *Stretching DNA with optical tweezers*. Biophysical Journal, 1997. **72**(3): p. 1335-1346.
124. Bommarito, S., N. Peyret and J. SantaLucia, *Thermodynamic parameters for DNA sequences with dangling ends*. Nucleic Acids Research, 2000. **28**(9): p. 1929-1934.

125. Mergny, J.L. and L. Lacroix, *UV Melting of G-Quadruplexes*. Curr Protoc Nucleic Acid Chem, 2009. **Chapter 17**: p. Unit 17 11.
126. Hardin, C.C., A.G. Perry and K. White, *Thermodynamic and kinetic characterization of the dissociation and assembly of quadruplex nucleic acids*. Biopolymers, 2000. **56**(3): p. 147-194.
127. Rudiuk, S., A. Venancio-Marques and D. Baigl, *Enhancement and Modulation of Enzymatic Activity through Higher-Order Structural Changes of Giant DNA-Protein Multibranch Conjugates*. Angewandte Chemie International Edition, 2012. **51**(51): p. 12694-12698.
128. Timm, C. and C.M. Niemeyer, *Assembly and Purification of Enzyme-Functionalized DNA Origami Structures*. Angewandte Chemie International Edition, 2015. **54**(23): p. 6745-6750.
129. Petkau-Milroy, K. and L. Brunsveld, *Supramolecular chemical biology; bioactive synthetic self-assemblies*. Org Biomol Chem, 2013. **11**(2): p. 219-232.
130. Xiao, J. and F.R. Salsbury, *Molecular dynamics simulations of aptamer-binding reveal generalized allostery in thrombin*. J Biomol Struct Dyn, 2016: p. 1-16.
131. Hasegawa, H., K.I. Taira, K. Sode and K. Ikebukuro, *Improvement of Aptamer Affinity by Dimerization*. Sensors (Basel), 2008. **8**(2): p. 1090-1098.
132. Di Giusto, D.A. and G.C. King, *Construction, stability, and activity of multivalent circular anticoagulant aptamers*. J Biol Chem, 2004. **279**(45): p. 46483-46489.
133. Di Giusto, D.A., S.M. Knox, Y. Lai, G.D. Tyrelle, M.T. Aung and G.C. King, *Multitasking by multivalent circular DNA aptamers*. ChemBiochem, 2006. **7**(3): p. 535-544.
134. Lao, Y.H., K. Peck and L.C. Chen, *Enhancement of aptamer microarray sensitivity through spacer optimization and avidity effect*. Anal Chem, 2009. **81**(5): p. 1747-1754.
135. Timasheff, S.N., *Protein-solvent preferential interactions, protein hydration, and the modulation of biochemical reactions by solvent components*. Proc Natl Acad Sci U S A, 2002. **99**(15): p. 9721-9726.
136. Levy, Y. and J.N. Onuchic, *Water and proteins: a love-hate relationship*. Proc Natl Acad Sci U S A, 2004. **101**(10): p. 3325-3326.
137. Verespy, S., 3rd, A.Y. Mehta, D. Afosah, R.A. Al-Horani and U.R. Desai, *Allosteric Partial Inhibition of Monomeric Proteases. Sulfated Coumarins Induce Regulation, not just Inhibition, of Thrombin*. Sci Rep, 2016. **6**: p. 24043.
138. Xiao, J. and F.R. Salsbury, *Molecular dynamics simulations of aptamer-binding reveal generalized allostery in thrombin*. J Biomol Struct Dyn, 2017. **35**(15): p. 3354-3369.
139. Castro, C.E., F. Kilchherr, D.N. Kim, E.L. Shiao, T. Wauer, P. Wortmann, . . . H. Dietz, *A primer to scaffolded DNA origami*. Nat Methods, 2011. **8**(3): p. 221-229.
140. Stahl, E., T.G. Martin, F. Praetorius and H. Dietz, *Facile and scalable preparation of pure and dense DNA origami solutions*. Angew Chem Int Ed Engl, 2014. **53**(47): p. 12735-12740.
141. Sano, T., M.W. Pandori, X. Chen, C.L. Smith and C.R. Cantor, *Recombinant core streptavidins. A minimum-sized core streptavidin has enhanced structural stability and higher accessibility to biotinylated macromolecules*. J Biol Chem, 1995. **270**(47): p. 28204-28209.
142. Russo Krauss, I., A. Pica, A. Merlino, L. Mazzarella and F. Sica, *Duplex-quadruplex motifs in a peculiar structural organization cooperatively contribute to thrombin binding of a DNA aptamer*. Acta Crystallogr D Biol Crystallogr, 2013. **69**(Pt 12): p. 2403-2411.

143. Russo Krauss, I., A. Merlino, A. Randazzo, E. Novellino, L. Mazzarella and F. Sica, *High-resolution structures of two complexes between thrombin and thrombin-binding aptamer shed light on the role of cations in the aptamer inhibitory activity*. Nucleic Acids Res, 2012. **40**(16): p. 8119-8128.
144. Bode, W., I. Mayr, U. Baumann, R. Huber, S.R. Stone and J. Hofsteenge, *The refined 1.9 Å crystal structure of human alpha-thrombin: interaction with D-Phe-Pro-Arg chloromethylketone and significance of the Tyr-Pro-Pro-Trp insertion segment*. EMBO J, 1989. **8**(11): p. 3467-3475.
145. Vanommeslaeghe, K. and A.D. MacKerell, Jr., *CHARMM additive and polarizable force fields for biophysics and computer-aided drug design*. Biochim Biophys Acta, 2015. **1850**(5): p. 861-871.
146. Phillips, J.C., R. Braun, W. Wang, J. Gumbart, E. Tajkhorshid, E. Villa, . . . K. Schulten, *Scalable Molecular Dynamics with NAMD*. J Comput Chem, 2005. **26**(16): p. 1781-1802.
147. Jorgensen, W.L., J. Chandrasekhar, J.D. Madura, R.W. Impey and M.L. Klein, *Comparison of simple potential functions for simulating liquid water*. The Journal of Chemical Physics, 1983. **79**(2): p. 926-935.
148. Förster, T., *Zwischenmolekulare Energiewanderung und Fluoreszenz*. Ann. Phys., 1948. **437**(1-2): p. 55-75
149. Marras, S.A., *Selection of fluorophore and quencher pairs for fluorescent nucleic acid hybridization probes*. Methods Mol Biol, 2006. **335**: p. 3-16.
150. Berney, C. and G. Danuser, *FRET or no FRET: a quantitative comparison*. Biophys J, 2003. **84**(6): p. 3992-4010.
151. Ubarretxena-Belandia, I., L. Hozeman, E. van der Brink-van der Laan, E.H. Pap, M.R. Egmond, H.M. Verheij and N. Dekker, *Outer membrane phospholipase A is dimeric in phospholipid bilayers: a cross-linking and fluorescence resonance energy transfer study*. Biochemistry, 1999. **38**(22): p. 7398-7405.
152. Lorenz, M. and S. Diekmann, *Quantitative distance information on protein-DNA complexes determined in polyacrylamide gels by fluorescence resonance energy transfer*. Electrophoresis, 2001. **22**(6): p. 990-998.
153. Clegg, R.M., A.I. Murchie and D.M. Lilley, *The solution structure of the four-way DNA junction at low-salt conditions: a fluorescence resonance energy transfer analysis*. Biophys J, 1994. **66**(1): p. 99-109.
154. Tsiang, M., A.K. Jain, K.E. Dunn, M.E. Rojas, L.L. Leung and C.S. Gibbs, *Functional mapping of the surface residues of human thrombin*. J Biol Chem, 1995. **270**(28): p. 16854-16863.
155. A. Trapaidze, A.B., and M. Brut, *Binding modes of thrombin binding aptamers*. Appl. Phys. Lett., 2015. **106**(043702).

A List of Physical Parameter and Abbreviations

List of physical parameters and abbreviations

2D	two dimensional
3D	three dimensional
%	Percentage
°	Degree
Å	Ångström
°C	Degree Celsius
ΔG	Change in free energy
ΔH	Change in free enthalpy
ΔS	Change in entropy
ε	Absorption coefficient
θ	Folded fraction of the structures
μg	Microgram
μl	Micoliter
μm	Micrometer
μM	Mircomolar
A	Adenosin
AFM	Atomic force microscopy
amp	Ampicillin
APS	Ammonium persulfate
a.u.	Arbitrary units
B	Boric acid
BG	Benzylguanin
bp	Basepairs
BSA	Bovine serum albumin

c	Concentration
C	CLOSED
C	Cytosine
cam	chloramphenicol
CCP	Covalent protein conjugate
CH	Chlorohexan
Cl₂	Chloride
CTR	Control
d	Thickness of the cuvette
D	FAM fluorescence emission intensity of the sample containing only the donor molecule
DA	FAM fluorescence emission intensity of the sample containing the donor and acceptor molecule
DMSO	Dimethylsulfoxid
DNA	Deoxyribonucleic acid
DX	Double crossover tiles
E₀	Initial enzyme concentration
E	Extinction
E	FRET efficiency
EDTA	Ethylenediaminetetraacetic
Eq.	Equation
Etbr	Ethidiumbromide
F	Extinction coefficient
F	Folded structures
F	Force
FAM	Carboxyfluorescein
Fig.	Figure
FITC	Fluorescein isothiocyanate
FRET	Fluorescence resonance energy transfer spectroscopy

G	Guanine
g	Gram
GOX	Glucose oxidase
h /hrs	Hour / hours
HCl	Hydrogen chloride
H₂O	Water
HRP	Horseradish peroxidase
I₀	Intensity of the entering light
I	Intensity of the exiting light
IB	Inclusion bodies
IPTG	Isopropyl β -D-1-thiogalactopyranoside
k	Spring constant
kb	Kilo base
k_BT	Boltzman factor
kcal	Kilo calorie
k_{cat}	Catalytic rate, turnover number
KCl	Potassium chloride
kDA	Kilo Dalton
K_{eq}	equilibrium constant
K_m	Michaelis constant
L_c	Contour length
L_p	Persistence length
M	Molecular weight
M	Molar
Mg	Magnesium
min	Minute
ml	Milliliter

mM	Milimolar
MWCO	Molecular weight cut off
n°	Number
NaCl	Sodium chloride
(NH₄)₂SO₄	Ammonium sulfate
ng	Nanogram
nM	Nanomolar
nm	Nanometer
NN	Nearest neighbor
norm.	Normalized
O	Open
OD	Optical density
PBS	Phosphate buffered saline
PEG	Polyethyleneglycole
pN	Piconewton
PNA	Peptidenucleic acid
qRTPCR	quantitative Real Time Polymerase Chain Reaction
R	End-to-end distance
R	Ideal gas constant
RC	Reclosed
rcf	Relative centrifugal force
rmsf	Root mean square flexibility
RNA	Ribonucleic acid
rpm	Rounds per minute
RT	Room temperature
S	Substrate concentration
SDS-PAGE	Sodium dodecyl sulfate polyacrylamide gel electrophoresis

sec	Second
SEM	Standard error of the mean
ss	Single stranded
STV	Streptavidin
sulfoSMCC	Sulfosuccinimidyl 4-(N-maleimidomethyl) cyclohexane- 1-carboxylate
T	Temperature
T	Thymine
Tab.	Table
TAMRA	Carboxytetramethylrhodamine
TBA1	Thrombin binding aptamer 1
TBA2	Thrombin binding aptamer 2
TEM	Transmission electron microscopy
TEMED	Tetramethylethylenediamine
tetra	tetracycline
TIRF	Total internal reflection fluorescence microscopy
T_m	Melting temperature
TRIS	tris(hydroxymethyl)aminomethane
U	Unfolded structures
UV	Ultraviolette
V	Volt
V	Dilutionfactor
v₀	initial reaction rate
v_{max}	Maximum enzymtaic rate
WLC	Worm Like Chain

B List of Figures

Main text

Figure 1-1: Schematic representation of the DNA double helix.	3
Figure 1-2: Pioneering work of Ned Seeman, representing the fundamental idea of the rapid growing DNA nanotechnology field.	4
Figure 1-3: Multiple-branched antiparallel DNA motifs: the so-called DX tiles.	5
Figure 1-4: The scaffolded DNA origami approach.	7
Figure 1-5: Examples for functionalization of distinct DNA nanostructures by means of covalent approaches.	12
Figure 1-6: Examples for functionalization of distinct DNA nanostructures by means of the non-covalent approach.	13
Figure 1-7: Toehold-mediated single strand displacement.	15
Figure 3-1: Characterization of the modified streptavidin protein.	23
Figure 3-2: AFM characterization of construct 0 and I.	25
Figure 3-3: Visualization of the correct functioning of constructs type 0, I and II.	26
Figure 3-4: AFM characterization of construct II in the closed, open and reclosed state and construct III in the closed state.	27
Figure 3-5: Demonstration of the reversible functioning of the four-state DNA origami device (construct III) bearing a second set of loops in series.	29
Figure 3-6: (a) Schematic illustration of the prepared FRET-thermal analysis constructs.	31
Figure 3-7: Construct type 0 is the most rigid structure analyzed during this study, containing no flexible hairpin motifs integrated along the seam sequence.	33
Figure 3-8: Curves obtained by temperature-dependent FRET spectroscopy for construct I, featuring one set of hairpin loops.	34
Figure 3-9: Constructs type II and III bearing two identical or two different sets of parallel hairpin loops along the seam.	35
Figure 3-10: CanDo three-dimensional model of the presented DNA nanostructure, omitting (a) or featuring (b) the single stranded hairpin motifs tethered along the seam.	36
Figure 3-11: Normalized thermal cooling (blue) and melting (red) curve of sample I/5 analyzed by UV spectroscopy.	37
Figure 3-12: Data collection of the free energy change (ΔG , grey bars) and melting temperature (T_m , black bars) attributed to the cooling process of the compact hairpin (a,b) and the duplex (c).	39
Figure 3-13: Representation of the spring model estimation for the constructs obtaining one, two identical or two different hairpin motifs in series tethered to the origami frame.	45
Figure 3-14: Proposed free energy landscape of the organized collection of hairpin motifs tethered to the DNA nanoarchitecture according to a hybrid nearest neighbour/worm-like chain model.	48

Figure 3-15: NN model approximation of the transition of a single hairpin motif ($T_3C_5T_5G_5T_3$) in its closed state to its open state (additional formation of 10 bp: T_5G_5/C_5A_5), upon hybridization with a complementary fuel strand (orange).	49
Figure 3-16: Comparison of the normalized FAM emission intensity during the cooling process of the labeled hairpin motif ($C_5T_5G_5$), either free in solution (black curve) or embedded within the origami surface at position 5 of the seam (purple curve, attributed to construct I/5).	53
Figure 3-17: Monitored FAM emission intensity during a mechanical unfolding/refolding process of a G4 motif connected into the inner cavity of the reconfigurable I/5 construct.	55
Figure 3-18: 25% non-denaturing PAGE characterization of the correct G-quadruplex formation free in solution, relying on design 1, using FRET analysis.	59
Figure 3-19: Gel electrophoresis characterization of the correct configuration of the embedded G4-motifs within the inner cavity exemplary shown for design 1.	60
Figure 3-20: Thrombin stability characterization by SDS-PAGE gel electrophoresis at room temperature (a) and 37°C (b).	61
Figure 3-21: AFM characterization of the presented designs 0, 1 and 2 for protein encapsulation.	64
Figure 3-22: Computational binding studies for design 2.	65
Figure 3-23: AFM characterization of the presented designs 3S and 3L for protein encapsulation.	66
Figure 3-24: Summary of the data (mean + SEM) gained by AFM characterization of the DNA-loaded nanocage with the protein thrombin.	67
Figure 3-25: Gel electrophoresis characterization of D1.	69
Figure 3-26: Activity of thrombin within the DNA origami device featuring the ligands in D1 configuration (a) compared to the aptamers freely moving in solution (b) evaluated at 100 nM.	70
Figure 3-27: Activity of thrombin within the DNA origami device featuring the ligands in a D1 configuration compared to the aptamers freely moving in solution (a) and data set for the distinctive designs applied during this study (b), all evaluated at 100 nM.	73
Figure 4-1: Overview of the distinctive designs used in this study.	75
Figure 4-2: Schematic representation of the operational movement for construct I.	76
Figure 4-3: Detail design of the hairpin motif used in construct I.	77
Figure 4-4: Design of the hairpin motifs for construct II.	78
Figure 4-5: Design of the two different hairpin motifs 1 (a), 2 (b) and the linking between 1 & 2 (c) for construct III.	79
Figure 4-6: NUPACK analysis of the different hairpin motifs used in this study for construct I, II and III.	80
Figure 4-7: Schematical representation of the modification of the inner cavity to encapsulate the protein thrombin.	81
Figure 4-8: Schematic representation of the DNA origami structure modified with three oligonucleotides on the left side of the device (topographical marker) and containing a biotin molecule at the 5'-end, extending out of the origami plane.	87
Figure 4-9: Schematic representation of the aptamer modification for analysis of correct G-quadruplex formation using FRET spectroscopy technology for D1.	90

Figure 4-10: Experimental set up of the FRET-thermal analysis. _____	96
Figure 4-11: Illustration of the tug-of-war experiment using the origami design of construct I. _____	97
Figure 4-12: Starting setup for the five MD simulations performed. _____	101

E Supplementary Information

Figure E-1: Prove of principle of correct streptavidin expression and purification. _____	127
Figure E-2: Demonstration of correct assembly and labeling for construct 0, I, II and III used in section 4.2. _____	129
Figure E-3: Specification of the applied FRET-substrate used during the enzymatic activity assays. _____	131
Figure E-4: Standard curve for the calculation of the Michaelis Menten kinetic parameters determined by a dilution series of the substrate containing the donor fluorophore only. _____	131
Figure E-5: FAM fluorescence emission intensities for different aptamer concentrations (50, 80, 100 and 120 nM) for TBA1 (a), TBA2 (b), TBA12 in 1x TEMg KCl, 30 nM thrombin and 20 μ M substrate. _____	132
Figure E-6: FAM fluorescence emission intensities for different thrombin concentrations (30, 50 and 80 nM) in presence of TBA1 (a), TBA2 (b), TBA12 (c) and without any aptamers in solution (d) in 1x TEMg KCl, 100 nM aptamer and 20 μ M substrate. _____	133
Figure E-7: FAM fluorescence emission intensities for different aptamer concentrations (50, 80, 100 and 120 nM) for TBA1 (a), TBA2 (b), TBA12 (c) in 1x TEMg, 30 nM thrombin and 20 μ M substrate. _____	134
Figure E-8: FAM fluorescence emission intensities for different thrombin concentrations (30, 50 and 80 nM) in presence of TBA1 (a), TBA2 (b), TBA12 (c) and without any aptamers in solution (d) in 1x TEMg, 100 nM aptamer and 20 μ M substrate. _____	135
Figure E-9: FAM fluorescence emission intensities representing the proteolytic activity of the tested protein. Evaluated were the free aptamers in solution (a) compared to the protein enveloped in cage D1 (b) and destroyed constructs (c). _____	135

C List of Tables

Main text

Table 3-1: Thermodynamic parameters obtained from temperature-dependent FRET experiments for the cooling process. _____	40
Table 3-2: Thermodynamic parameters obtained from temperature-dependent FRET experiments for the melting process. _____	41
Table 3-3: AFM- analysis data for yields of protein encapsulation. _____	68
Table 3-4: Summary of Michaelis-Menten kinetic evaluation (mean \pm SEM) for aptamers moving free in solution, i.e. not tethered to the DNA origami platform. _____	71
Table 3-5: Summary of Michaelis-Menten kinetic evaluation (mean \pm SEM) for design 1. _____	72
Table 3-6: Summary of Michealis-Menten kinetic evaluation (mean \pm SEM) for design 1, 2, 3s, 3l and both aptamers moving free in solution. _____	73
Table 4-1: Assay-Mix (# 4331348). _____	85
Table 4-2: Master-Mix qRT-PCR. _____	86
Table 4-3: Cycle parameter. _____	86
Table 4-4: Running parameters used during the enzyme kinetic measurements. _____	93

E Supplementary Information

Table E-1: Buffer, media and solutions.	136
Table E-2: Chemicals & miscellaneous reagents.	137
Table E-3: Cells, plasmids, antibodies & enzymes.	139
Table E-4: DNA origami left side of the structure.	140
Table E-5: DNA origami right side of the structure.	144
Table E-6: List of the oligonucleotides used for modification of the seam in construct I.	148
Table E-7: List of the oligonucleotides used for modification of the seam in construct II with inner segment A: 5'-ATCGAACTGGGC-3'.....	149
Table E-8: List of the oligonucleotides used for modification of the seam in construct II with inner sequence B: 5'-CGCTGATGCACT-3'.....	150
Table E-9: List of the oligonucleotides used for modification of the seam in construct III with inner sequence B: 5'-CGCTGATGCACT-3'.....	151
Table E-10: List of the oligonucleotides used for FRET analysis of the hairpin motifs of construct I.	152
Table E-11: List of the oligonucleotides used for FRET analysis of the hairpin motifs of construct II and III.	152
Table E-12: List of oligonucleotides for FRET tag-of-war analysis of construct I.	153
Table E-13: List of oligonucleotides for inner cavity modifications for thrombin encapsulation of construct I.	153
Table E-14: List of primers for m13mp18 sequencing.	154

Table E-15: Consumables & kits.	155
Table E-16: General equipment.	156

D List of Equations

Main text

<i>Eq. [3-1] Hooke's law</i>	42
<i>Eq. [3-2] Construct I- set of springs in parallel</i>	43
<i>Eq. [3-3] Construct I- set of springs in parallel</i>	43
<i>Eq. [3-4] Construct I- set of springs in parallel</i>	43
<i>Eq. [3-5] Construct I- set of springs in parallel</i>	43
<i>Eq. [3-6] Construct I- set of springs in parallel</i>	43
<i>Eq. [3-7] Construct I- set of springs in parallel</i>	43
<i>Eq. [3-8] Construct I- set of springs in parallel</i>	43
<i>Eq. [3-9] Construct II and III- set of springs in parallel</i>	44
<i>Eq. [3-10] Construct II and III- set of springs in parallel</i>	44
<i>Eq. [3-11] Construct II and III- set of springs in parallel</i>	44
<i>Eq. [3-12] Construct II and III- set of springs in parallel</i>	44
<i>Eq. [3-13] Construct II and III- set of springs in parallel</i>	45
<i>Eq. [3-14] Worm-Like Chain (WLC) model</i>	50
<i>Eq. [3-15] Worm-Like Chain (WLC) model</i>	51
<i>Eq. [4-1] Lambert-Beer law</i>	83
<i>Eq. [4-2] Lambert-Beer law</i>	83
<i>Eq. [4-3] Lambert-Beer law</i>	83
<i>Eq. [4-4] Michaelis Menten kinetic</i>	92
<i>Eq. [4-5] Michaelis Menten kinetic</i>	92
<i>Eq. [4-6] Van 't Hoff analysis</i>	95
<i>Eq. [4-7] Van 't Hoff analysis</i>	95
<i>Eq. [4-8] Van 't Hoff analysis</i>	95
<i>Eq. [4-9] Van 't Hoff analysis</i>	95
<i>Eq. [4-10] Van 't Hoff analysis</i>	95

Supplementary Information

<i>Eq. [E-1] FRET Efficiency</i>	128
----------------------------------	-----

E Supplementary Information

Streptavidin as topological marker

As a proof of principle, the produced streptavidin during this study was tested to be applicable for further evaluations (figure e-1):

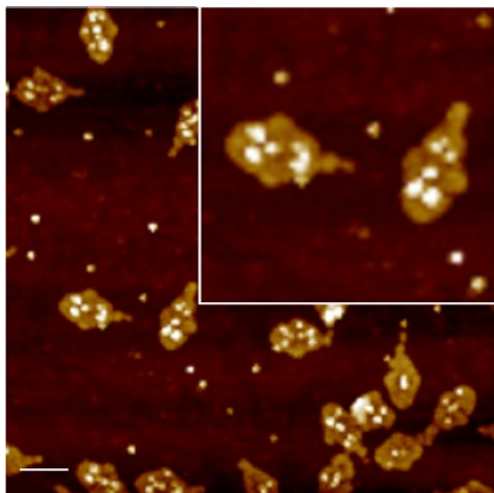


Figure E-1: Prove of principle of correct streptavidin expression and purification. Bright white spots indicate correct streptavidin hybridization to the biotin molecules bound to the extended protruding DNA oligonucleotides, orthogonal to the origami construct plane. Scale bar is in 100 nm.

Förster resonance energy transfer (FRET)

The Förster resonance energy transfer (FRET) is a biophysical analyzing technique to evaluate the distances between distinctive selected molecules, developed by Theodor Förster [148]. The mechanism relies on a non-radiative energy transfer between the donor fluorophore and the acceptor molecule [149]. By specific excitation of the donor molecule, the electrons of the donor gain a higher instable vibrational state compared to the initial level. Therefore, by returning back to the lowest energy state, the electron emits energy that is transferred to the nearby acceptor molecule, resulting in decreased donor fluorescence emission and increased acceptor fluorescence emission [149]. A mechanism called quenching, leading to fluorescence emission of the acceptor's characteristic emission wavelength. The FRET efficiency can be calculated as a fraction of the energy originally absorbed by the donor-acceptor and the donor only sample [150], using the following equation:

$$E = 1 - \frac{F(DA)}{F(D)}$$

Eq. [E-1]

with:

F(DA) Emission fluorescence intensity of the donor-acceptor sample

F(D) Emission fluorescence intensity of the donor only sample

Due to the FRET efficiency's dependence on the interfluorophore distance, FRET is widely used as a molecular ruler, for example to study protein-protein interactions [151] or in nucleic acid [152] or DNA-nanotechnology based approaches [153]. A detailed description of the all calculations is given in the section 4.2.4.1.

Design and FRET labeling of the device

Correct formation and assembly of the spring like motif tethered to the DNA nanostructure were estimated by ensemble FRET measurements. As shown in the gel of figure e-2, the samples containing only the donor-molecule show no TAMRA fluorescence signal construct I, containing the donor and acceptor molecule shows instead a high FRET efficiency due to the shorter intermolecular distance between the FRET reporters. Differently, the systems containing two loops in series show a simple overlay of the two fluorescent signals (green and red band of construct II and III).

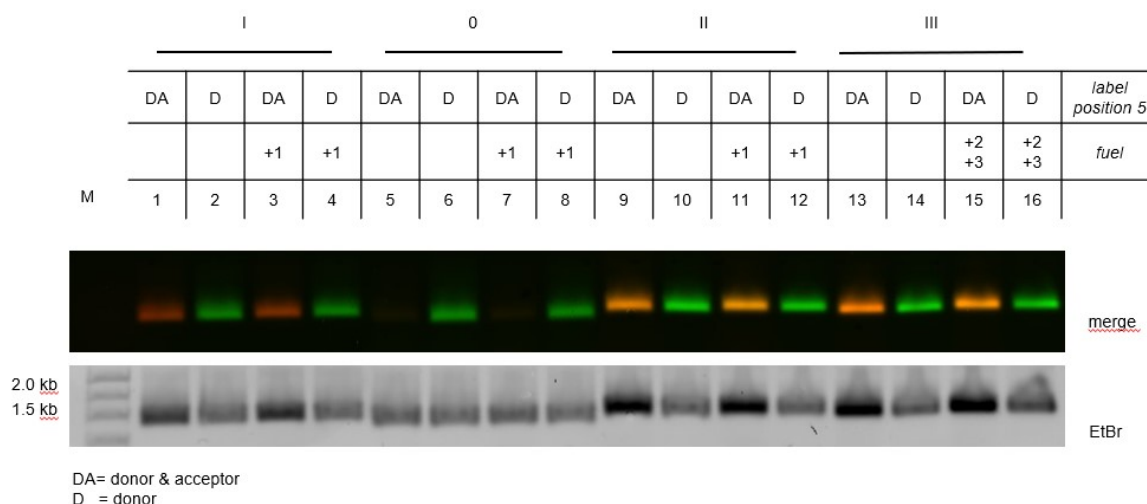


Figure E-2: Demonstration of correct assembly and labeling for construct 0, I, II and III used in section 3.2. As estimated the samples containing only the donor-molecule show no TAMRA fluorescence signal compared to the samples containing the donor and acceptor molecule. As well a high FRET efficiency in construct I, bearing only one set of hairpin loops integrated along the seam sequence, could be demonstrated, based on the shorter intermolecular distance between the integrated FRET reporters compared to the systems containing two loops in series, i.e. overlay of the green and red fluorescence signal (construct II and III).

Thrombin binding aptamers (TBA1 and TBA2)

TBA1

TBA1 is a 15 mer 5'-GGTTGGTGTGGTTGG-3' and was identified by SELEX (Systematic Evolution of Ligands by Exponential Enrichment) with a K_D of ca. 75-100 nM binding to the fibrinogen recognition exosite I [70;71].

Structure/binding mode: The tertiary structure of TBA1 is an anti-parallel G-quadruplex. This chair-like structure is folded through the stacking of two guanine (G)-tetrads. Each G-quartet is stabilized by non-Watson-Crick-like hydrogen bonds (more likely Hoogsteen-like hydrogen bonds). According to the NMR (1HAO)18 and X-ray crystallographic images (4DIH; 4DII) [143] the correct topology of the TBA1 consists of a TGT loop on the wide side and the TT loops on the narrow sites. TBA is bound to the exosite I of thrombin majorly via its two TT loops (T3, T4 and T12, T13) through polar and hydrophobic interactions. The residues His71, Arg75, Tyr76, Arg77, Asn78, Ile79, Tyr117 in the exosite I epitope are involved in the interaction with TBA. In particular,

T3 interacts with His71, which plays a critical role for fibrinogen recognition, both through hydrogen bonding and hydrophobic interaction [154].

Role of ions: A potassium ion helps TBA1 folding into a G-quadruplex structure. Also, the potassium ion improves the thermal stability of TBA1. Compared with sodium, the potassium ion fits perfectly between two G-tetrad planes and is coordinately bound to four O6 atoms in each plane. This enhances the structural stability of TBA1. In contrast, due to its small size, sodium ion can only interact with four rather than eight oxygen atoms of two G-tetrad planes, and accordingly has two alternative positions in respect to the G-tetrad plane. Thrombin shows similar influence as potassium ion. In the ion-deficient condition, thrombin helps TBA1 to fold into a stable G-quadruplex structure from a randomized coil, which is known as “target-induced” conformational change [70].

Molecular models/binding energy: The results of *in silico* calculations with the molecular mechanics Poisson-Boltzmann surface area (MM-PBSA) method, suggest that the calculated binding energy (ΔG) of TBA to thrombin exosite I is slightly stronger in the presence of K^+ (-66.73 kcal/mol) than in the case of Na^+ (-60.29 kcal/mol), however both states are likely to coexist [155].

TBA2

TBA2 is an optimized 29-mer (5'- AGTCCGTGGTAGGGCAGGTTGGGGTGACT-3') [70]. This aptamer recognizes the exosite II of thrombin, which mediates the heparin binding. The K_D is much higher than TBA1 (ca. 0.5 nM) and it has a better binding affinity than TBA1 and is therefore more sensitive to thrombin detection (till nanomolar concentration). Nevertheless, it may still be challenging to discriminate target from non-target in mixed protein samples.

Structure/binding mode: Unlike TBA1, it holds a duplex/G-quadruplex mixed structure. The X-ray crystallographic image with 2.4 Å resolution was reported recently (4I7Y) [142]. Since the exosite II is a positively charged motif, it creates many ion pairs with the TBA2 backbone especially in the duplex region. Hydrophobic interactions are mainly observed in the G-quadruplex region (T9, T18 and T10), and this stabilizes the complex formation.

Molecular models/binding energy: Calculated binding energy of TBA2 to thrombin exosite II is -88.37 kcal/mol [155].

Evaluation of the proteolytic activity of the caged protein

Here we describe the experimental conditions used for the analysis of the encapsulated thrombin protein (section 3.3.4) and proteolytic digestion of the FRET substrate. The substrate was supplied from INTAVIS. The specification parameters are listed in figure e-3.

Tabelle der Peptidsequenzen 16127				E. Schöneweiß				
Nr.	Bezeichnung	Aminosäuresequenz	Lot	MG [g/mol]	Masse [Da]	gefundene Masse [Da]	Einwaage [mg]	HPLC Reinheit [%]
1	Peptid-1	FCA-GG -D-Phe-PR SGGG-Lys (BHQ-1) - K-OH	RSA161031_14F31-34	1892,02	1890,81	1891,00	6,2	95,0
2	Peptid-2	FCA-GG -D-Phe-PR SGGGK K-OH	RSA161031_15F8-13	1405,49	1404,61	1404,70	5,9	>99

Figure E-3: Specification of the applied FRET-substrate used during the enzymatic activity assays. The peptide sequence was chosen with help of the databank MEROPS.

For the calculation of the Michaelis Menten kinetic parameters, a standard curve was produced by a dilution series of the substrate (standard curve, figure e-4), containing only the donor fluorophore (peptide 2 in figure e-3) was evaluated. By means of that one can calculate the concentration of the cleaved FRET substrate, which results in the release of the donor from the acceptor molecule accompanied by an increased FAM fluorescence emission intensity during the enzyme kinetics experiments. From this value one can calculate the enzyme rate ($\mu\text{M}/\text{min}$).

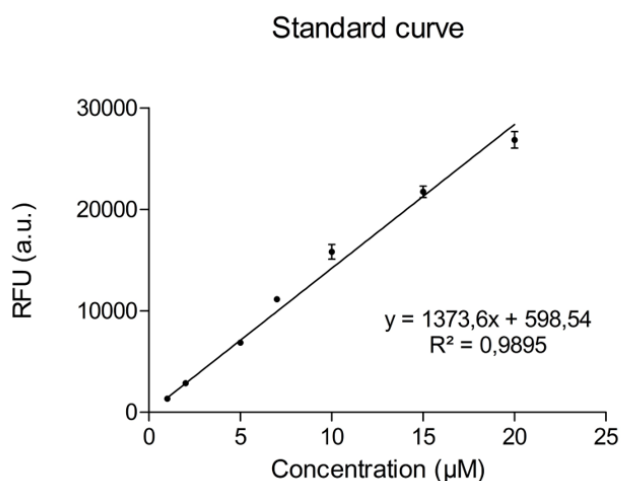


Figure E-4: Standard curve for the calculation of the Michaelis Menten kinetic parameters determined by a dilution series of the substrate containing the donor fluorophore only.

Initially, the aptamers ((a) TBA1, (b) TBA2 and a mix (c) of equal concentrated TBA1 and TBA2) free in solution were analyzed to determine the appropriated aptamer concentration in 1x TEMgKCl (figure e-5). It could be demonstrated that the change in aptamer concentration did not influence the initiation of the kinetic process (first 10 minutes), mostly used in the kinetic analysis. Therefore, to be consistent and comparable with later experiments on nanocage constructs, the concentration of the aptamers free in solution, serving as control in later analysis, were set to 100 nM.

In a second step, the optimal enzyme concentration was determined in 1x TEMgKCl (figure e-6). This was set to 30 nM thrombin for all further experiments.

Because DNA nanoconstructs D1, D2 and D3 are normally dissolved in TEMg 1x (i.e. in absence of potassium ions), the same experiments were repeated to determine the appropriated aptamer concentration (figure e-7) and optimal enzyme concentration (figure e-8). The data revealed a drastic increase in fluorescence intensity and therefore the buffer used for the evaluation of the proteolytic activity of the caged protein was set to TEMg 1x instead of TEMgKCl 1x (3.3.4).

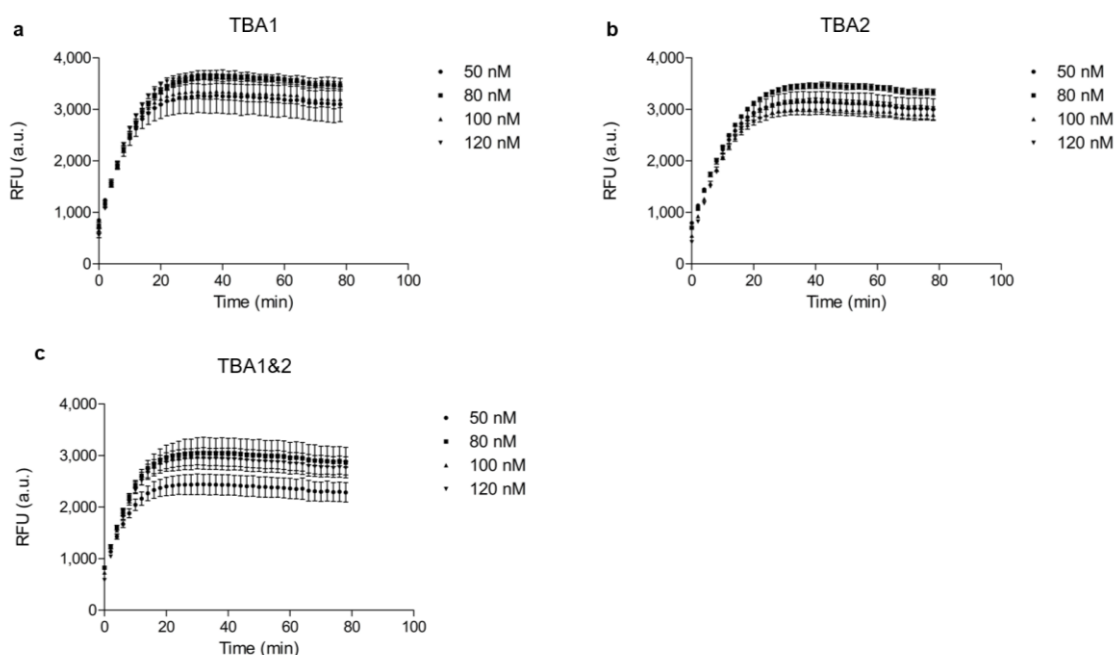


Figure E-5: FAM fluorescence emission intensities for different aptamer concentrations (50, 80, 100 and 120 nM) for TBA1 (a), TBA2 (b), TBA1&2 in 1x TEMg KCl, 30 nM thrombin and 20 μM substrate.

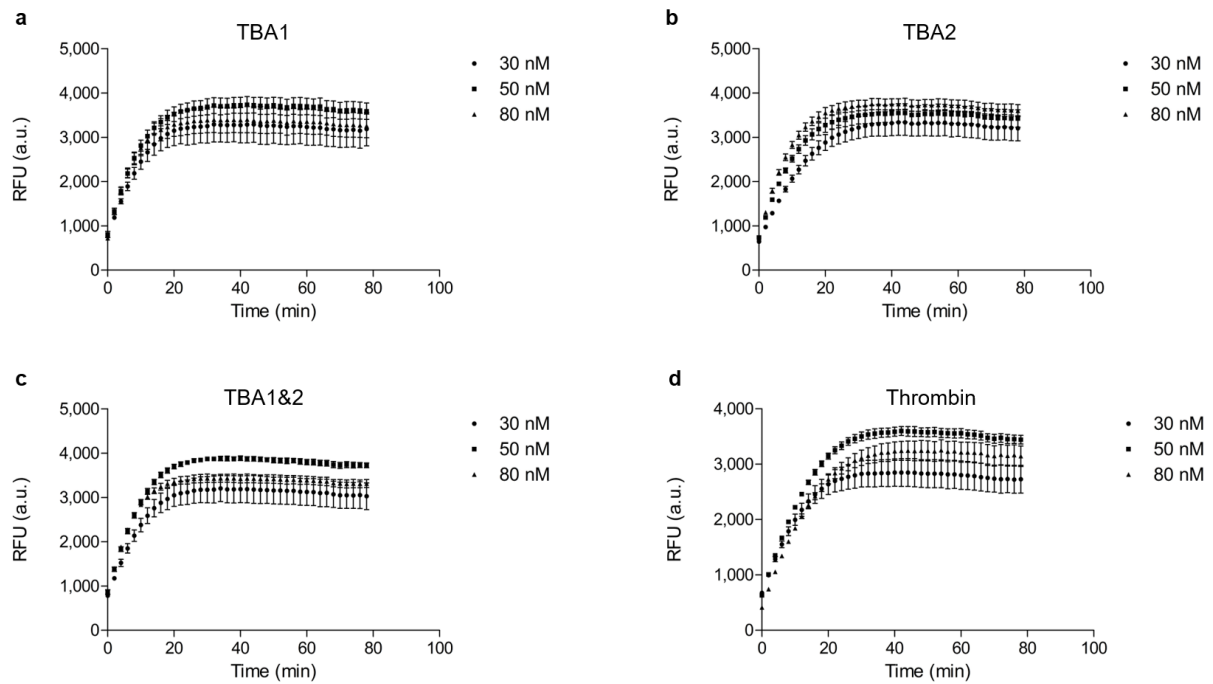


Figure E-6: FAM fluorescence emission intensities for different thrombin concentrations (30, 50 and 80 nM) in presence of TBA1 (a), TBA2 (b), TBA1&2 (c) and without any aptamers in solution (d) in 1x TEMg KCl, 100 nM aptamer and 20 μ M substrate.

However, the results within this buffer conditions did not change dramatically for the optimal chosen aptamer concentration (100 nM; figure e-7 (a)-(c)) and enzyme concentration (30 nM; figure e-8 (a)-(d)). Additionally, several control samples were evaluated, all showing the expected results ((d), figure e-7). The peptide, containing only the donor fluorophore (CTR S D), gave the highest fluorescence intensity, whereas the FRET substrate (CTR S DA), the blank control (CTR blank), the buffer control (CTR buffer) and the enzyme control (CTR THR) all showed no fluorescence signal at all.

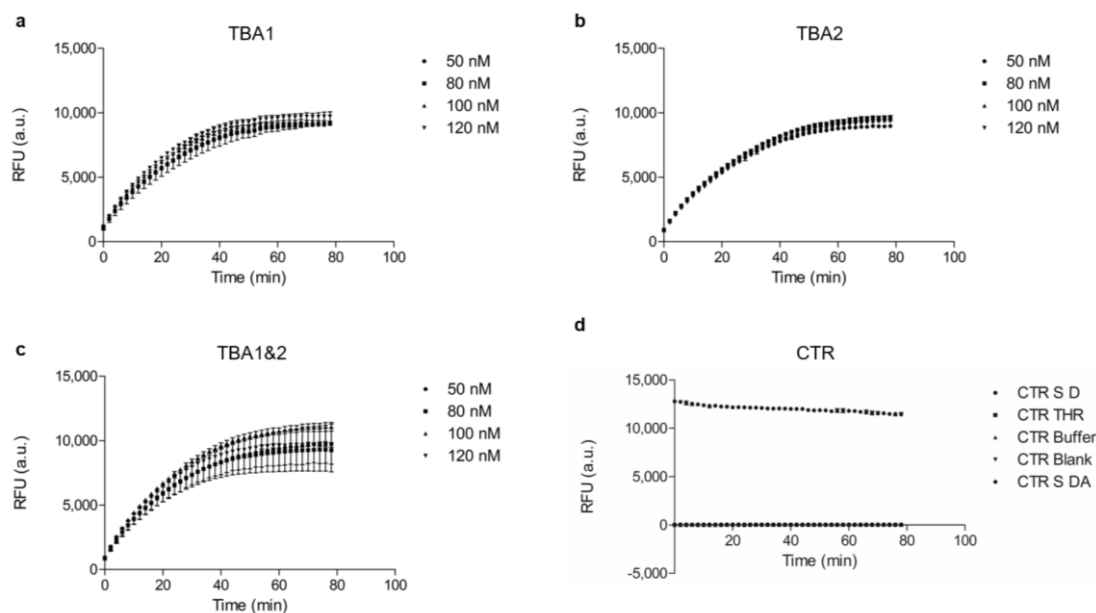


Figure E-7: FAM fluorescence emission intensities for different aptamer concentrations (50, 80, 100 and 120 nM) for TBA1 (a), TBA2 (b), TBA1&2 (c) in 1x TEMg, 30 nM thrombin and 20 μ M substrate. The different control samples show the estimated results. (d) Several control samples were evaluated. The sample containing the substrate with only the donor molecule showed the maximal fluorescence intensity (CTR S D), whereas the fluorescence intensity of the measured FRET-substrate dropped to the minimal level (CTR S DA). The enzyme control sample (CTR THR), containing no substrate, the measurement of an empty well (CTR blank) and evaluation of the used buffer system without any supplements (CTR Buffer) were comparable to that.

The optimal parameters were then tested for the system of the free aptamers in solution, the cage system D1 and the melted DNA origami structures. Figure E-9 shows the raw data obtained from the kinetic analysis. The results reveal, that in general the presence of DNA enhances the proteolytic activity of the protein (d). But there are massive differences between the individual samples, although all samples were equal in concentration and therefore quantitatively comparable. The sample containing only the protein showed the lowest proteolytic activity (turquoise curve). Upon addition of the different aptamers sequences, the activity slightly improved (grey curves). The disordered system (red curves, destroyed structures) showed the highest enzymatic processing. However, enveloping the protein in cage D1, i.e. using an ordered system, led already to an enormous enhancement of the enzyme activity (black curves) when compared to the other systems evaluated.

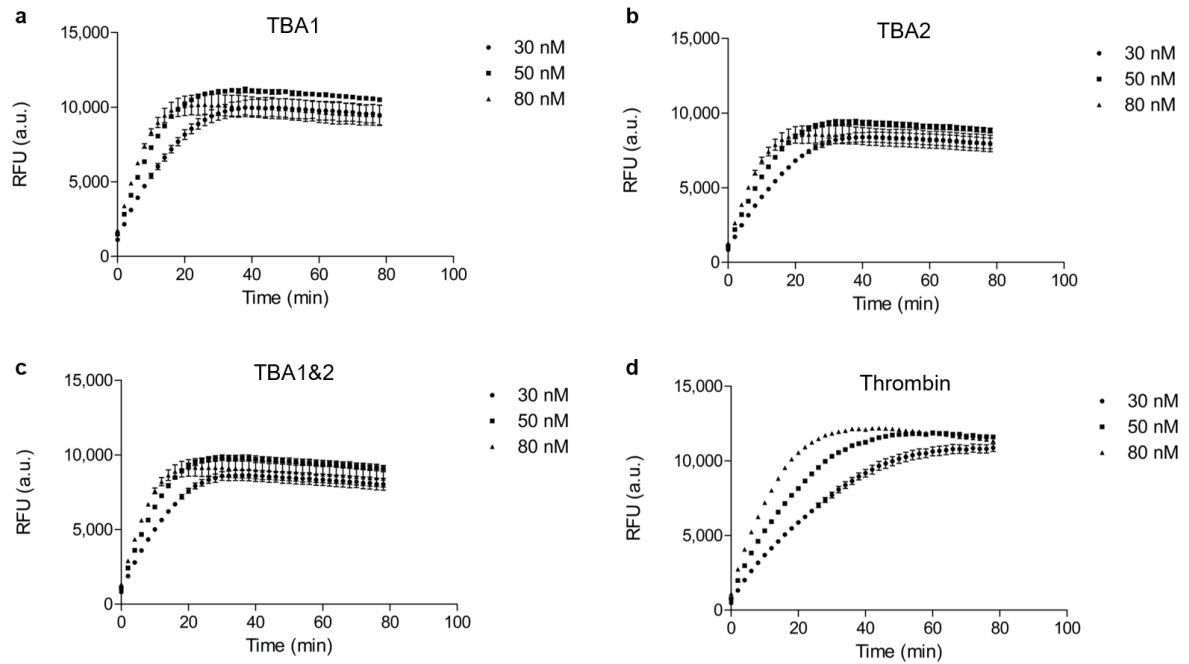


Figure E-8: FAM fluorescence emission intensities for different thrombin concentrations (30, 50 and 80 nM) in presence of TBA1 (a), TBA2 (b), TBA1&2 (c) and without any aptamers in solution (d) in 1x TEMg, 100 nM aptamer and 20 μ M substrate.

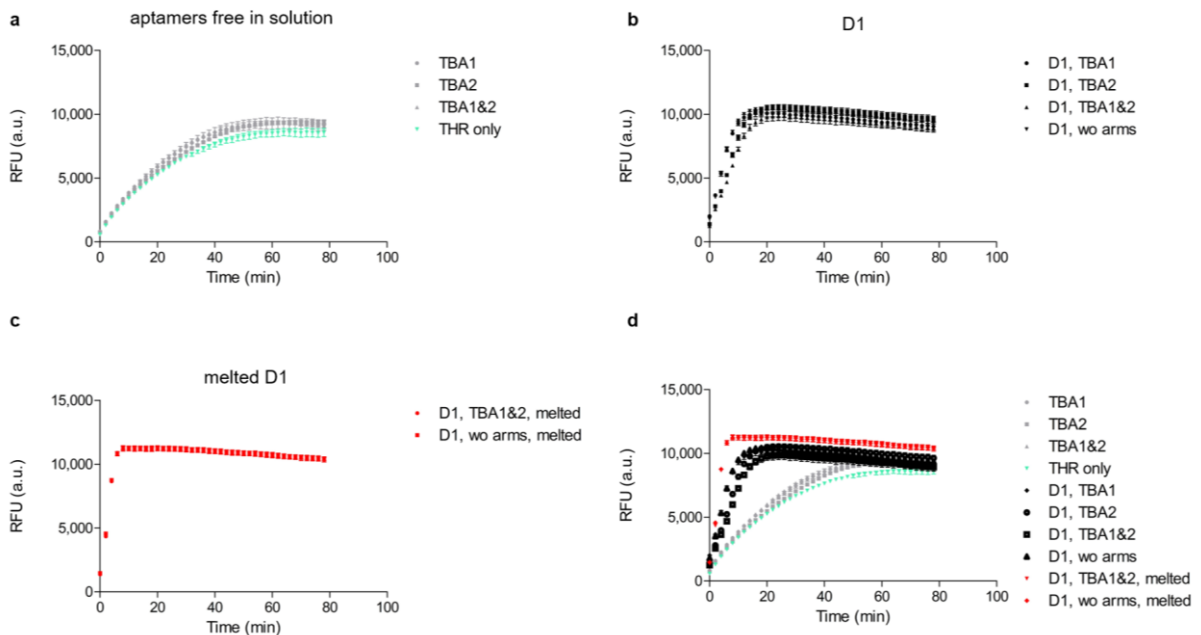


Figure E-9: FAM fluorescence emission intensities representing the proteolytic activity of the tested protein. Evaluated were the free aptamers in solution (a) compared to the protein enveloped in cage D1 (b) and destroyed constructs (c).

Buffer, Media and solutions**Table E-1: Buffer, media and solutions.**

Buffer/Media/Solutions	
2xYT Medium	16 g/l bacto tryptone, 10 g/l bacto yeast extract, 5 g/l NaCl
Blocking solution and antibody dilutant	50 ml TBS-T with 3% BSA
Buffer CA	25% (v/v) isopropanol, 10% (v/v) acetate, 0.05% (w/v) Coomassie R250
Buffer CB	10% (v/v) isopropanol, 10% (v/v) acetate, 0.005% (w/v) Coomassie R250
Buffer CC	10% (v/v) acetate, 0.002% (w/v) Coomassie R250
Buffer CD	10% (v/v) acetate
Guanidine HCl	6 M guanidine HCl pH 1.5
Loading dye for denaturing PAGE	80% formamide (v/v), 20% TBE 5x (v/v)
Loading dye for native PAGE and agarose gelelectrophoresis	70% TBEMg 5x (v/v), 30% glycerol (v/v)
NZA-Medium	10 g/l NZA, 5 g/l bacto yeast extract, 10 g/l NaCl
PBS (1x)	3.5 mM NaH ₂ PO ₄ , 8 mM Na ₂ HPO ₄ , 50 mM NaCl, pH 8.6
PEG precipitation buffer	5 mM tris base, 1 mM EDTA, 505 mM NaCl, 15% (w/v) PEG 8000
SDS PAGE gel-loading buffer	200 mM tris HCl (pH 6.8), 8% SDS, 40% glycerol, 0.004% bromophenolblue, DTT 30 mM
SDS resolving gel buffer (4x)	500 mM tris/HCl (pH= 6.8), 4 g/l SDS
SDS running buffer (1x)	250 mM tris, 950 mM glycine, 5 g/l SDS
SDS stacking gel buffer (4x)	3 M tris base, 4 g/l SDS
Standard I agar	37 g/l Agar
TBE (1x)	89 mM tris base, 89 mM boric acid, 2 mM EDTA, pH 8.0
TBEMg (1x)	40 mM tris base, 20 mM boric acid, 2 mM EDTA, 12.5 mM Mg acetate, pH 8.0
TBS (1x)	30 mM tris base, 150 mM NaCl, pH 7.5
TBS-T	100 ml 10x TBS, 900 ml H ₂ O, 0.1% Tween
TEMg (1x)	20 mM tris base, 2 mM EDTA, 12.5 mM MgCl ₂ , pH 7.6
TEMg KCl (1x)	20 mM tris base, 2 mM EDTA, 12.5 mM MgCl ₂ , 100 mM KCl pH 7.6

Transfer buffer (1x)	100 ml 10x SDS running buffer, 200 ml 100% MeOH, 700 ml H ₂ O
Tris A- buffer	50 mM Tris, 500 mM saccharose, pH 8.0
Tris B- buffer	50 mM Tris, 1 mM EDTA, pH 8.0

Chemicals & miscellaneous reagents

Table E-2: Chemicals & miscellaneous reagents.

Chemicals & miscellaneous reagents	Manufacturer
1 kb DNA-ladder + gel loading buffer	Carl Roth GmbH + Co. KG
10 bp DNA- ladder + gel loading buffer	GeneOn GmbH
2-Mercaptoethanol	Sigma-Aldrich Co. LLC.
Acrylamide/bis solution (37.5:1; 30% w/v)	Sigma-Aldrich Co. LLC.
Acrylamide/bis solution (19:1; 40% w/v)	Sigma-Aldrich Co. LLC.
Agarose	Biozym
Ampicillin	Sigma-Aldrich Co. LLC.
Ammonium persulfate (APS)	Sigma-Aldrich Co. LLC.
Ammonium sulfate ((NH₄)₂SO₄)	Sigma-Aldrich Co. LLC.
Aqua dest.	Milli-Q® Integral Water Purification System (cat. # Z00QSVC01)
Argon	AIR LIQUIDE Deutschland GmbH
AssayMix qRT-PCR	Thermo Fisher Scientific
Bacto Tryptone	Becton, Dickinson and Company
Bacto Yeast Extract	Becton, Dickinson and Company
Boric acid	Sigma-Aldrich Co. LLC.
Bovine serum albumin (BSA)	Sigma-Aldrich Co. LLC., VWR
Bromophenol blue sodium salt	Sigma-Aldrich Co. LLC.
Chloramphenicol	Sigma-Aldrich Co. LLC.
Cyanin-3 ester	Lumiprobe GmbH

Cyanin-5 ester	Lumiprobe GmbH
Dimethylsulfoxid (DMSO), puriss. p.a., ACS reagent, ≥ 99.9%	Sigma-Aldrich Co. LLC.
Disodium phosphate (Na₂HPO₄*2H₂O)	Sigma-Aldrich Co. LLC.
Ethanol 99,9 %; denatured	W. Hoffmann GmbH, Düsseldorf, Germany
Ethanol p.a. 99,9 %	Merck KGaA
Ethidium bromide, for molecular biology	Merck KGaA
Ethylenediamine tetraacetic acid disodium salt dihydrate (EDTA)	Sigma-Aldrich Co. LLC.
Fluorescein isothiocyanate (FITC)- ester	Thermo Fisher Scientific
Glycerin	Sigma-Aldrich Co. LLC.
Glycine	Sigma-Aldrich Co. LLC.
Guanidinium chloride	Sigma-Aldrich Co. LLC.
HCl adjust pH	Bernd Kraft GmbH
Isopropanol	Sigma-Aldrich Co. LLC.
Isopropyl-β-D-thiogalactopyranosid (IPTG)	Sigma-Aldrich Co. LLC.
Lysis-Buffer (0.2 M NaOH, 1% SDS)	Macherey-Nagel
M13mp18 phage genome	Affymetrix
Magnesium acetate tetrahydrate	Sigma-Aldrich Co. LLC.
Magnesium chloride hexahydrate	Sigma-Aldrich Co. LLC.
Mastermix qRTPCR	Thermo Fisher Scientific
Monopotassium phosphate (KH₂PO₄)	Sigma-Aldrich Co. LLC.
NaOH adjust pH	Sigma-Aldrich Co. LLC.
Neutralization-Buffer (3 M KOAc pH 5.5)	Macherey-Nagel KIT
N-Z-Amine	Sigma-Aldrich Co. LLC.
Polyethylene glycol 8000	Sigma-Aldrich Co. LLC.
Potassium chloride	Sigma-Aldrich Co. LLC.
Saccharose	Sigma-Aldrich Co. LLC.
Sodium chloride	Carl Roth GmbH + Co. KG

Sodium dodecyl sulfate (SDS)	Sigma-Aldrich Co. LLC.
Spectra™ Multicolor Low Range Protein Ladder	Thermo Fisher Scientific
Standard I Agar	Merck KGaA
SYBR Gold nucleic acid gel staining	Thermo Fisher Scientific
Tetracycline	Sigma-Aldrich Co. LLC.
Tetramethylethylenediamine (TEMED)	Sigma-Aldrich Co. LLC.
Tris(hydroxymethyl)aminomethane	Sigma-Aldrich Co. LLC.
TritonX	Sigma-Aldrich Co. LLC.
Tween	Sigma-Aldrich Co. LLC.
X-gal [100µg/ml]	Sigma-Aldrich Co. LLC.

Cells, plasmids, antibodies and enzymes

Table E-3: Cells, plasmids, antibodies & enzymes.

Cells, plasmids, antibodies & enzymes	Manufacturer
Benzonase (<i>Serratia marcescens</i>-endonuclease, EC 3.1.30.2)	Roche Deutschland Holding GmbH
E.coli BL21	Sigma-Aldrich Co. LLC.
E.coli DH5α	Thermo Fisher Scientific
human α-Thrombin	Cayman Chemical Company
m13mp18	Affymetrix
pTSA-13	Addgene
Streptavidin peroxidase	Sigma-Aldrich Co. LLC.
XL1-Blue <i>E.coli</i> bacteria	Agilent Technologies

Full lists of DNA sequences (table e-4 to table e-13)*Table E-4: DNA origami left side of the structure.*

Oligoname	Sequence (5'- 3')
B-12,35	CTTCCAGTGCTAAACAACCTTTCAAGGCTTGC
B-12,67	ATAGTTAGGAGAATAGAAAGGAACCGCCCACG
B-12,99	ACAACGCCAATAATAATTTTTTTCACCGATAGT
B-12,131	CGTAACACAAAAAAGGCTCCAAAACCTTTCGAG
B-32,35	AGGGAGTTCAGCGAAAGACAGCATTTCGAAATC
B-32,67	CATAACCGACGGCTACAGAGGCTTCGGAGATT
B-32,99	TGCGCCGATTTTCATGAGGAAGTTTAGCGATTA
B-32,131	GTGAATTTATACGTAATGCCACTAAGAATACA
B-52,35	CGCGACCTACGGTCAATCATAAGGTGTGAATT
B-52,67	TGTATCATCTTTGAAAGAGGACAGGCTTGAGA
B-52,99	TACCAAGCCCAGGCGCATAGGCTGGACGAGAA
B-52,131	CTAAAACAAGTAATCTTGACAAGAAAGCTGCT
B-72,35	ACCTTATGGGACGTTGGGAAGAAAATAGTAAA
B-72,67	TGTTTTAAACGAACCTAACGGAACACTTTTGCA
B-72,99	ACACCAGAAAAGATTCATCAGTTGCAGACGAC
B-72,131	CATTCAGTCATTCAACTAATGCAGGTAAGAGCAACAC TATC
B-92,35	ATGTTTAGTAAATATTCATTGAATTCAAAGCG
B-92,67	AAAGAAGTAAACAGTTCAGAAAACAAGACTTC
B-92,99	GATAAAAACAAAATCAGGTCTTTGATTGCAT
B-112,35	AACCAGACAGTACCTTTAATTGCTGTTTGACC
B-112,67	AAATATCGCATTTTTTGCGGATGGCTTGATTCC
B-112,99	CAAAAAGAGAATATAATGCTGTAGACGGTGTC
B-132,35	ATTAGATAATATTTTCATTTGGGGTTTGCGGG
B-132,67	CAATTCTGGGCATCAATTCTACTATTGTACCA

B-132,99	TGGAAGTTCATCCAATAAATCATACAATAAAG
B-152,35	AGAAGCCTCCCTCATATATTTTAATTGCCTGA
B-152,67	AAAACATTATGTGTAGGTAAAGATTTTTTGAG
B-152,99	CCTCAGAGGGCCGGAGACAGTCAAAGCTGATA
B-172,35	GAGTCTGGAAAAGTAGCATGTCAAGATTCTCC
B-172,67	AGATCTACTGATAATCAGAAAAGCAACATTAA
B-172,99	AATTAATGTTGTATAAGCAAATATCGCGTCTG
B-178,123	TAATATTTTGTTAAAATTTTAACCA
B-192,35	GTGGGAACCGTTGGTGTAGATGGGGGGTAACG
B-192,67	ATGTGAGCATCTGCCAGTTTGAGGGAAAGGGG
B-192,99	GCCTTCCTGGCCTCAGGAAGATCGGTGCGGGC
B-192,131	ATAGGAACCCGGCACCGCTTCTGGTCAGGCTG
B-212,35	CCAGGGTTGTGCCAAGCTTGCATGCATTAATG
B-212,67	GATGTGCTAGAGGATCCCCGGTACTTTCCAG
B-212,99	CTCTTCGCAATCATGGTCATAGCTACTCACAT
B-212,131	CGCAACTGTGTTATCCGCTCACAATGTAAAGC
B-232,35	AATCGGCCCGCCAGGGTGGTTTTTAACGTCAA
B-232,67	TCGGGAAACGGGCAACAGCTGATTACAAGAGT
B-232,99	TAATTGCGCCCTGAGAGAGTTGCACGAGATAG
B-232,131	CTGGGGTGGGTTTGCCCCAGCAGGGGCAAAT
B-252,35	AGGGCGAAGAACCATCACCCAAATCAAGTTTT
B-252,67	CCACTATTGAGGTGCCGTAAAGCACTAAATCG
B-252,99	GGTTGAGTAAGGGAGCCCCGATTTAGAGCTT
B-252,131	CCCTTATAAAGCCGGCGAACGTGGCGAGAAAG
G-18,20	TGGGATTTACGTTAGTAAATGAATTT
G-18,52	AGCGGAGTCGTAACGATCTAAAGTTTTGTCGT
G-18,84	GAATTGCGTGTAGCATTCCACAGACAGCCCTC

G-18,116	ATCTCCAATGAGTTTCGTCAACCAGTACAAACT
G-38,20	ACCCTCAGAAAGGCCGCTTTTTCGTTTTTTTTCTGTA
G-38,52	GGGTAGCAATATATTCGGTCGCTGACAGTTTC
G-38,84	AAAGACTTCAATGACAACAACCATAACTAAAG
G-38,116	CGGGTAAACTTAAACAGCTTGATACGTTGAAA
G-58,20	AGGCGCAGGCTCCATGTTACTTAGTTTTTGGATCGTC
G-58,52	CTGACCAACGCCTGATAAATTGTGCGGAACGA
G-58,84	TGTACAGAGCGAAACAAAGTACAATGAGGACT
G-58,116	TCATCAAGCTCATCTTTGACCCCCCATTA
G-78,20	ACCAGTCACGATTTTAAGAAGTGGTTTTTCCGGAACG
G-78,52	TTAATAAATTTCAACTTTAATCATGAACCGAA
G-78,84	ACAGGTAGACGAGTAGTAAATTGGATGAACGG
G-78,116	GAATACCAGAATAAGGCTTGCCCTGCTGACCT
G-98,20	AATCGTCAACTGGATAGCGTCCAATTTTTCTCATTAT
G-98,52	AATGCTTTTTTGCCAGAGGGGGTAAATCTACG
G-98,84	CCATAAATCCAAAATAGCGAGAGGACATTATT
G-98,116	TATTATAATAACCCTCGTTTACAGATTTAG
G-118,20	GATTAGAGCGGAAGCAAACCTCCAATTTTTACTGCGG
G-118,52	TAAGAGGTCGTTTTAATTCGAGCTCCCCCTCA
G-118,84	TAATTGCTTTAAGAGGAAGCCCGAGAGAATGA
G-118,116	GTTTTAAGTCAGAAGCAAAGCGACCCTGAC
G-138,20	GTTTAGCTCATTTCGCAAATGGTCTTTTTCAGGTCAG
G-138,52	GAAAAGGTCGAACGAGTAGATTTACTTTTGA
G-138,84	AGCATTAAATCATTCCATATAACAGTTAGAGCT
G-138,116	GCAAAGAATATGCAACTAAAGTCTCAACAT
G-158,20	TTTTAGAATTATTTCAACGCAAGGTTTTTAATAACCT
G-158,52	CCTGAGTAATGACCCTGTAATACTCGCGAGCT

G-158,84	GTGAGAAACATAAAGCTAAATCGGATAGTAGT
G-158,116	CAATATGATTAGCAAAATTAAGCAGGCAAG
G-178,20	GTAATCGTAGCAAACAAGAGAATCTTTTTATAAAAAT
G-178,52	ACCCCGGTAAAGGCTATCAGGTCAATGCAATG
G-178,84	CAGGAAGACCGGAGAGGGTAGCTATCAAAGG
G-178,116	TAAACGTATATTCAACCGTTCTATCACCAT
G-198,20	ATAGGTCAAACGGCGGATTGACCTTTTTGATGAACG
G-198,52	AACCGTGCGAGTAACAACCCGTCGTCATATGT
G-198,84	ACAGTATCGTAGCCAGCTTTCATCCCCAAAAA
G-198,116	CCAGCTTTGCCATCAAAAATAATTTTAAATTG
G-218,20	GACGGCCATTCCCAGTCACGACGTTTTTTGTAATGG G
G-218,52	TCGACTCTGCAAGGCGATTAAGTTCGCATCGT
G-218,84	GAATTCGTTATTACGCCAGCTGGCGGACGACG
G-218,116	TGTGAAATTTGGGAAGGGCGATCGCACTCCAG
G-238,20	GTATTGGGAACGCGCGGGGAGAGGTTTTTTGTAAAA C
G-238,52	CAGTGAGACCTGTCGTGCCAGCTGCCTGCAGG
G-238,84	CCGCCTGGTTGCGCTCACTGCCCGCCGAGCTC
G-238,116	TCCACGCTCCTAATGAGTGAGCTAGTTTCCTG
G-258,52	TTGGGGTCAAAGAACGTGGACTCCCTTTTCAC
G-258,84	GAACCCTAGTTGTTCCAGTTTGGAGCCCTTCA
G-258,116	GACGGGGAAATCAAAGAATAGCCGCAAGCGG
G-262,12	TTCGATGGCCCACTACGTAAACCGTCTATCAGGGTTT TTCGGTTTGC

Table E-5: DNA origami right side of the structure.

Oligoname	Sequence (5'- 3')
B-18,180P	ATCCTCATTAGCGGGGTTTTGCTCAGTACCA
B-18,212P	CTCTGAATGAGGCTGAGACTCCTCAAGAGAAG
B-18,244P	ATGGCTTTGAACCTATTATTCTGAAACATGAA
B-18,276P	ATAAGTTTGTATAAACAGTTAATGCCCCCTGC
B-38,180P	AGTAGCGATTGACAGGAGTTGAGACAAATAA
B-38,212P	CAGACTGTCACCAGAACCACCACCAGCGCAGT
B-38,244P	GTCATAGCGCCACCCTCAGAGCCACGTCATAC
B-38,276P	TTCATAATCCGCCTCCCTCAGAGCTACTGGTA
B-58,180P	GGTGGCAACCATTAGCAAGGCCGGCCGTAATC
B-58,212P	CACGGAATTAGAGCCAGCAAATCTTTAGCGT
B-58,244P	GAAAATTCATCACCGTCACCGACTCATTTCG
B-58,276P	AAAAGGGCTATTGACGGAAATTATGCCATCTT
B-78,180P	GGAGAATTGATTAAGACTCCTTATTACATAAA
B-78,212P	GAGGGTAAAATAATAACGGAATACAAAGACAC
B-78,244P	ACCCACAAACAAAGTTACCAGAAGAATCAATA
B-78,276P	GAGCAAGAGCCCTTTTTAAGAAAACCAAAGAC
B-92,187P	GAAAATAGCAGCCTTTATTAGACG
B-98,212P	CGAACCTCTAAGAAACGATTTTTTCAAAGTCA
B-98,244P	CTTAAATCATAAACAGCCATATTAGAGAGATA
B-98,276P	AGCTACAAGTCTTTCCAGAGCCTAAATAATAA
B-118,212P	AAGAAAAAAGCAAATCAGATATACGTTTTAG
B-118,244P	CATGTAGATCATCGTAGGAATCATTTTGAAGC
B-118,276P	TCCTTATCACTCATCGAGAACAAGTTGCACCC
B-138,212P	TTCTTACCACATGTTCCAGCTAATGTCCTGAAC
B-138,244P	AGGGCTTAAAGTAATTCTGTCCAGTTTACGAG

B-138,276P	CGCCAACAAATAAGAGAATATAAAGCTGTCTT
B-158,212P	TAGGTTGGCACCCGAATCATAATTTATACAAA
B-158,244P	GATGCAAAGTGTGATAAATAAGGCTCAACAGT
B-158,276P	AGAAAAGCTTGACCTAAATTTAATGTTTAACAA
B-178,212P	ATTACATTAATAGTGAATTTATCACTCCGGCT
B-178,244P	TTTTAATGCGATAGCTTAGATTAATAAATGCT
B-178,276P	GTGAGTGATTAATTTTCCCTTAGAAGAACGCG
B-198,180P	CATATTCAGTTACAAAATCGCGCAAAGAAGATGATG AA
B-198,212P	TCAATATAATAACGGATTCGCCTGCAAATA
B-198,244P	CTGAATAACAGTAACAGTACCTTTATTACCTT
B-198,276P	CAAATTATAGATTTTCAGGTTTACAATATAT
B-218,180P	CTTGCTGAAGTAACATTATCATTTATTATCAT
B-218,212P	AATATCTGTTTGCCCGAACGTTATGCAATTCA
B-218,244P	AAGGAATTTTACAAACAATTCGACTTATACTT
B-218,276P	TAGGAGCATAATACATTTGAGGATTACCATAT
B-238,180P	TTACATTGGCCTGCAACAGTGCCAAGCATCAC
B-238,212P	GTAATAAAAAAACAGAGGTGAGGCCCTCAATC
B-238,244P	AGAACCCTTAAAAATACCGAACGAACAGTTGA
B-238,276P	GTGGCACATGCGCGAACTGATAGCAATATCTT
B-258,180P	ACAGGAGGAAAAACGCTCATGGAATGGATTAT
B-258,212P	AACGGTACAGAACAATATTACCGCCACGACCA
B-258,244P	ATAATCAGAACTCAAATATCGGCACAGAGAT
B-258,276P	GTCCATCAATTAGTAATAACATCAAAGAATAC
G-8,299P	TTTTGAGTAACAGTGCCCTAACGGGGTCAGTGCCTTTT TAGAGCCAC
G-12,195P	GATTAGGATAAAGCCAGAATGGAAAGAGCCGC
G-12,227P	AGTATTAATTACCGTTCCAGTAAGCCACCCTC
G-12,259P	CTATTTTCGTGATGATACAGGAGTGCGCCACCC

G-32,195P	CGCCAGCACAGAATCAAGTTTGCCACCAGTAG
G-32,227P	AGAGCCGCAGCGCGTTTTTCATCGGTGAGCCAT
G-32,259P	TCAGAACCCCCCTTATTAGCGTTTTTCATTAAA
G-32,291P	CACCGGAACAAAATCACCGGAACCTTTTTAGGGAGGG
G-52,195P	CACCATTACATATAAAAGAAACGCCCAAAGA
G-52,227P	TTGGGAATAAGTTTATTTTGTACGAAACCGA
G-52,259P	GGTGAATTATATGGTTTACCAGCGGTAAGCAG
G-52,291P	AAGGTAAAGACATTCAACCGATTGTTTTTTAGCTATC
G-72,195P	ACTGGCATAACTGAACACCCTGAAGTTTAACG
G-72,227P	GGAAACGCTTGAGCGCTAATATCATTTATCCC
G-72,259P	ATAGCCGAGAATTGAGTTAAGCCCATTTGCCA
G-72,291P	TTACCGAAAACAATGAAATAGCAATTTTTACCAACGC
G-92,195P	TCAAAAATTTCTAAGAACGCGAGGGAAGGCTT
G-92,227P	AATCCAAACCGACTTGCGGGAGGTTACCGCGC
G-92,259P	GTTACAAAAAGATTAGTTGCTATTCAAGCCGT
G-92,291P	TAACGAGCTTTTATCCTGAATCTTTTTTTTTAAACCA
G-112,195P	ATCCGGTAATCAACAATAGATAAGCAGAACGC
G-112,227P	CCAATAGCTAATATCCCATCCTAACGACGAC
G-112,259P	TTTTATTTAACCAATCAATAATCGGTACCGAC
G-112,291P	AGTACCGCATTCCAAGAACGGTATTTTTGCATTTTC
G-132,195p	GCCTGTTTTTAGTATCATATGCGTACTAGAAA
G-132,227P	AATAACAAGTATAAAGCCAACGCGTTAAATA
G-132,259P	AAAAGGTAATTGAGAATCGCCATAGTTTGAAA
G-132,291P	GAGCCAGTTGTAATTTAGGCAGAGTTTTTAGTTAATT
G-152,195P	AAGCCTGTAGACTACCTTTTTAACAAATCATA
G-152,227P	AGAATAAAGTTATATAACTATATGGACGCTGA
G-152,259P	TACCGACCTCCAATCGCAAGACAAATCCTTGA

G-152,291P	TCATCTTCTTTTCAAATATATTTTTTTTTTAAATCGTC
G-172,195P	GGTCTGAGACAAACATCAAGAAAAATTGCTTT
G-172,227P	GAAGAGTCTAACAATTCATTTGATACATCGG
G-172,259P	AAACATAGGAAACAGTACATAAATACGTCAGA
G-172,291P	GCTATTAATAACCTTGCTTCTGTTTTTTAAATAAAG
G-192,195P	GAATACCATGATTATCAGATGATGTAATTTTA
G-192,227P	GAGAAACAATCCTGATTGTTTGGAAACTCGTA
G-192,259P	TGAATATATGGAAGGTTAGAACCTTAGAAGT
G-192,291P	AAATTGCGTTTGCACGTAAAACAGTTTTTTAGAGCCG
G-212,195P	AAAGTTTGACCTCAAATATCAAACGGTCAGTA
G-212,227P	TTAAATCCGTCAGTTGGCAAATCAACCACCAG
G-212,259P	ATTAGACTGAGGAAGGTTATCTAACCTAAAAC
G-212,291P	TCAATAGACTAACAATAATAGATTTTTTTGGCTATTA
G-232,195P	TTAACACCGCAGATTCACCAGTCACAGCCATT
G-232,227P	CAGAAGATAGGGACATTCTGGCCACTTGCTGG
G-232,259P	ATCGCCATTCTGACCTGAAAGCGTCTTGCCTG
G-232,291P	GTCTTTAAGACAATATTTTTGAATTTTTTTAGCAATA
G-252,195P	GCAACAGGCCGATTAAAGGGATTTTAGACAGG
G-252,227P	TAATATCCGCCAGAATCCTGAGAAGTGTTTTT
G-252,259P	AGTAGAAGTGAGGCCACCGAGTAAAAGAGTCT
G-252,291P	CTTCTTTGCGCAAATTAACCGTTGTT

Table E-6: List of the oligonucleotides used for modification of the seam in construct I.

n°	Oligoname	Sequence (5'- 3')
2	LG18,148P	TAATTGTATTTCCCCCTTTTTGGGGGTTTGCCTTGATATTCACAAGCAG GTCA
4	LG38,148P	CCAACCTATTTCCCCCTTTTTGGGGGTTTACCATCGATAGCAGCAAAC GTCA
6	LG58,148P	TTCATTACTTTCCCCCTTTTTGGGGGTTTAAACGTAGAAAATACATACG CAGT
8	LG78,148P	CGCCAAAATTTCCCCCTTTTTGGGGGTTTAAAACAGGGAAGCGCACA GAGAG
10	LG178,148P	AATTTTTGTTTCCCCCTTTTTGGGGGTTTTTCAATTACCTGAGCAGAG GCGA
12	LG198,148P	ACCAGGCATTTCCCCCTTTTTGGGGGTTTCACCAGAAGGAGCGGATGC GGAAC
14	LG218,148P	AACATACGTTTCCCCCTTTTTGGGGGTTTCAAATGAAAAATCTAACGCT GAGA
16	LG238,148P	CTGTTTGATTTCCCCCTTTTTGGGGGTTTGCTCAATCGTCTGAAAATAC CTAC
18	LG258,148P	GAAGGGAATTTCCCCCTTTTTGGGGGTTTCGTTAGAATCAGAGCGGGA GCTAA
1	LG12,163P	GGCGGATATTTCCCCCTTTTTGGGGGTTTCAAGCCAATAGGAACCCA TGTAC
3	LG32,163P	GACGATTGTTTCCCCCTTTTTGGGGGTTTTCGGTTTATCAGCTTGGA GCCTT
5	LG52,163P	CCAATGAATTTCCCCCTTTTTGGGGGTTTAAACGAAAGAGGCAAACGA AGGCA
7	LG72,163P	ATGTTAGCTTTCCCCCTTTTTGGGGGTTTCAAATCAACGTAACAACCG GATA
9	LG92,163P	AATAACATTTTCCCCCTTTTTGGGGGTTTGAATTACGAGGCATAATAC ATAA
11	LG192,163P	ATTATTCATTTCCCCCTTTTTGGGGGTTTTTAATCAGCTCATTTTCGCA TTA
13	LG212,163P	AAAGAACTTTCCCCCTTTTTGGGGGTTTAAAGCGCCATTCGCCATTGC CGGAA
15	LG232,163P	GCCAGCAGTTTCCCCCTTTTTGGGGGTTTAGCCGGAAGCATAAAGTTC CACAC
17	LG252,163P	ATTTTGACTTTCCCCCTTTTTGGGGGTTTGGTGGTTCCGAAATCCGAA AATC

Table E-7: List of the oligonucleotides used for modification of the seam in construct II with inner segment A: 5'-ATCGAACTGGGC-3'.

n°	Oligoname	Sequence (5'- 3')
2	2ILA-1	TAATTGTATTCCCCCTTTTTGGGGGATCGAACTGGGCCCCCCTTTTTG GGGGTTGCCTTGATATTCACAAGCAGGTCA
4	2ILA-2	CCAACCTATTCCCCCTTTTTGGGGGATCGAACTGGGCCCCCCTTTTTG GGGGTTACCATCGATAGCAGCAAACGTCA
6	2ILA-3	TTCATTACTTCCCCCTTTTTGGGGGATCGAACTGGGCCCCCCTTTTTG GGGGTTAAACGTAGAAAATACATACGCAGT
8	2ILA-4	CGCCAAAATTCCCCCTTTTTGGGGGATCGAACTGGGCCCCCCTTTTTG GGGGTTAAAAACAGGGAAGCGCACAGAGAG
10	2ILA-5	AATTTTTGTTCCCCCTTTTTGGGGGATCGAACTGGGCCCCCCTTTTTG GGGGTTTTTCAATTACCTGAGCAGAGGCGA
12	2ILA-6	ACCAGGCATTCCCCCTTTTTGGGGGATCGAACTGGGCCCCCCTTTTTG GGGGTTCACCAGAAGGAGCGGATGCGGAAC
14	2ILA-7	AACATACGTTCCCCCTTTTTGGGGGATCGAACTGGGCCCCCCTTTTTG GGGGTTCAAATGAAAATCTAACGCTGAGA
16	2ILA-8	CTGTTTGATTCCCCCTTTTTGGGGGATCGAACTGGGCCCCCCTTTTTG GGGGTTGCTCAATCGTCTGAAAATACCTAC
18	2ILA-9	GAAGGGAATTCCCCCTTTTTGGGGGATCGAACTGGGCCCCCCTTTTTG GGGGTTCGTTAGAATCAGAGCGGGAGCTAA
1	2ILA-10	GGCGGATATTCCCCCTTTTTGGGGGATCGAACTGGGCCCCCCTTTTTG GGGGTTCAAGCCCAATAGGAACCCATGTAC
3	2ILA-11	GACGATTGTTCCCCCTTTTTGGGGGATCGAACTGGGCCCCCCTTTTTG GGGGTTTCGGTTTATCAGCTTGGGAGCCTT
5	2ILA-12	CCAATGAATTCCCCCTTTTTGGGGGATCGAACTGGGCCCCCCTTTTTG GGGGTTAAACGAAAGAGGCAAACGAAGGCA
7	2ILA-13	ATGTTAGCTTCCCCCTTTTTGGGGGATCGAACTGGGCCCCCCTTTTTG GGGGTTCAAATCAACGTAACAACCGGATA
9	2ILA-14	AATAACATTTCCCCCTTTTTGGGGGATCGAACTGGGCCCCCCTTTTTG GGGGTTGGAATTACGAGGCATAATACATAA
11	2ILA-15	ATTATTCATTCCCCCTTTTTGGGGGATCGAACTGGGCCCCCCTTTTTG GGGGTTTTAAATCAGCTCATTTTCGCATTA
13	2ILA-16	AAAGAACTTCCCCCTTTTTGGGGGATCGAACTGGGCCCCCCTTTTTG GGGGTTAAGCGCCATTCGCCATTGCCGGAA
15	2ILA-17	GCCAGCAGTTCCCCCTTTTTGGGGGATCGAACTGGGCCCCCCTTTTTG GGGGTTAGCCGGAAGCATAAAGTTCCACAC
17	2ILA-18	ATTTTGACTTCCCCCTTTTTGGGGGATCGAACTGGGCCCCCCTTTTTG GGGGTTTGGTGGTCCGAAAATCCGAAAATC

Stabilizing sequence 5'-GCCCAGTTCGAT-3'

Fuel: 5'-C₅A₅G₅CGCG-3'; Antifuel: 5'-CGCGC₅T₅G₅-3'

Table E-8: List of the oligonucleotides used for modification of the seam in construct II with inner sequence B: 5'-CGCTGATGCACT-3'.

n°	Oligo-name	Sequence (5'- 3')
2	2ILB-1	TAATTGTATTCCCCCTTTTTGGGGGCGCTGATGCACTCCCCCTTTTTGGGGGTTG CCTTGATATTCACAAGCAGGTCA
4	2ILB-2	CCAACCTATTCCCCCTTTTTGGGGGCGCTGATGCACTCCCCCTTTTTGGGGGTTA CCATCGATAGCAGCAAAACGTCA
6	2ILB-3	TTCATTACTTCCCCCTTTTTGGGGGCGCTGATGCACTCCCCCTTTTTGGGGGTTA AACGTAGAAAATACATACGCAGT
8	2ILB-4	CGCCAAAATTCCCCCTTTTTGGGGGCGCTGATGCACTCCCCCTTTTTGGGGGTTA AAAACAGGGAAGCGCACAGAGAG
10	2ILB-5	AATTTTTGTTCCCCCTTTTTGGGGGCGCTGATGCACTCCCCCTTTTTGGGGGTTT TTCAATTACCTGAGCAGAGGCGA
12	2ILB-6	ACCAGGCATTCCCCCTTTTTGGGGGCGCTGATGCACTCCCCCTTTTTGGGGGTT CACCAGAAGGAGCGGATGCGGAAC
14	2ILB-7	AACATACGTTCCCCCTTTTTGGGGGCGCTGATGCACTCCCCCTTTTTGGGGGTTT AAATGAAAAATCTAACGCTGAGA
16	2ILB-8	CTGTTTGATTCCCCCTTTTTGGGGGCGCTGATGCACTCCCCCTTTTTGGGGGTTG CTCAATCGTCTGAAAATACCTAC
18	2ILB-9	GAAGGGAATTCCCCCTTTTTGGGGGCGCTGATGCACTCCCCCTTTTTGGGGGTT CGTTAGAATCAGAGCGGGAGCTAA
1	2ILB-10	GGCGGATATTCCCCCTTTTTGGGGGCGCTGATGCACTCCCCCTTTTTGGGGGTT CAAGCCCAATAGGAACCCATGTAC
3	2ILB-11	GACGATTGTTCCCCCTTTTTGGGGGCGCTGATGCACTCCCCCTTTTTGGGGGTTT CGGTTTATCAGCTTGGGAGCCTT
5	2ILB-12	CCAATGAATTCCCCCTTTTTGGGGGCGCTGATGCACTCCCCCTTTTTGGGGGTTA AACGAAAGAGGCAAACGAAGGCA
7	2ILB-13	ATGTTAGCTTCCCCCTTTTTGGGGGCGCTGATGCACTCCCCCTTTTTGGGGGTTT CAAATCAACGTAACAACCGGATA
9	2ILB-14	AATAACATTTCCCCCTTTTTGGGGGCGCTGATGCACTCCCCCTTTTTGGGGGTTG GAATTACGAGGCATAAATACATAA
11	2ILB-15	ATTATTCATTCCCCCTTTTTGGGGGCGCTGATGCACTCCCCCTTTTTGGGGGTTT TAAATCAGCTCATTTTCGCATTA
13	2ILB-16	AAAGAAACTTCCCCCTTTTTGGGGGCGCTGATGCACTCCCCCTTTTTGGGGGTTA AGCGCCATTGCGCATTGCCGGA
15	2ILB-17	GCCAGCAGTTCCCCCTTTTTGGGGGCGCTGATGCACTCCCCCTTTTTGGGGGTT AGCCGGAAGCATAAAGTTCCACAC
17	2ILB-18	ATTTTGAATTCCCCCTTTTTGGGGGCGCTGATGCACTCCCCCTTTTTGGGGGTTT GGTGGTTCCGAAATCCGAAAATC

Stabilizing sequence 5'-AGTGCATCAGCG-3'

Fuel: 5'-C₅A₅G₅CGCG-3'; Antifuel: 5'-CGCGC₅T₅G₅-3'

Table E-9: List of the oligonucleotides used for modification of the seam in construct III with inner sequence B: 5'-CGCTGATGCACT-3'.

n°	Oligoname	Sequence (5'- 3')
2	2DLB-1	TAATTGTATTGCTGCTTTTTGCAGCCGCTGATGCACTCCTCCTTTTTG GAGGTTGCCTTGATATTCACAAGCAGGTCA
4	2DLB-2	CCAACCTATTGCTGCTTTTTGCAGCCGCTGATGCACTCCTCCTTTTTG GAGGTTACCATCGATAGCAGCAAAACGTCA
6	2DLB-3	TTCATTACTTGCTGCTTTTTGCAGCCGCTGATGCACTCCTCCTTTTTG GAGGTTAAACGTAGAAAATACATACGCAGT
8	2DLB-4	CGCCAAAATTGCTGCTTTTTGCAGCCGCTGATGCACTCCTCCTTTTTG GAGGTTAAAACAGGGAAGCGCACAGAGAG
10	2DLB-5	AATTTTTGTTGCTGCTTTTTGCAGCCGCTGATGCACTCCTCCTTTTTG GAGGTTTTTCAATTACCTGAGCAGAGGCCA
12	2DLB-6	ACCAGGCATTGCTGCTTTTTGCAGCCGCTGATGCACTCCTCCTTTTT GGAGGTTACCAGAAGGAGCGGATGCGGAAC
14	2DLB-7	AACATACGTTGCTGCTTTTTGCAGCCGCTGATGCACTCCTCCTTTTTG GAGGTTCAAATGAAAATCTAACGCTGAGA
16	2DLB-8	CTGTTTGATTGCTGCTTTTTGCAGCCGCTGATGCACTCCTCCTTTTTG GAGGTTGCTCAATCGTCTGAAAATACCTAC
18	2DLB-9	GAAGGGAATTGCTGCTTTTTGCAGCCGCTGATGCACTCCTCCTTTTT GGAGGTTTCGTTAGAATCAGAGCGGGAGCTAA
1	2DLB-10	GGCGGATATTGCTGCTTTTTGCAGCCGCTGATGCACTCCTCCTTTTT GGAGGTTCAAGCCCAATAGGAACCCATGTAC
3	2DLB-11	GACGATTGTTGCTGCTTTTTGCAGCCGCTGATGCACTCCTCCTTTTTG GAGGTTTCGGTTTATCAGCTTGGGAGCCTT
5	2DLB-12	CCAATGAATTGCTGCTTTTTGCAGCCGCTGATGCACTCCTCCTTTTTG GAGGTTAAACGAAAGAGGCAACGAAGGCA
7	2DLB-13	ATGTTAGCTTGCTGCTTTTTGCAGCCGCTGATGCACTCCTCCTTTTTG GAGGTTCAAATCAACGTAACAACCGGATA
9	2DLB-14	AATAACATTTGCTGCTTTTTGCAGCCGCTGATGCACTCCTCCTTTTTG GAGGTTGGAATTACGAGGCATAATACATAA
11	2DLB-15	ATTATTCATTGCTGCTTTTTGCAGCCGCTGATGCACTCCTCCTTTTTG GAGGTTTTAAATCAGCTCATTTTTCGCATT
13	2DLB-16	AAAGAACTTGCTGCTTTTTGCAGCCGCTGATGCACTCCTCCTTTTTG GAGGTTAAGCGCCATTGCGCCATTGCCGGAA
15	2DLB-17	GCCAGCAGTTGCTGCTTTTTGCAGCCGCTGATGCACTCCTCCTTTTT GGAGGTTAGCCGGAAGCATAAAGTTCCACAC
17	2DLB-18	ATTTGACTTGCTGCTTTTTGCAGCCGCTGATGCACTCCTCCTTTTTG GAGGTTTGGTGGTTCCGAAATCCGAAAATC

Stabilizing sequence B: 5'-AGTGCATCAGCG-3'

FAM-Fuel1: 5'-FAM-CCTCCA₅GGAGG-ATTCGAGCTC-3'

TAMRA-Fuel2: 5'-TAMRA-GCTGCA₅GCAGC-CAGA₃TGGC-3'

AntiFuel1: 5'-GAGCTCGAAT-CCTCCT₅GGAGG-3'

AntiFuel2: 5'-GCCAT₃CTG-GCTGCT₅GCAG-3'

Table E-10: List of the oligonucleotides used for FRET analysis of the hairpin motifs of construct I.

n°	Oligoname	Sequence (5'- 3')
4	loop4-TAMRA	CCAACCTATTTCCCCCTTTTTGGGGGTTTACCATCGATAGCAGCAA CGTCACCAATGAA-[TAMRA]
5	FAM-loop5	[FAM]-AAACGAAAGAGGCAAACGAAGGCA
8	loop8-TAMRA	CGCCAAAATTTCCCCCTTTTTGGGGGTTTAAAAACAGGGAAGCGCA CGAGAGAATAACAT-[TAMRA]
9	FAM-loop9	[FAM]-GGAATTACGAGGCATAATACATAA
14	loop14-TAMRA	AACATACGTTTCCCCCTTTTTGGGGGTTTCAAATGAAAAATCTAACG CTGAGAGCCAGCAG-[TAMRA]
15	FAM-loop15	[FAM]-AGCCGGAAGCATAAAGTTCCACAC
--	FAM_G138,52	[FAM]-GAAAAGGTCTGAACGAGTAGATTTACCTTTTGA
--	G158,52_TAMRA	CCTGAGTAATGACCCTGTAATACTCGCGAGCT-[TAMRA]
18R	TAMRA-loop18_right	[TAMRA]-CGTTAGAATCAGAGCGGGAGCTAA
18L	loop18_left-FAM	CCCTTATAAAGCCGGCGAACGTGGCGAGAAAGGAAGGGAA-[FAM]
4	no_loop4-TAMRA	CCAACCTAACCATCGATAGCAGCAAACGTCACCAATGAA-[TAMRA]
14	no_loop14-TAMRA	AACATACGCAAATGAAAAATCTAACGCTGAGAGCCAGCAG-[TAMRA]

Table E-11: List of the oligonucleotides used for FRET analysis of the hairpin motifs of construct II and III.

n°	Oligoname	Sequence (5'- 3')
4	loop4-2i-B-TAMRA	CCAACCTATTCCCCCTTTTTGGGGGCGCTGATGCACTCCCCCTTTTT GGGGGTTACCATCGATAGCAGCAAACGTCACCAATGAA-[TAMRA]
4	loop4-2d-B-TAMRA	CCAACCTATTGCTGCTTTTTGCAGCCGCTGATGCACTCCTCCTTTTT GGAGGTTACCATCGATAGCAGCAAACGTCACCAATGAA-[TAMRA]
5	FAM-loop5	[FAM]-AAACGAAAGAGGCAAACGAAGGCA

Table E-12: List of oligonucleotides for FRET tag-of-war analysis of construct I.

Oligoname	Sequence (5'- 3')
FAM-G-138_G4L	[FAM]-TGGTGGTGGTGGTGGTGGTGGATATGCAACTAAAGTCTCAACAT
21-G4T4G4_L	CCACCACCACCACCACCAGGGGTTTTGGGG
21-G4T4G4-R	CAACAACAACAACAACAAGGGGTTTTGGGG
21-G4T4G4-TAMRA	CCACCACCACCACCACCAGGGGTTTTGGGG[TAMRA]

Table E-13: List of oligonucleotides for inner cavity modifications for thrombin encapsulation of construct I.

Oligoname	Sequence (5'- 3')
pA_D0-L1	ACAACAACATATGCAACTAAAGTCTCAACAT
pA_D0-L2	CAATATGATTAGCAAATAAGCAGGCAAGGCAAAGATAACAACAA
pA_D0-R1	ATCCGGTAATCAACAATAGATAAGCAGAACGCGCCTGTTTTGATGATG
pA_D0-R2	GATGATGATTAGTATCATATGCGTACTAGAAA
pA_D1,2,3-L1	ATATGCAACTAAAGTCTCAACAT
pA_D2-L2	CAATATGATTAGCAAATAAGCAGGCAAGGCAAAGATAACAACAACAA CAACAACAA
pA_D1,3-L2	CAATATGATTAGCAAATAAGCAGGCAAGGCAAAGATAACAACAACAA CAACAA
pA_D1,2,3-R1	ATCCGGTAATCAACAATAGATAAGCAGAACACACCTGTTT
pA_D2-R2	GATGATGATGATGATGATGATGTTAGTAGTATCATATGAGTACTAGAAA
pA_D1,3-R2	GATGATGATGATGATGTTAGTATCATATGCGTACTAGAAA
th_TBA1 D0,1,2	GGTTGGTGTGGTTGGTTGTTGTTGTTGTTGTCGGTAAAGAC
th_TBA1_FLC D0,1,2	GGTTGGTGTGGTTGG[FAMT]TGTTGTTGTTGTTGTCGGTAAAGAC
th_TBA1_FLC_TAMRA D0,1,2	[TAMRA]-GGTTGGTGTGGTTGG[FAMT]TGTTGTTGTTGTTGTCGGTAAAGAC
th_TBA2 D0,1,2	CTCGAGCTTACATCATCATCATCAGTCCGTGGTAGGGCAGGTTGGGG TGACT
th_TBA2_FLC D0,1,2	CTCGAGCTTACATCATCATCATCAG[FAMT]TCCGTGGTAGGGCAGGTT GGGGTGACT
th_TBA2_FLC_TAMRA D0,1,2	CTCGAGCTTACATCATCATCATCAG[FAMT]TCCGTGGTAGGGCAGGTT GGGGTGACT-[TAMRA]
cth_TBA1 D0,1,2	GTCTTTACCGACAACAACAACAACCAACCACACCAACC

cth_TB2 D0,1,2	AGTCACCCCAACCTGCCCTACCACGGACTGATGATGATGATGATGTAAGCTCGAG
FAM-TBA1 D0,1,2	[FAM]-GGTTGGTGTGGTTGGTTGTTGTTGTTGTTGT
TBA1 D0,1,2	GGTTGGTGTGGTTGGTTGTTGTTGTTGTTGT
TBA2-TRAMRA D0,1,2	CATCATCATCATCATCAGTCCGTGGTAGGGCAGGTTGGGGTGACT-[TAMRA]
TBA2 D0,1,2	CATCATCATCATCATCAGTCCGTGGTAGGGCAGGTTGGGGTGACT
TBA1-long spacer D3	GGTTGGTGTGGTTGGTTTTTTTTTTTTTTTTTTTTTTTTTTGTTGTTGTTGTTGT
FAM-TBA1-long spacer D3	[FAM]-GGTTGGTGTGGTTGGTTTTTTTTTTTTTTTTTTTTTTTTTTGTTGTTGTTGTTGT
TBA1-short spacer D3	GGTTGGTGTGGTTGGTTTTTTTTTTTTTTTTTTTTTTTTTTGTTGTTGTTGTTGT
FAM-TBA1-short spacer D3	[FAM]-GGTTGGTGTGGTTGGTTTTTTTTTTTTTTTTTTTTTTTTTTGTTGTTGTTGTTGT

Table E-14: List of primers for m13mp18 sequencing.

Oligoname	Sequence (5' - 3')
primer_1	CGTAAAGCACTAAATCGGAACCCT
primer_2	TCACTGCCCGCTTTCCA
primer_3	GTTTTCCCAGTCACGACGTTGTAA
primer_4	GAAAAGCCCCAAAAACAGGAAGAT
primer_5	ATCATACAGGCAAGGCAAAGAATT
primer_6	AAAAAGATTAAGAGGAAGCCCGAA
primer_7	CGATAAAAACCAAAATAGCGAGAG
primer_8	TTGACCCCCAGCGATTATACCA
primer_9	TGACAACAACCATCGCCAC
primer_10	ATAAGTGCCGTCGAGAGGGTTG
primer_11	CATAATCAAATCACCGGAACCAG
primer_12	GAAACCGAGGAAACGCAATAATAA
primer_13	GACTTGCGGGAGGTTTTGAA
primer_14	CAAGACAAAGAACGCGAGAAAAC
primer_15	CCTGAGCAAAGAAGATGATGAAA

primer_16	ACCTCAAATATCAAACCCTCAATC
primer_17	GTCCATCACGCAAATTAACCG

All scaffold batches were directly sequenced after production to verify no divergence to the reference sequence used as basement for all designs presented in this thesis. For a detailed description of the scaffold sequence alignment see electronic supplement material.

Consumables and kits

Table E-15: Consumables & kits.

Consumables & Kits	Manufacturer
96- well plate	Bio-Rad Laboratories, Inc
96 Well Black Flat Bottom Polystyrene NBS	Corning
AFM / STM Metal Specimen Discs, ø15mm	Ted Pella, Inc.
Amicon Ultra Centrifugal Filter Units 3, 50 & 100 kDa	Merck KGaA
Cellulose sheets	Kimberly Clark
Cryotubes (2 ml)	Greiner, BioOne, Starstedt
Dialysis tube, SpectraPor, MWCO: 6-8 kDa	Thermo Fisher Scientific
Erlenmeyer flasks (0,1-5l)	Neolab, VWR
Filtration unit	VWR International GmbH
Glooves	VWR International GmbH
Mica "V1" & "V3", 9.9 mm ø round, 0.1 mm thick	Plano GmbH
MicroAmp Clear Adhesive Film	Applied Biosystems
Microseal 'B' seal Seals	Bio-Rad Laboratories, Inc
Parafilm	VWR International GmbH
Pasteurpipettes	VWR International GmbH
PCR-Tubes (0,2 ml)	VWR International GmbH

Pipettes, serological	VWR International GmbH
Pipetting tips blue (1000 µl)	Eppendorf AG, Starlab International GmbH
Pipetting tips grey (20 µl)	Eppendorf AG, Starlab International GmbH
Pipetting tips yellow (200 µl)	Eppendorf AG, Starlab International GmbH
Polypropylen Tubes (15 ml, 50 ml)	VWR International GmbH
Reaction vessel (1,5, 2 & 5 ml)	Sarstedt AG & Co.
Scalpel, sterile	Swann-Morton, Sheffield, Great Britain
SCANASYST-Air/Fluid AFM tips	Bruker Nano Inc.
Schottflasks	VWR International GmbH
Sterile filters (0,2 µm)	VWR International GmbH
Syringe BD Plastipak Eccentric Luer Slip	Becton, Dickinson and Company
Taq Man Gene Expression Assay	Applied Biosystems
Taq Man Gene Expression Assay MasterMix	Thermo Fisher Scientific
Tweezer	VWR International GmbH
Westernblot membrane, Immobilon-P, 0.45 µm	Carl Roth GmbH + Co. KG
Whatman filter paper	VWR

General equipment

Table E-16: General equipment.

General Equipment	Manufacturer
- 80°C freezer	Thermo Fisher Scientific
- 20°C freezer	Liebherr-International Deutschland GmbH
4°C refrigerator	Liebherr-International Deutschland GmbH
Analytical Balance	Satorius AG
Atomic force microscope, MultiMode8	Bruker Corporation
AF 103 Ice Flaker	Scotsman Ice Systems

C-MAG HS 7, Magnetic stirrer	IKA-Werke GmbH & CO. KG
Centrifuge 5424 R; Centrifuge 5430 R; Centrifuge 5810 R	Eppendorf AG
Clean bench Mars Pro Cytosafe Class 2	Scanlaf
CFX96 RealTime PCR-System	Bio-Rad Laboratories, Inc
Gel documentation system, Gel Slite „Touch“	Intas
Gel documentation system, Amersham Imager 600 QC	GE Healthcare Life Sciences
Electrophoresis systems	VWR International GmbH, Bio-Rad Laboratories, Inc., C.B.S. Scientific Company, Inc.
Incubator IN30	Memmert GmbH + Co. KG
Measuring cylinder	Brand, Wertheim, Germany
Microwave	SHARP BUSINESS SYSTEMS DEUTSCHLAND GMBH
Nanophotometer	DeNovix Inc.
Pipette boy	Hirschmann
Pipettes Eppendorf Research plus	Eppendorf AG
Power Source power supply, 300V	VWR International GmbH
Precision Balance	Satorius AG
Shaking Incubator	New Brunswick Scientific
Spark 10M	Tecan Trading AG
SPROUT mini centrifuge 12V	Heathrow Scientific
Thermocylers	Eppendorf AG
Typhoon FLA 9000	GE Healthcare Life Sciences
Vacuum pump	VWR International GmbH
Vortex mixer, VV3	VWR International GmbH
Water purification system	Merck KGaA
Waterbath	Bandelin electronic GmbH & Co. KG
WTW Inolab pH 720	Xylem Analytics Germany Sales GmbH & Co. KG

F Curriculum Vitae

Der Lebenslauf ist in der Online-Version aus Gründen des Datenschutzes nicht enthalten.

G List of Authored and Coauthored Publications

- In preparation** Elisa-C. Schöneweiß, Kenny Bravo-Rodriguez, Elsa Sanchez-Garcia and Barbara Saccà. Binding affinity and proteolytic activity of a thrombin molecule embedded into a DNA origami frame.
- In preparation** Elisa-C. Schöneweiß*, Georg Homa*, Wolfgang Pfeifer, Christian Denkhaus, Purya Menzel and Barbara Saccà. Geometry and energetics of base stacking in absence of shape complementarity.
- In preparation** Elisa-C. Schöneweiß, B. Popper, B. Saccà. Validation of mRNA-Protein interaction of neuronal RBPs by 2D- origami nano technology.
- Nov 2017** Elisa-C. Schöneweiß, Andreas Jaekel and Barbara Saccà. Nanotechnology and the unique role of DNA. In *DNA Nanotechnology for Bioanalysis. From hybrid DNA nanostructures to functional devices*. Eds. Arrabito and Wang. ISBN-10:1786343797
- Feb 2017** Schöneweiß EC, Saccà B. *Nanoscale*. 2017 Mar 30;9(13):4486-4496. doi: 10.1039/c6nr08314e.
- Feb 2017** Sprengel A, Lill P, Stegemann P, Bravo-Rodriguez K, Schöneweiß EC, Merdanovic M, Gudnason D, Aznauryan M, Gamrad L, Barcikowski S, Sanchez-Garcia E, Birkedal V, Gatsogiannis C, Ehrmann M, Saccà B. *Nat Commun*. 2017 Feb 16;8:14472. doi: 10.1038/ncomms14472.
- Jan 2015** B. Saccà, Y. Ishitsuka, R. Meyer, A. Sprengel, E.C. Schöneweiß, G.U. Nienhaus and C.M. Niemeyer. *Angew Chem Int Ed Engl*. (2015) 54:3592-3597. Flagged as “hot” paper

H Declarations

Hiermit erkläre ich, gem. § 6 Abs. (2) f) der Promotionsordnung der Fakultäten für Biologie und Geographie zur Erlangung der Dr. rer. nat., dass ich das Arbeitsgebiet, dem das Thema „Reconfigurable DNA-nanochambers as dynamic compartmentalization systems“ zuzuordnen ist, in Forschung und Lehre vertrete und den Antrag von Elisa-Charlott Schöneweiß befürworte und die Betreuung auch im Falle eines Weggangs, wenn nicht wichtige Gründe dem entgegenstehen, weiterführen werde.

Essen, den _____
Unterschrift eines Mitglieds der Universität Duisburg - Essen

Hiermit erkläre ich, gem. § 7 Abs. (2) d) + f) der Promotionsordnung der Fakultät für Biologie zur Erlangung des Dr. rer. nat., dass ich die vorliegende Dissertation selbstständig verfasst und mich keiner anderen als der angegebenen Hilfsmittel bedient, bei der Abfassung der Dissertation nur die angegebenen Hilfsmittel benutzt und alle wörtlich oder inhaltlich übernommenen Stellen als solche gekennzeichnet habe.

Essen, den 23.05.2018 _____
Unterschrift des/r Doktoranden/in

Hiermit erkläre ich, gem. § 7 Abs. (2) e) + g) der Promotionsordnung der Fakultät für Biologie zur Erlangung des Dr. rer. nat., dass ich keine anderen Promotionen bzw. Promotionsversuche in der Vergangenheit durchgeführt habe und dass diese Arbeit von keiner anderen Fakultät/Fachbereich abgelehnt worden ist.

Essen, den 23.05.2018 _____
Unterschrift des/r Doktoranden/in

The following student works have been completed under my co-supervision:

- Bianca Hoofe, Bachelor thesis, Biology, SS 17, Evaluation of the encapsulation of the protein thrombin in a DNA origami framework

- Magdalena Zak, Master Practical, Medical Biology, SS 16, 14-3-3 ligand coupling to thiol-modified oligonucleotides

- Richard Kosinski, Master Practical, Medical Biology, WS 15/16, Anomalous folding of a 2D DNA origami

- Eric Bucholz, Master Practical, Medical Biology, WS 15/16, Determination of DNA-origami concentrations by qPCR

I Acknowledgement

Foremost, I would like to thank Dr. Barbara Saccà, Centre for Medical Biotechnology (ZMB) and Centre for Nano Integration Duisburg-Essen (CENIDE), University of Duisburg-Essen, for the opportunity to perform my PhD thesis under her supervision. The completion of my PhD could not have been accomplished without her throughout support and encouraging words not only on the scientific level. She has been always open for any kind of discussion and therefore I am deeply grateful, especially for her help and guidance during my last PhD year 2017. Everyone should be more than thankful and proud to be a part of her group.

I would particularly like to thank Prof. Dr. Markus Kaiser, Centre for Medical Biotechnology (ZMB), and Prof. Dr. Elsa Sánchez-García, Centre for Medical Biotechnology (ZMB), University of Duisburg-Essen mostly for academic input and taking time to evaluate my thesis.

I would also like to thank Kenny Bravo-Rodriguez for performing the computational simulation analysis.

Additionally, I owe a very important debt to Wolfgang Pfeifer (Pfeiflein, or called Nobs by very special friends), Geronimo Heilmann (Nafri), Richard Kosinski (Rico²-Regler, Riiihaaart) & MiniRico, Andreas Jaekel (AJ), Pierre Stegemann (Panzer-Pierre), Pascal Lill (Kalle), Steffen Köcher (Steffemmm) and Georg Homa (Junior#nohoma). You made the PhD time in Essen to such an awesome and nifty period in my life. Without you guys work wouldn't have been the same. The statement by our beloved friend Dimitrie, the Russian: "*When are you guys actually working? or Where do you get your experimental results from?*" demonstrate the highly enthusiastic atmosphere and emerged friendship between all of us (nevertheless, which got even more strengthened by commonly visits at our favorite bar *Drehscheibe* and epic trips, which should not be mentioned all here).

I'm as well deeply grateful to Svenja Blaskowski (Svenjay) and Jenny Bormann (Jenny-Benni). You always helped me getting a time out when balance between physical and mental activity was really necessary. Thank you for you both being like you are, such

special personalities and for the time we spend by running, laughing and having from time to time some glasses of wine.

Florian Schulz (Flo-the-Bo) and Sabrina Ninck (Brini), I want to thank for their throughout encouragement in organizing planned activities and social events during the last three years. Additionally, a big thank to Svenja Kernchen (SvenK), who always helped me to deal with bureaucracy tasks.

In the end, I would like to express my deepest appreciation to my mom, my dad, my grandmother and my sister Sofie and her partner Bastian for their encouragement, heartfelt support and motivation throughout my academic studies and my whole life.